

# Arsenic and antimony in the environment: Release and possible immobilization mechanisms



## Dissertation

zur Erlangung des akademischen Grades *doctor rerum naturalium*

(Dr. rer. nat.)

Vorgelegt dem Rat der Chemischen-Geowissenschaftlichen Fakultät der  
Friedrich-Schiller-Universität Jena

von Dipl.-Geologe Ralph Michael Bolanz  
geboren am 08.03.1982 in Freiburg i.B.

Gutachter:

1. Prof. Dr. Juraj Majzlan, Jena
2. Prof. Dr. Georg Büchel, Jena
3. Prof. Dr. Gerhard Heide, Freiberg

Tag der öffentlichen Verteidigung: Jena, 19.06.2013

## Eigenanteil des Doktoranden

---

### Mineralogy, geochemistry, and arsenic speciation in coal combustion waste from Nováky, Slovakia

R.M. Bolanz<sup>a</sup>, J. Majzlan<sup>a</sup>, Ľ. Jurkovič<sup>b</sup>, J. Göttlicher<sup>c</sup>

<sup>a</sup>Friedrich-Schiller-University, Institute of Geosciences, Burgweg 11, D-07749 Jena, Germany

<sup>b</sup>Comenius University, Department of Geochemistry, Mlynská dolina G, SK-84215 Bratislava, Slovakia

<sup>c</sup>Karlsruhe Institute of Technology, Institute for Synchrotron Radiation, Hermann-von-Helmholtz Platz 1, D-76344 Eggenstein-Leopoldshafen, Germany

Journal: FUEL, 94, 1, 125-136 (2012)  
Jahr: 2011  
DOI: 10.1016/j.fuel.2011.10.067  
Status: Publiziert

Die Veröffentlichung wurde durch den Doktoranden verfasst. Die Geländearbeit wurde von Ľubomir Jurkovič betreut, die Probenahme und Auswertung der Geländedaten erfolgte durch den Doktoranden. Alle Vorbereitungen der Proben und chemischen Analysen inklusive sequentiellen Extraktionen, Karbonatgehalt, Röntgenfluoreszenz, Elektronenstrahlmikrosonde und Röntgendiffraktion wurden durch den Doktoranden durchgeführt und ausgewertet. Die synchrotronbasierenden Techniken,  $\mu$ -Röntgendiffraktion und Röntgenabsorptionsspektroskopie, wurden durch Jörg Göttlicher betreut und von dem Doktoranden durchgeführt und ausgewertet.

Der Eigenanteil des Doktoranden an dieser Veröffentlichung beträgt 95 %.

### Structural incorporation of As<sup>5+</sup> into hematite

Ralph M. Bolanz<sup>1</sup>, Maria Wierzbicka-Wieczorek<sup>1</sup>, Mária Čaplovičová<sup>2</sup>, Peter Uhlík<sup>2</sup>, Jörg Göttlicher<sup>3</sup>, Ralph Steininger<sup>3</sup>, and Juraj Majzlan<sup>1</sup>

<sup>1</sup>Friedrich-Schiller-University Jena, Institute of Geosciences, 07745 Jena, Germany

<sup>2</sup>Comenius University in Bratislava, Department of Economic Geology, 842 15 Bratislava, Slovakia

<sup>3</sup>Institute of Synchrotron Radiation, Karlsruhe Institute of Technology, 76344 Eggenstein-Leopoldshafen, Germany

Journal: Environmental Science and Technology  
Jahr: 2012  
DOI: 10.1021/es305182c  
Status: Akzeptiert

Die Veröffentlichung wurde durch den Doktoranden verfasst. Die Synthesen der beschriebenen Eisenoxide und Eisenarsenate sowie deren Charakterisierung durch Röntgendiffraktion und Rasterelektronenmikroskopie wurde durch den Doktoranden durchgeführt. Die chemischen Messungen der Syntheseprodukte wurden durch Ines Kamp und Dirk Merten durchgeführt, wobei die Auswertung dieser Daten und ihre Weiterverarbeitung durch den Doktoranden erfolgte. Eine Probe wurde von Mária Čaplovičová und Peter Uhlík für Transmissionselektronenmikroskopie vorbereitet und gemessen, diese Daten wurden anschließend durch den Doktoranden weiterverarbeitet. Die synchrotronbasierte Röntgenabsorptionsspektroskopie wurde von Jörg Göttlicher und Ralph Steininger betreut, während sämtliche Proben durch den Doktoranden vorbereitet, gemessen und ausgewertet wurden. Alle Computermodellierungen wurden durch den Doktoranden durchgeführt.

Der Eigenanteil des Doktoranden an dieser Veröffentlichung beträgt 85 %.

## The effect of antimonate, arsenate and phosphate on the transformation of ferrihydrite to goethite, hematite, feroxyhyte, and tripuyhite

Ralph Michael Bolanz<sup>1</sup>, Ulrich Bläss<sup>1</sup>, Sonia Ackermann<sup>1</sup>, Valerian Ciobotă<sup>2</sup>, Petra Rösch<sup>2</sup>, Nicolae Tarcea<sup>3</sup>, Jürgen Popp<sup>2,3</sup> and Juraj Majzlan<sup>1</sup>

<sup>1</sup>Institute of Geoscience, Friedrich-Schiller-University Jena, Germany

<sup>2</sup>Institute of Physical Chemistry, Friedrich-Schiller-University Jena, Germany

<sup>3</sup>Institute of Photonic Technology, Jena, Germany

Journal: Clays and Clay Minerals, 61, 1, 11-25 (2013)

Jahr: 2012

DOI: 10.1346/CCMN.2013.0610102

Status: Publiziert

Die Veröffentlichung wurde durch den Doktoranden verfasst. Die Synthesen der einzelnen Eisenoxide wurden streckenweise (ca 30 %) durch Sonia Ackermann betreut und ansonsten durch den Doktoranden durchgeführt. Die Charakterisierung der Syntheseprodukte mittels Röntgendiffraktion und Rasterelektronenmikroskopie (betreut durch Maria Wierzbicka-Wieczorek und Arkadiusz Wieczorek) wurden vollständig durch den Doktoranden durchgeführt und ausgewertet. BET Oberfläche und chemische Zusammensetzung wurden durch Ines Kamp, Dirk Merten, Anna Schmidt und Beate Truckenprod gemessen, die Ergebnisse wurden durch den Doktoranden ausgewertet und weiterverarbeitet. Proben für Transmissionselektronenmikroskopie wurde durch den Doktoranden präpariert und unter Betreuung von Ulrich Bläss gemessen und ausgewertet.

Der Eigenanteil des Doktoranden an dieser Veröffentlichung beträgt 85 %.

Ort, Datum

Unterschrift des Betreuers

.....

.....



**Abstract**

(English)

This thesis is dedicated to the release and immobilization of  $\text{As}^{5+}$  and  $\text{Sb}^{5+}$  in contaminated complex and heterogeneous geomaterials. They include contaminated soils and ash from the coal combustion and can hold contaminants in many different ways. Although the physical properties and chemical composition of the contaminated materials vary widely, the mechanisms which direct and control the fate of the contaminants are supposedly similar. Only with the knowledge how these mechanisms operate, we can accomplish remediation projects successfully. Hence, this thesis explores mechanisms that can be generalized to many polluted sites, instead of a detailed investigation of a single or a few selected sites.

In order to understand these mechanisms, I carried out a mineralogical and geochemical investigation of a soil, which was mixed with contaminated As-rich ash waste. With techniques including powder X-ray diffraction (PXRD), inductively-coupled-plasma mass spectrometry (ICP-MS), sequential extractions, electron microprobe analysis (EMPA) and synchrotron based  $\mu$ -X-ray diffraction and X-ray absorption near edge spectroscopy, the carriers of  $\text{As}^{5+}$  in the fresh ash waste and soil-ash mixtures were identified and characterized. The results show that in the fresh ash waste glass particles and unburned coal particles with veinlets of As-rich calcite veins are the main carriers of  $\text{As}^{5+}$ . In the soil-ash mixtures, the soluble  $\text{As}^{5+}$  containing phases of the ash-waste almost completely disappeared and  $\text{As}^{5+}$  migrated into the soil components, which presumably consist of iron oxides and clay minerals.

In the following study, the immobilization of  $\text{As}^{5+}$  by iron oxides in the context of  $\text{As}^{5+}$  incorporation in hematite was investigated. For this study, ferrihydrite was doped with  $\text{As}^{5+}$  and transformed to hematite. The newly formed hematite was examined by ICP-MS, PXRD, scanning electron microscopy (SEM), transmission electron microscopy (TEM), and extended X-ray absorption fine structure (EXAFS) spectroscopy. The results show that  $\text{As}^{5+}$  needs not only be bound to the surface of hematite, but also can be incorporated into the hematite crystals with concentrations of 1.9 wt%  $\text{As}^{5+}$ . This novel immobilization mechanism encouraged me to investigate the possibility of  $\text{Sb}^{5+}$  incorporation into iron oxides in a subsequent study. In order to evaluate the possibility of structural incorporation of  $\text{Sb}^{5+}$  into iron oxides, ferrihydrite was doped with different concentrations of  $\text{Sb}^{5+}$  and transformed to more-well crystalline products. For comparison,  $\text{As}^{5+}$  and  $\text{P}^{5+}$  doped ferrihydrite was transformed at the same conditions. The transformation products were then analyzed and characterized by ICP-MS, PXRD, SEM and TEM. The results show that  $\text{Sb}^{5+}$  directly controls the outcome of the ferrihydrite transformation and therefore the transformation products. These transformation products contain significant amounts of  $\text{Sb}^{5+}$  with up to 14 wt% of  $\text{Sb}^{5+}$ , which exceeds an exclusive adsorption mechanism by far. It can therefore be assumed, that  $\text{Sb}^{5+}$  can be incorporated into the structure of iron oxides in high quantities by replacing  $\text{Fe}^{3+}$ .

This thesis demonstrates, that the incorporation of pollutants in iron oxides is a significant immobilization mechanism and thus has to be taken into account when dealing with the mobility of pollutants in contaminated soils.

## Kurzfassung

(Deutsch)

Diese Doktorarbeit ist der Mobilisation und Immobilisation von  $\text{As}^{5+}$  und  $\text{Sb}^{5+}$  in kontaminierten und heterogenen geologischen Materialien gewidmet. Zu diesen Materialien gehören kontaminierte Böden und Aschen aus der Braunkohleverbrennung, die Schadstoffe auf verschiedenste Arten und Weisen binden können. Obwohl die physikalische und chemische Zusammensetzung von kontaminierten Materialien stark variiert, sind die Mechanismen die das Verhalten der Schadstoffe lenken und kontrollieren vermutlich sehr ähnlich. Nur mit dem Wissen wie diese Mechanismen genau funktionieren, können wir Sanierungsprojekte erfolgreich durchführen. Deshalb beschäftigt sich diese These mit Mechanismen, die für kontaminierte Regionen allgemeingültig sind, statt eine detaillierte Studie für ein oder zwei spezielle Fallbeispiele durchzuführen. Um diese Mechanismen besser zu verstehen, habe ich mineralogische und geochemische Untersuchungen an einem Boden durchgeführt, der mit arsenhaltiger Asche vermischt wurde. Ich habe dazu Techniken wie Pulver-Röntgendiffraktometrie (XRD), Induktiv-Gekoppelte-Plasma Massenspektrometrie (ICP-MS), Sequentielle Extraktionen, Elektronenstrahlmikrosonde (EMS) und synchrotronbasierte  $\mu$ -Röntgendiffraktion und Röntgenabsorptionsspektroskopie (XANES) eingesetzt, um die Trägerstoffe des  $\text{As}^{5+}$  in der frischen Asche und den Boden-Asche-Gemischen zu identifizieren und charakterisieren. Die Resultate zeigen, dass in der frischen Asche Glaspartikel und unverbrannte Kohlereste mit hochgradig arsenhaltigen Calcitadern die Hauptträgerstoffe von  $\text{As}^{5+}$  sind. In den Boden-Asche-Gemischen hingegen, sind die löslichen  $\text{As}^{5+}$ -Trägerstoffe der Asche bereits größtenteils verschwunden und  $\text{As}^{5+}$  ist



zu Bestandteilen des Bodens migriert. Bei diesen Bodenbestandteilen handelt es sich voraussichtlich um Eisenoxide und Tonminerale.

In einer weiteren Studie wurde die Immobilisation von  $\text{As}^{5+}$  durch Eisenoxide, im Hinblick auf strukturellen Einbau von  $\text{As}^{5+}$  in Hämatit untersucht. Für diese Studie wurde Ferrihydrit mit  $\text{As}^{5+}$  dotiert und zu Hämatit umgewandelt. Der so entstandene Hämatit wurde durch ICP-MS, XRD, Rasterelektronenmikroskopie (REM), Transmissionselektronenmikroskopie (TEM) und synchrotronbasierter Röntgenabsorptionsspektroskopie (EXAFS) untersucht. Die Resultate dieser Studie zeigen, dass  $\text{As}^{5+}$  nicht ausschließlich an die Oberfläche von Hämatit gebunden sein muss, sondern auch mit Konzentrationen von 1.9 Gew.-%  $\text{As}^{5+}$  in die Hämatitkristalle eingebaut werden kann.

Dieser neuartige Immobilisationsmechanismus ermutigte mich dazu, in einer Folgestudie den strukturellen Einbau von  $\text{Sb}^{5+}$  in Eisenoxide zu untersuchen. Um die Hypothese des  $\text{Sb}^{5+}$  Einbaus in Eisenoxide zu überprüfen, wurde Ferrihydrit mit verschiedenen Konzentrationen von  $\text{Sb}^{5+}$  dotiert und zu besserkristallinen Eisenoxiden umgewandelt. Zum Vergleich wurde  $\text{As}^{5+}$  und  $\text{P}^{5+}$  dotierter Ferrihydrit bei den gleichen Bedingungen umgewandelt. Die Transformationsprodukte wurden anschließend mit ICP-MS, XRD, REM und TEM analysiert und charakterisiert. Die Resultate zeigen, dass  $\text{Sb}^{5+}$  direkt das Endergebnis der Ferrihydrittransformation beeinflusst und somit die Transformationsprodukte. Diese Transformationsprodukte zeigen mit zirka 14 Gew.-% hohe Konzentrationen an  $\text{Sb}^{5+}$  und überschreiten eine einfache Adsorption an die Oberfläche der Minerale damit bei weitem. Es kann daher angenommen werden, dass  $\text{Sb}^{5+}$  in hohen Konzentrationen in die Struktur der Eisenoxide durch eine  $\text{Fe}^{3+}$ -Substitution eingebaut werden kann.

Diese Dissertation zeigt, dass der Einbau von Schadstoffen in Eisenoxide einen bedeutenden Immobilisationsmechanismus darstellt und bei der Mobilität von Schadstoffen in kontaminierten Böden in Betracht gezogen werden muss.

**CONTENT**

<b>Abstract</b> (English)		<b>i</b>
<b>Kurzfassung</b> (Deutsch)		<b>iii</b>
<b>Acknowledgements</b>		<b>vii</b>
<b>List of figures</b>		<b>ix</b>
<b>List of tables</b>		<b>xiii</b>
<b>Introduction</b>		<b>Page 1</b>
<b>Chapter 1:</b>	Mineralogy, geochemistry, and arsenic speciation in coal combustion waste from Nováky, Slovakia	<b>Page 8</b>
<b>Chapter 2:</b>	Structural incorporation of As <sup>5+</sup> into hematite	<b>Page 49</b>
<b>Chapter 3:</b>	The effect of antimonate, arsenate and phosphate on the transformation of ferrihydrite to goethite, hematite, feroxyhyte, and tripuhyte	<b>Page 95</b>
<b>Outlook:</b>		<b>Page 133</b>

## ACKNOWLEDGEMENTS

The most important person who made this thesis possible is my advisor Professor Juraj Majzlan. I can't thank him enough for the countless questions he answered, the numberless advices he gave me, and the innumerable scientific opportunities he offered me to accomplish this work. He always gave me the chance to follow my own ideas, encouraged me when I struggled with unsolvable problems and showed me new ways when I had the feeling that I hit the end of the road. Without you this thesis would just be a theoretical probability never happened. Thank you.

I am grateful to my second advisor Professor Georg Büchel, whose encouragement in environmental geochemistry during the bio-geo colloquia, the remediation symposia, and brainstorming weekends in Siegmundsburg always gave me the feeling, that environmental topics are still of concern and worth of investigation. Although many other research fields, related to industry, climates change, and planetary geology, receive more funding and public interest, the environmental aspects of our plant should not be forgotten. Thank you.

I want to thank my parents, Helga and Siegfried Bolanz, who always encouraged me to follow my own ideas. When I became old enough to be interested in science, they supplied me with microscopes, telescopes and chemistry sets for children, in order to fulfill the needs of a young mind, thirsty for knowledge. Without you two, I would never be the person I am today. Thank you.

I wish to thank my family, Clivia Tag, Werner Wengler, Hannelore Futwängler, Beate Bolanz, and all my dearest friends and colleagues who always supported me in my decisions and gave me the inspiring environment and the safe harbor I needed for my studies. Thank you.

I want to thank Sonia Ackermann, Ulrich Bläss, Mária Čaplovičová, Valerian Ciobota, Jörg Göttlicher, L'ubomir Jurkovič, Jürgen Popp, Petra Rösch, Ralph Steininger, Nicolae Tarcea, Peter Uhlík, and Maria Wierzbicka-Wieczorek for a fruitful cooperation. Thank you.

I would like to thank the graduate school "Alteration and element mobility at microbe-mineral interface" and the Deutsche Forschungsgemeinschaft for funding my investigations. Thank you.

---

## List of figures

### Chapter 1

- Figure 1: A: Coal deposits of Nováky and Handlová, modified after Halmo et al. (2010). Inset shows the position of Nováky in Slovakia. B: An aerial photograph of the studied area with sampling locations. The Nitra river is marked for clarity by a thick white line.
- Figure 2: Soil profile of the ash flow near Zemianske Kostol'any covered by soil. Our samples of the ash-soil mixtures were collected from the ash buried under soil.
- Figure 3: Fraction of As extracted in each step of the sequential extraction normalized to the total arsenic concentration ( $As_{\text{tot,digestion}}$ , Table 2) for a sample of the lagooned ash waste (Bo 2) and an ash-soil mixture (Bo 5). Numbers in the sectors are the steps of the sequential extraction (see Table 1).
- Figure 4: Back-scattered electron images of an (A) unburned coal particle in ash, (B) calcite veins within an unburned coal particle in ash, (C) vesicular glass particle in ash, (D) spheroidal glass particle in ash, (E) grain-binding matrix in soil-ash mixture and (F) calcite crystal in soil-ash mixture.
- Figure 5: Element distribution map of an unburned coal particle with calcite veins in the ash.
- Figure 6: Element distribution map of a vesicular glass particle in the ash.
- Figure 7: A triangular plot of spheroidal (grey) and vesicular (black) glasses. The circle size is scaled to the As concentration in the glass.
- Figure 8: Bulk X-ray diffraction (synchrotron radiation,  $\lambda = 1.18241 \text{ \AA}$ ). The ticks below the pattern mark the calculated positions of diffraction peaks; top row – hematite, middle – plagioclase, bottom – quartz.
- Figure 9:  $\mu$ XRD pattern ( $\lambda = 0.886 \text{ \AA}$ ) of calcite of an unburned coal particle with calcite veins. The ticks below the pattern mark the calculated positions of diffraction peaks of calcite.
- Figure 10: XANES spectra of constituents of the lagooned ash waste (bottom four spectra) and the ash-soil mixtures (middle four spectra), compared to

the spectra of references with As<sup>3+</sup> (top spectrum, thin line) and As<sup>5+</sup> (top spectrum, thick line). All spectra were normalized to an edge jump of 1.

## Chapter 2

- Figure 1: The structure of hematite with an included angelellite-like cluster. The (210) plane of angelellite runs parallel to the (0001) plane of hematite. Fe<sup>3+</sup> atoms of the hematite structure closer than 3.1 Å to the next As<sup>5+</sup> atom of angelellite were excluded. A colored version of this figure is available in the supplementary material (Figure 2S).
- Figure 2: SEM microphotographs of the ferrihydrite transformation products. (a) rhombohedral crystals of hematite grown at 70°C at pH 4 in the absence of As<sup>5+</sup> in aqueous solution. (b) rhombohedral hematite crystals grown at 70 °C at pH 4 in 0.23 mM As<sup>5+</sup> solution. (c) disc-shaped hematite crystals grown at 200 °C at pH 4 at an molar As : Fe ratio of 1. (d) disc-shaped crystals of angelellite grown at 700 °C via a solid-state synthesis.
- Figure 3: Bright field TEM image (a) and corresponding selected area electron diffraction pattern (b) of a sliced hematite crystal. The crystal is oriented near the [ $\bar{2}$  205] zone axis parallel to the primary electron beam.
- Figure 4: Fourier transforms of the As K-edge spectra taken from sample HEM<sub>1to1</sub> (a), angelellite (b), scorodite (c), kaňkite (d), and parasymphesite (e). The grey dashed lines indicate prominent features of the second and third shell of sample HEM<sub>1to1</sub>.
- Figure 5: (a) Normalized, k<sup>3</sup>-weighted As K-edge EXAFS spectrum of sample HEM<sub>1to1</sub>. (b) real part of the Fourier transform of the As K-edge EXAFS spectrum of sample HEM<sub>1to1</sub>. (c) magnitude of the Fourier transform of the As K-edge EXAFS spectrum of sample HEM<sub>1to1</sub>. The black dots indicate the measured data, whereas the solid grey lines show the achieved fit.
- Figure 1S: (a) SEM microphotograph of a disc-shaped hematite crystal grown at 200°C, pH 4, and a molar As : Fe ratio of 1. (b) Scheme of the part,

which was sliced out of the hematite crystal. The cut was chosen to be parallel to the flattening direction of the spheroidal particle. (c) Slice of a hematite crystal which was analyzed later by TEM-EDX.

Figure 2S: Images of the structure of angelellite-like clusters, intergrown with hematite.  $O^{2-}$  atoms belonging to the original hematite structure are marked in red,  $Fe^{3+}$  atoms belonging to hematite are marked in brown. The  $O^{2-}$  atoms of angelellite are marked in green, whereas the  $Fe^{3+}$  atoms are marked in blue.  $As^{5+}$  atoms are marked in violet.

Figure 3S: Image of the angelellite-like cluster, which was used for the FEFF calculation. The radius of three spheres around three adjacent As atoms was chosen to be 5 Å.  $O^{2-}$  atoms belonging to the original hematite structure are marked in red,  $Fe^{3+}$  atoms belonging to hematite are marked in brown. The  $O^{2-}$  atoms of angelellite are marked in green, whereas the  $Fe^{3+}$  atoms are marked in blue.  $As^{5+}$  atoms are marked in violet.

Figure 4S: Structures of interest as described in the corresponding section. The structure of hematite was taken from Blake et al. (1966), angelellite (Moore & Araki, 1978), scorodite (Kitahama et al., 1975), kaňkite (unpublished data), and parasymphesite (Mori & Ito, 1950).

Figure 5S: XANES spectra of sample  $HEM_{1to1}$ , reference compounds, and  $As_2O_5$  and  $As_2O_3$  for the determination of the oxidation state of arsenic.

Figure 6S: (a) Fit of the structure of angelellite to sample  $HEM_{1to1}$  as real part of the Fourier transform of the As K-edge EXAFS spectrum. (b) Fit of the structure of angelellite to sample  $HEM_{1to1}$  as magnitude of the Fourier transform of the As K-edge EXAFS spectrum. (c) Fit of the structure of scorodite to sample  $HEM_{1to1}$  as real part of the Fourier transform of the As K-edge EXAFS spectrum. (d) Fit of the structure of scorodite to sample  $HEM_{1to1}$  as magnitude of the Fourier transform of the As K-edge EXAFS spectrum. The blue dots indicate the measured data, whereas the solid red lines show the achieved fit.



Figure 7S: Powder XRD pattern of sample HEM<sub>1to1</sub>. The red bars show the calculated hematite peak positions.

### Chapter 3

Figure 1: Iron oxide speciation and quantification for P, As, and Sb-doped ferrihydrite and subsequently formed transformation products.

Figure 2: Bright field TEM image and corresponding selected area electron diffraction pattern (inset) of that area showing the rhombohedral shape and the sharp diffraction spots of feroxyhyte.

Figure 3: Chemical composition of the transformation products given as molar ratios of P, As, and Sb against Fe. The molar starting ratios of P/As/Sb : Fe are given for each concentration step.

Figure 4: Ferrihydrite transformation in the presence of increasing Sb(V)-concentrations. The numbers in front of each pattern indicate the molar Sb:Fe ratio. hem: hematite, goe: goethite, fx: feroxyhyte, tri: tripuhyte. All experiments were performed at pH 4 and an aging time of 16 days.

Figure 5: Selected Raman spectra of ferrihydrite transformations at increased Sb(V) concentrations. Sample 1 was transformed at pH 4, 70 °C and Sb(V) concentrations of 6.000 mM with a aging time of 16 days. Sample 2 was transformed at the same conditions, but pH 7 instead of pH 4. Sample 3 was transformed at an molar Sb:Fe ratio of 0.600 at pH 4, 70 °C and 16 days of aging.

Figure 6: Graphical summary of the maximum adsorption capacities calculated from different literature values. The striped bars show the adsorption capacity that can be reached by every cited literature value. The grey bars indicate the uncertainty for the maximum adsorption capacity calculated from literature values. Dots indicate that only one literature value was available. fh: ferrihydrite, hem: hematite, goe: goethite.

Figure 7: Selected electron diffraction pattern of feroxyhyte. The powder pattern shows the four dominant diffraction lines of feroxyhyte, whereas additional lines of hematite are clearly absent. In [010] zone pattern, the (001) reflection of feroxyhyte is clearly visible but should be extinct for hematite.  $[1\bar{1}1]$  and  $[2\bar{2}1]$  zone pattern belong to the same crystal tilted by  $\sim 18^\circ$  along the  $[110]$  axis.

Figure 8: On the left side the structure of goethite ( $\alpha$ -FeOOH) constructed by double octahedral chains (Pbnm setting). In a high pressure environment the tunnels which run parallel to the octahedral chains collapse forming the denser high pressure phase  $\varepsilon$ -FeOOH (upper right). During the Sb(V)  $\rightarrow$  Fe(III) substitution these tunnels could also collapse forming the denser tripuhyite structure (lower right). Both,  $\varepsilon$ -FeOOH and tripuhyite are isostructural with rutile.

Figure 9: Structures similar to that of hematite (left) can incorporate pentavalent ions. These pentavalent ions cannot occur in close contact to each other because of the strong electrostatic repulsion. In LiNbO<sub>3</sub>, a superstructure of hematite, the presence of Nb(V) face-sharing octahedra is avoided by monovalent Li<sup>+</sup> octahedra in between, reducing the electrostatic repulsion.

## List of tables

### Chapter 1

Table 1: Mineralogical composition of the lignite coal after <sup>a</sup>Verbich (1998) [16] and <sup>b</sup>Mecháček & Petrík (1967) [17].

Table 2: Sampling positions with GPS coordinates and chemical composition of the ash waste and soil-ash mixtures measured by X-ray fluorescence (XRF) spectrometry. XRF data in weight %.

Table 3: Sequential extraction procedure used in this study (after Tessier et al. 1979)

Table 4: Arsenic concentration (in mg/kg) determined by the total digestion ( $As_{tot,digestion}$ ) and each step of the sequential extraction of the ash and soil-ash mixtures measured by atomic absorption spectroscopy (AAS).  $As_{tot,seq,ex}$  shows the total arsenic retrieved in all steps of the sequential extraction.

Table 5: Concentrations of Al, Ca, Fe, and Mn (in mg/kg) released from the ash (sample Bo 1) in each step of the sequential extraction after Tessier et al. 1979 measured by ICP-OES.

- Table 6: Electron microprobe analysis for the constituents of the ash.  $n$  is the number of analyses averaged, the value in parenthesis is one standard deviation. All analytical data in weight %. The row volume % reports the estimate of the proportions of the constituents determined by areal integration of back-scattered electron images. The bottom row is the amount of As in each constituent in ppm.
- Table 7: Electron microprobe analysis for the constituents of the soil-ash mixtures.  $n$  is the number of analyses averaged, the value in parenthesis is one standard deviation. All analytical data in weight %.

## Chapter 2

- Table 1: Lattice parameters of the ferrihydrite transformation products grown in the absence and presence of  $\text{As}^{5+}$ . The numbers in parentheses are the standard deviations of the measurements on the last decimal digit reported.
- Table2: Scattering paths, coordination numbers (CN),  $\Delta r$ , and  $\sigma^2$  of the angelellite-like cluster fit to sample  $\text{HEM}_{1\text{to}1}$ . The third shell was split into 3-1 and 3-2 with two independent  $\Delta r$  values.
- Table 1S: Scattering paths, coordination numbers (CN),  $\Delta r$ , and  $\sigma^2$  of angelellite fit to sample  $\text{HEM}_{1\text{to}1}$ . The third shell was split into 3-1 and 3-2 with two independent  $\Delta r$  values. Values with an asterisk (\*) were restrained during the fit.
- Table 2S: Scattering paths, coordination numbers (CN),  $\Delta r$ , and  $\sigma^2$  of scorodite fit to sample  $\text{HEM}_{1\text{to}1}$ . Values with an asterisk (\*) were restrained during the fit.
- Table 3S: Scattering paths, coordination numbers (CN),  $\Delta r$ , and  $\sigma^2$  of the angelellite-like cluster fit to sample  $\text{HEM}_{1\text{to}1}$ . The third shell was split into 3-1 and 3-2 with two independent  $\Delta r$  values.
- File 1S: Crystallographic information file for the angelellite-like sheeted cluster used for EXAFS fitting.

**Chapter 3**

Table 1: Iron oxide speciation by Raman spectroscopy from selected ferrihydrite transformation products. fh: ferrihydrite, goe: goethite, hem: hematite, and fx: feroxyhyte. The asterisk marks component occurring in trace amounts which were not detected by XRD.

# Introduction

Soil is one of the most valuable resources for our society. About 99 % of our food supply comes from land [1] and is related to agricultural soils. Soils are also natural filter systems, which can immobilize pollutants carried in aqueous solutions and thus purify our drinking water from harmful substances. The importance of an unpolluted soil cannot be overstressed.

When soils become polluted, risks have to be assessed and remediation techniques can be considered in order to restore them to the original or near-original state. For both approaches, the type of pollutant, its concentration and bioavailability are significant factors to take into account. The latter is strongly influenced by the mobility of the pollutant. Arsenic is a good example for a pollutant, since it is one of the most widespread contaminants and is known for its toxicity [2]. Even at low concentrations, arsenic can cause serious health problems [3]. Additionally, many arsenic compounds possess a high solubility product [4] and may therefore be of high bioavailability. Each study dealing with a contaminated soil should therefore start with the identification of the pollutant, its concentration, chemical speciation, localization and identification of the phases, which carry the pollutant, and possible immobilization mechanisms of the soil constituents.

Especially the immobilization mechanisms in soils are still barely understood due to their complex interactions between geological and biological processes. Minerals, for example, belong to the non-living environment and are studied by geoscientists. Minerals can also be formed by the activities of microorganisms that belong to the living environment and are investigated by biologists. The formation of some minerals is therefore a result of bio-geo interaction and these processes should be explored by an interaction between geoscientists and biologists.

The most prominent example for microbial mineral formation in soils is a poorly crystalline iron oxide called ferrihydrite ( $\sim\text{Fe}_2\text{O}_3 \cdot n\text{H}_2\text{O}$ ). Ferrihydrite, the probably most widespread biomineral [5], is not only the precursor for many other iron oxides (e.g. [6]), it is also an driving force for the immobilization of pollutants in soils (e.g. [7,8,9]). The pollutant-immobilizing capacity of ferrihydrite owes largely to its high specific surface area of about  $300 \text{ m}^2/\text{g}$  [10]. This high specific surface area allows ferrihydrite to adsorb considerable amounts of pollutants, since the number of binding sites per gram of ferrihydrite is higher than for most other soil constituents. However, the adsorption of pollutants to the surface of ferrihydrite is not a long-term immobilization mechanism. Under oxidizing conditions, ferrihydrite is often unstable and transforms to more-well crystalline iron oxides over time, like goethite ( $\alpha\text{-FeOOH}$ ) and hematite ( $\alpha\text{-Fe}_2\text{O}_3$ ) (e.g. [6]). The transformation products of ferrihydrite depend on the pH [11], temperature [11], and the type and concentration of foreign ions, e.g. adsorbed pollutants [12]. But what happens to these adsorbed pollutants when ferrihydrite transforms to other iron oxides? The typical transformation products of ferrihydrite, namely goethite and hematite, have much smaller specific surface areas of  $\sim 40$  and  $\sim 20 \text{ m}^2/\text{g}$  [10,13], respectively. Assuming that the surface of ferrihydrite was completely covered by adsorbed pollutants, the transformation products can adsorb, bind, and therefore immobilize only a fraction of these pollutants, relative to their specific surface area. The pollutants, which cannot be retained by the transformation products are mobilized again and become a risk for the surrounding biosphere. Adsorption, however, seems not to be the only immobilization mechanism iron oxides possess. Recent studies investigated the fate of antimonate ( $\text{Sb}^{5+}$ ) in the presence of iron oxides and concluded that  $\text{Sb}^{5+}$  is not just adsorbed to the surface of the transformation product goethite, but also incorporated into the goethite structure [14,15]. For contaminated sites, the

incorporation of pollutants in iron oxides could be a significant immobilization mechanism. Pollutants adsorbed to the minerals surface can easily be desorbed by competing ions [16], pollutants bound in a crystal structure, however, can be considered immobilized until the host mineral becomes unstable and dissolves or recrystallized.

This dissertation thesis is dedicated to the fate of arsenate ( $\text{As}^{5+}$ ) and antimonate ( $\text{Sb}^{5+}$ ) in contaminated soils and possible long-term immobilization mechanisms associated with iron oxides. In the first chapter of this thesis, a mineralogical and geochemical survey of a soil was conducted, which became contaminated by  $\text{As}^{5+}$ -rich ash-waste from a brown coal burning power plant in central Slovakia. The task was to identify the primary  $\text{As}^{5+}$  carriers in the fresh ash-waste, compare them to the  $\text{As}^{5+}$  carriers in the soil and evaluate if migration to the soil constituents, like the iron oxides, occurred. A change in the  $\text{As}^{5+}$  carriers from the fresh ash-waste to the soil-ash mixtures would indicate a mobilization of  $\text{As}^{5+}$  by the weathering of the original  $\text{As}^{5+}$ -carriers and a subsequent immobilization of  $\text{As}^{5+}$  by the soil components. For the investigation, the bulk chemistry of the ash-waste and soil-ash mixtures was analyzed by X-ray fluorescence spectrometry (XRF) and inductively-coupled plasma mass spectrometry (ICP-MS). Subsequently, sequential extractions were performed to allocate the  $\text{As}^{5+}$  to possible carrier phases and the mineralogical bulk composition was analyzed by powder X-ray diffractometry (PXRD). After the bulk composition of the ash-waste and the soil-ash mixtures was characterized, the individual components of both matrices were morphologically and chemically classified by electron microprobe analysis (EMPA). This classification was further used to gather more information about the individual components with synchrotron techniques like micro-X-ray diffraction ( $\mu$ -XRD) and X-ray absorption near edge spectroscopy

(XANES). The combined data of all these measurements could then finally be used to show the fate of  $\text{As}^{5+}$ , from its original carrier phases in the ash-waste, which weathered in the soil-ash mixtures and the migration of  $\text{As}^{5+}$  to the soil components. From the results of chapter 1, iron oxides were identified as possible immobilizers for  $\text{As}^{5+}$  in the contaminated soil. The consequence from this data was the evaluation of the immobilizing mechanisms provided by iron oxides. Chapter 2 of this work was therefore devoted to the transformation of ferrihydrite in the presence of  $\text{As}^{5+}$  and possible immobilization mechanisms, which are related to this transformation. Previous studies suggested, that  $\text{P}^{5+}$ , in many cases a chemical analogue for  $\text{As}^{5+}$ , cannot only be bound to the surface of the iron oxides, but can be incorporated into the structure of hematite [17].

To investigate a possible incorporation of  $\text{As}^{5+}$  in hematite, synthesized ferrihydrite was doped with different concentrations of  $\text{As}^{5+}$  and transformed to hematite at pH 4 from 70-200 °C. The newly formed hematite was analyzed for its  $\text{As}^{5+}$  concentration by ICP-MS and the unit cell parameters of hematite were determined by PXRD. Morphology and grain size of the hematite crystals were investigated by scanning electron microscopy (SEM). Since it was assumed that  $\text{As}^{5+}$  is not only bound to the crystal surface by adsorption, but also incorporated into the structure of hematite, selected hematite crystals were embedded in resin and cut into ~ 90 nm thin slices. The slices could then be analyzed by transmission electron microscopy (TEM), which allowed us to determine the  $\text{As}^{5+}$  content inside the crystals by energy dispersive mode (EDX). In the last step of this study, the short-range order and the nearest neighbor atoms around  $\text{As}^{5+}$  were investigated by extended X-ray absorption fine-structure (EXAFS) spectroscopy at the synchrotron-light source ANKA in Karlsruhe. From this data, a new immobilization mechanism for  $\text{As}^{5+}$  by hematite could be described and the possibility of  $\text{As}^{5+}$  incorporation in hematite could be proven.



Since the structural incorporation of  $\text{As}^{5+}$  into a transformation product of ferrihydrite is possible, like shown in chapter 2, the following chapter evaluated the possibility of incorporation of other elements, which are relevant in natural systems and for contaminated soils. In this study the transformation of ferrihydrite in the presence of antimony ( $\text{Sb}^{5+}$ ) and phosphorus ( $\text{P}^{5+}$ ) was evaluated and compared to  $\text{As}^{5+}$ .

Synthesized ferrihydrite was doped with different concentrations of  $\text{As}^{5+}$ ,  $\text{P}^{5+}$ , and  $\text{Sb}^{5+}$  and transformed to more crystalline iron oxides at 70 °C and pH 4, 7, and 12. The concentration of the foreign ions in the transformation products was analyzed by ICP-MS and the products were characterized by PXRD, Raman spectroscopy, and transmission electron microscopy (TEM). Particle size and morphology of the transformation products were analyzed by SEM and TEM, whereas the specific surface area was investigated by the Brunauer-Emmet-Teller method [18]. With the combined data of all the individual techniques, a new model for  $\text{Sb}^{5+}$  immobilization by iron oxides could be developed.

## References

- [1] Pimentel, D., Giampietro, M. (1994) Global population, food and the environment. *Trends in Ecology and Evolution*, 9, 6, 239
- [2] Henke, K. (2009) *Arsenic – Environmental Chemistry, Health Threats and Waste Treatment*. John Wiley & sons Ltd. Chichester
- [3] Smith A.H., Lingas, E.O., Rahman, M. (2000) Contamination of drinking-water by arsenic in Bangladesh: a public health emergency. *Bulletin of the World Health Organization*, 78 (9), 1093-1103.
- [4] Pokrovski, G., Gout, R., Schott, J., Zotov, A., Harrichoury, J-C. (1996) Thermodynamic properties and stoichiometry of As (III) hydroxide complexes at hydrothermal conditions. *Geochimica et Cosmochimica Acta*, 60, 5, 737–749.
- [5] Konhauser, K.O. (2007) *Introduction to geomicrobiology*. Blackwell Science. 425 pp.
- [6] Cornell, R.M., Schwertmann, U. (2003) *The iron oxides, properties, reactions, occurrences, and uses*. Wiley-VCH Verlag, Weinheim.

- 
- [7] Waychunas, G.A., Rea, B.A., Fuller, C.C., Davis, J.A. (1993) Surface chemistry of ferrihydrite: Part 1. EXAFS studies of the geometry of coprecipitated and adsorbed arsenate. *Geochimica et Cosmochimica Acta*, 57, 2251-2269.
- [8] Waychunas, G.A., Davis, J.A., Fuller, C.C. (1995) Geometry of sorbed arsenate on ferrihydrite and crystalline FeOOH: Re-evaluation of EXAFS results and topological factors in predicting sorbate geometry, and evidence for monodentate complexes. *Geochimica et Cosmochimica Acta*, 59, 3655-3661.
- [9] Manceau, A. (1995) The mechanism of anion adsorption on iron oxides: evidence for the bonding of arsenate tetrahedral on free Fe(O,OH)<sub>6</sub> edges. *Geochimica et Cosmochimica Acta*, 59, 3647-3653.
- [10] Schwertmann, U., Cornell, R.M. (2000) *Iron oxides in the laboratory: Preparation and Characterization*, 2nd edition. Wiley-VCH Verlag, Weinheim.
- [11] Das, S., Hendry, J., Essilfie-Dughan, J. (2011a) Effects of adsorbed arsenate on the rate of transformation of 2-line ferrihydrite at pH 10. *Environmental Science & Technology*, 45, 5557-5563.
- [12] Das, S., Hendry, J., Essilfie-Dughan, J. (2011b) Transformation of two-line ferrihydrite to goethite and hematite as a function of pH and temperature. *Environmental Science & Technology*, 45, 268-275.
- [13] Torrent, J., Schwertmann, U., Barrón, V. (1994) Phosphate sorption by natural hematites. *European Journal of Soil Science*. 45, 45-51.
- [14] Scheinost, A.C., Rossberg, A., Vantelon, D., Xifra, I., Kretzschmar, R., Leuz, A.K., Funke, H., Johnson, C.A. (2006) Quantitative antimony speciation in shooting-range soils by EXAFS spectroscopy. *Geochimica et Cosmochimica Acta*, 70, 3299-3312.
- [15] Mitsunobu, S., Takashi, Y., Terada, Y., Sakata, M. (2010) Antimony(V) incorporation into synthetic ferrihydrite, goethite, and natural iron oxyhydroxides. *Environmental Science & Technology*, 44, 7312-7318.
- [16] Pigna, M., Krishnamurti, G.S.R., Violante, A. (2006) Kinetics of arsenate sorption-desorption from metal oxides. *Soil Science Society of America*, 70, 6, 2017-2027
- [17] Gálvez, N., Barron, V., Torrent, J. (1999) Preparation and properties of hematite with structural phosphorus. *Clays and Clay Minerals*, 47, 3, 375-385.
- [18] Brunauer, S., Emmett, P.H., and Teller, E. (1938) Adsorption of gases in multimolecular layers. *Journal of the American Chemical Society*, 60, 308-319.

## **Chapter one**

# **Mineralogy, geochemistry, and arsenic speciation in coal combustion waste from Nováky, Slovakia**

R.M. Bolanz<sup>a\*</sup>, J. Majzlan<sup>a</sup>, L. Jurkovič<sup>b</sup>, J. Göttlicher<sup>c</sup>

<sup>a</sup>Friedrich-Schiller-University, Institute of Geosciences, Burgweg 11, D-07749 Jena, Germany

<sup>b</sup>Comenius University, Department of Geochemistry, Mlynská dolina G, SK-84215 Bratislava, Slovakia

<sup>c</sup>Karlsruhe Institute of Technology, Institute for Synchrotron Radiation, Hermann-von-Helmholtz Platz 1, D-76344 Eggenstein-Leopoldshafen, Germany

\* corresponding author: Tel. +49-3641-948704, fax +49-3641-948602, email address:  
Ralph.Bolanz@uni-jena.de

Submitted to: FUEL, February 21<sup>st</sup>, 2011

Reviews received: September 21<sup>st</sup>, 2011

Revision 1 submitted: October 18<sup>th</sup>, 2011

Accepted: October 27<sup>th</sup>, 2011

Published: April, 2012

Reproduced according to the rules of ELSEVIER, publisher of *FUEL*.

**ABSTRACT**

We used a suite of techniques to characterize the mineralogy, geochemistry, and arsenic speciation in lagooned combustion waste (ash) from coal burning and ash buried under agricultural soil since 1965 when a dam of one of the ash ponds failed. Coal seams from Nováky (Slovakia) contain low-temperature hydrothermal mineralization with orpiment ( $\text{As}_2\text{S}_3$ ). The lagooned ash waste has 1000-1400 ppm As and consists of vesicular and compact glasses (86.29 % of the ash with an average of 0.13 wt%  $\text{As}_2\text{O}_5$ ), spheroidal glasses (2.53 % of the ash; 1.35 wt%  $\text{As}_2\text{O}_5$ ), unburned coal particles (7.76 % of the ash; 0.10 wt%  $\text{As}_2\text{O}_5$ ) with calcite veins (0.27 % of the ash; 1.60 wt%  $\text{As}_2\text{O}_5$ ), as well as quartz, plagioclase, and traces of poorly crystalline mullite (3.15 % of the ash; 0.01 wt%  $\text{As}_2\text{O}_5$ ). The major As carriers are the glasses and electron microprobe analyses document high affinity of As towards Ca-rich material in the glasses. Sequential extractions show massive release of Ca during the mildest leaching (water or  $\text{MgCl}_2$  solution); As is released especially under reducing conditions. The soil-ash mixtures from 1965 have 1078-1381 ppm As, almost the same As concentration as the lagooned ash waste. In addition to the constituents identified in the lagooned combustion waste, they contain an omnipresent fine-grained matrix (0.05 wt%  $\text{As}_2\text{O}_5$ ) between the grains, most likely made of poorly crystalline clays and iron oxides. More than 90 % of the As in the lagooned ash waste and soil-ash mixtures occurs as  $\text{As}^{5+}$ . Our results allow us to track the fate of As: during combustion, As is incorporated into glasses, especially in those rich in Ca; in the ash impoundment, calcium arsenates form (assumption based on literature data) and are slowly replaced by calcite with a concomitant release of As. In the ashes buried in soils, part of this As is retained on pre-existing or newly-formed iron oxides and clays.

**Keywords:** coal combustion waste, mineralogy, sequential extraction, arsenic, speciation

## INTRODUCTION

Coal is the second most important source of energy with 27.4 % of the world primary energy production [1]. Almost all coal (6.42 billion metric tons in 2007) is burned to produce electric power [1]. Coal burning is, in turn, the second largest input of arsenic into the atmosphere, after smelting of Cu ores [2]. Implementation of modern filter systems reduced the release of harmful elements such as As, Cd, Cr, Hg and Ni into the atmosphere [3]. Nevertheless, the disposal of the residues after burning is still problematic. These combustion residues comprise the fly ashes, bottom ashes, and lagooned ash mixtures and will be collectively referred to as ash waste in this paper. After the burning process, the ash is often deposited in uncovered ash impoundments, where it interacts with the surrounding environment. Rainwater leaches the toxic elements and carries them into rivers and the ground water (*e.g.* [4]). Wind-blown ash particles cover large areas with harmful dust and impoundment failures devastate and contaminate the landscape. Arsenic is often of special interest in such cases because of its common occurrence in coals, up to 10000 ppm [5] or even 35000 ppm [6], and because of its relatively high solubility, mobility, and toxicity. For a better understanding of the risks associated with the ash waste, we need to characterize the speciation, solubility, and bioavailability of As in these waste products.

Ash is generally composed of heterogeneous microscopic particles whose nature depends on the initial chemistry and mineralogy of the coal and the combustion processes in a given power plant. Numerous studies exist about the phase and mineralogical composition of the combustion residues around the world (*e.g.* [7], [8], [9], [10], [11]). Much work has been dedicated to the morphological description and the association of the main chemical components with the particles in the ash.

In this work, we present a detailed mineralogical and geochemical study of combustion residues – ashes from the Nováky and Handlová coal deposits in central Slovakia. In particular, we examined the samples with a set of methods with micro resolution in order to determine the constituents which carry or possibly release arsenic. The materials studied in this work are of interest because they offer the possibility of comparing lagooned and old (~40 years) ash waste, the latter being covered by soil.

*Geological setting, power plant specifications and coal composition*

Coal seams are known from the Western Carpathians from sedimentary complexes of Carboniferous to Pliocene age [12]. The coalfields of Nováky and Handlová are one of the most important accumulations of fossil fuels in the Western Carpathians (Fig. 1) [13]. The underlying beds of the coal seams are made of tuffite. The uppermost strata of the underlying formation are volcanic derived sediments of redeposited and autochthonous pyroclastic rocks with epiclastogene volcanic rocks and coal segments [14]. These strata pass gradually into coals, bone coals, and coal beds with bands of clay. Other bands like tuffites and “dirt-bands” can be found within the 8-10 m thick coal layer splitting the main bed in up to 3 different layers, often seen in the northwestern parts of the deposit. The thickness of the individual coal layers is therefore only 1.1-5.0 m [12].

The power plant Nováky is operating since 1953 in a basic and semi-peak mode. The combustion is taking place in two dry bottom boilers (2 x 110 t/h steam) and a fluidised bed boiler (125 t/h steam). After the combustion process the ash waste is discharged via wet discharge system, pumping the ash-water mixture directly to the ash pond. The Nováky plant burns mostly lignite coal from the Nováky and Handlová coal deposit with an average calorific value of 10.5 MJ/kg [15]. The composition of



the lignite coal from Handlová shows  $A^d = 7.70$  wt% (ash content),  $W^a = 12.26$  wt% (moisture),  $C^d = 61.6$  %,  $H^d = 5.6$  %,  $N^d = 0.7$  %,  $S^d = 1.2$  %, and  $O^d = 23.2$  % (d = dry sample, a = sample including water) (Zubrik et al. 2009). A detailed mineralogical composition of the lignite coal is displayed in Table 1.

Orpiment ( $As_2S_3$ ) occurs in these coals [18], resulting in total As concentrations of 518 ppm As (arithmetic mean), range 18.5–1,540 ppm As [19]. During the operation of the power plant, the combustion waste was deposited in several ash ponds and remains there until today. In 1965, the dam of one of the ponds failed and contaminated an area of approximately 19,000 ha of the adjacent broad valley of the Nitra river [20]. Instead of remediation, the ash flow, up to 1 meter thick, was covered by 40-100 cm of soil and parts of it have been used since as agricultural areas, either fields or meadows.

## **MATERIALS AND METHODS**

### *Sampled Areas*

The samples Bo 1 and Bo 2 represent lagooned ash waste from the active ash impoundment near Zemianske Kostol'any, where the ash slurry is being delivered by a pipe system from the Nováky power plant. Four additional samples Bo 3-6 (Table 2) were taken from the ash flow from 1965. The ash was covered by soil and we took the samples from a depth of 10-50 cm (Fig. 2).

### *General sample preparation*

For the chemical analyses, the ash and soil-ash mixtures were dried at 105 °C for 24 h and ground with a Retsch RM 100 corundum mill. For the light microscopy and subsequent analytical work, the ash and soil-ash mixtures were air dried and stored in sealed plastic bags.

### *Total digestion and sequential extractions*

For the total digestion, 0.2 g of the dried, powdered ash or soil-ash mixtures were treated with 1 mL H<sub>2</sub>O<sub>2</sub> (30%), 6 mL HNO<sub>3</sub> (65%), and 1 mL HBF<sub>4</sub> (48%) in Teflon vessels. The digestion was performed in a MPREP-A MWS starT-System industrial microwave oven. The mixtures of the liquid and the sample were heated up to 230 °C within 7 minutes and held at this temperature for another 15 minutes. This procedure is standard for processing of brown coal dust after MLS-application E706-Braunkohlestaub by G. KOPP, application lab Leutkirch (Germany) and proved suitable for coal combustion waste.

The sequential extractions were performed after Tessier et al. [21]. The solutions used and the treatment applied in each step is described in Table 3. After each step, the suspension was centrifuged for 3 min, decanted, and the clear solution retained for analysis. Nominally, the first step of the sequential extraction targets exchangeable As adsorbed to mineral surfaces; the second step the carbonate fraction; the third step Fe and Mn oxides; and the fourth step organic matter. This sequential extraction procedure was originally developed for natural materials (soils) and the nominal targeted groups likely do not apply to the studied ash. Yet, we use the sequential extraction to distinguish the various reservoirs of arsenic in our ash.

For each step, a blank and a duplicate from the sample Bo 1 (ash) was measured. All samples were measured by atomic absorption spectrometry with a graphite furnace (GF-AAS) 4110 ZL Perkin Elmer Zeeman. For comparison, additional ash samples were measured by inductively coupled plasma mass spectrometry (ICP-MS) Quadrupol-ICP-MS X Series II ThermoFischer Scientific and optical emission spectrometry (OES) Variant 725 ICP-OES with CCD.

### *Carbonate content*

The content of carbonates in the ash was analyzed by the Scheibler's method with a Scheibler apparatus from the geotechnical equipment company Wille GeoTechnik, Goettingen-Rosdorf, Germany. The analyses were performed after DIN 18129. Briefly, the samples were mixed with a pre-determined amount of 15 % HCl and the volume of the released CO<sub>2</sub> was measured.

### *X-ray fluorescence spectrometry (XRF)*

The XRF pellets were made of 4 g of the powdered ash or soil-ash mixtures and 1 g wax. The powder was thoroughly mixed by shaking for 15 minutes, pressed in a PW E30 hydraulic press with 294.2 kN, and analyzed under vacuum in a Philips PW 2404 wavelength-dispersive X-ray fluorescence spectrometer, equipped with a 4 kW Rh anode tube. For the analyses, LiF 220, Ge, PE and PX1 crystals and the Duplex and scintillation detectors were used. The data were processed with SemiQ/Quantitative V.2.01B. Due to the high As concentration of the samples, we avoided the preparation of fused beads. Therefore, the results have to be considered as semi-quantitative.

### *Electron Microprobe (EMP)*

The dried ash and soil-ash mixtures were embedded in Chlorapox 493 epoxy resin, ground and polished. The quantitative EMP analyses were conducted with a Cameca SX-100 electron microprobe with a constant sample current of 20 nA and an accelerating voltage of 15 kV. All quantitative analyses were done in the wavelength dispersive mode (WDS). For standards GaAs was used for As, corundum for Al, wollastonite for Ca, hematite for Fe, periclase for Mg, rhodonite for Mn, apatite for P, celestite for S, orthoclase for Si and rutile for Ti.

The quantitative EMP analyses have presented several difficulties. The porous nature of most ash particles, their carbonaceous components and possibly also water, as well as their small grain size led to oxide totals often less than 100 wt%. To ensure that all major elements were included, energy-dispersive spectra (EDS) were collected at each spot where WDS analysis was to be done.

Elements distribution maps and back-scattered electron (BSE) images for quantification purposes were acquired with a Cameca SX-50 electron microprobe with a constant sample current of 20 nA and an accelerating voltage of 30 kV. The element distribution maps were done in the energy-dispersive mode. The quantitative proportions of the constituents in the ash and soil-ash mixture were quantified by microprobe BSE images (magnification 1500x); the area of each constituent in the acquired images was digitally integrated.

#### *X-ray Diffraction (XRD)*

The bulk analysis of the ashes and soil-ash mixtures was carried out with a Bruker D8 Advance diffractometer, employing Cu K $\alpha$  radiation, a secondary graphite monochromator, and a scintillation detector. Two selected samples were additionally analyzed at the bending magnet beamline PDIFF at the synchrotron light source ANKA, Karlsruhe. X-rays with a wavelength of 1.1824(1) Å were selected with a double crystal Si(111) monochromator and the diffractometer wavelength and zero were refined with scans of Si and quartz. The ash and soil-ash mixtures were loaded in a glass capillary with an inner diameter of 1 mm and measured in transmission mode. The intensity of the incoming beam was determined by an ionization chamber and the intensity of the diffracted beam was corrected for the primary beam decay. The patterns were collected at room temperature between 3.4 and 41.4° 2 $\theta$ , with a

step size of 0.004 °2 $\theta$  and a dwell time of 1 s. All data were processed by Rietveld refinement with the program GSAS [22].

*X-ray Micro Diffraction and Micro X-ray Absorption Near-Edge Structure Spectroscopy ( $\mu$ XRD,  $\mu$ XANES)*

The  $\mu$ XRD patterns and  $\mu$ XANES spectra of the ash and soil-ash mixtures were collected at the SUL-X beamline at the synchrotron light source ANKA, Karlsruhe. As a monochromator, a silicon (111) crystal pair with a fixed beam exit was used. The X-ray beam was aligned to an intermediate focus, and then collimated by slits located at the distance of the intermediate focus to about 50×50  $\mu\text{m}^2$  and subsequently focused with a Kirkpatrick-Baez mirror pair to about 30×30  $\mu\text{m}^2$  at the sample position.

The  $\mu$ -XRD patterns were collected in the transmission mode with a Photonic Science CCD detector (type XDI-VHR 2 150). For a better comparison with the results of the EMP analyses, the support glass of the previously used thin sections were abraded to a thickness of 200  $\mu\text{m}$ . Selected grains were measured with a constant energy of 14 keV ( $\lambda = 0.886 \text{ \AA}$ ) and an exposure time of 60 s. Powdered LaB<sub>6</sub> was used as calibrant to verify the wavelength and to refine the sample to detector distance. The obtained CCD frames were integrated with the program Fit2D [23].

The  $\mu$ XANES spectra at As *K* edge were measured in the fluorescence mode in energy steps of 5 eV in the region from –150 to –50 eV relative to the absorption edge, of 2 eV in the region from –50 eV to –20 eV, of 0.5 eV from –20 eV to +20 eV, and with a step of 0.05k from +20 eV to +400 eV. The intensity of the primary beam was measured by an ionization chamber. Fluorescence intensities were collected with a 7 element Si(Li) solid state detector Gresham with the energy window set to

the As fluorescence emission  $K\alpha$  line. Data were dead-time corrected, summed up for all seven channels and divided by the primary beam intensity. The collected data were processed by ATHENA [24]. For each measured particle, seven spectra were measured. During the repeated measurements, an increasing  $As^{3+}$  and decreasing  $As^{5+}$  signal could be observed, probably caused by a beam induced reduction of the arsenic. Hence, only the first scan has been taken for data analysis.

## RESULTS

### *Total chemical composition – X-ray fluorescence (XRF) and carbonate content*

Bulk composition of the ash and soil-ash mixtures was probed by XRF. The results are summarized in Table 2. The oxides  $SiO_2$ ,  $Al_2O_3$ , CaO, and FeO account for ~90 wt% of the ash.  $SO_2$  is elevated in the lagooned ash waste, the soil-ash mixtures have higher Ti concentrations. The inability of the XRF to measure light elements ( $Z < 11$ ) means that carbon, a substantial component of our samples, was not analyzed. Carbonate analyses of the ash revealed calcite concentrations of 1.07 wt%.

### *Total arsenic and fractionation – total digestion and sequential extractions*

The total digestion shows significant contamination of both lagooned ash waste and soil-ash mixtures (Table 4). The bulk speciation of arsenic in our samples was probed by sequential extractions. We are aware that the formal interpretation of the individual steps (as iron oxide-bound, organic matter-bound, etc.) is not valid for complex synthetic matrices such as ash or soils mixed with ash. Yet, the sequential extraction may provide insights into the mobility of arsenic.

Only ~50 % of the arsenic determined by the total digestion was retrieved during the entire sequential extraction procedure (Fig. 3). Therefore, we assume that ~50 % of

---

As is bound in a hardly soluble state which can be brought into solution only by the aggressive total digestion. During the first step of the sequential extraction, a 1 M  $\text{MgCl}_2$  solution was added to the dried samples. Only the ash released a significant amount of arsenic into the solution with 44 ppm (sample Bo 1) and 64 ppm (Bo 2), which represents 8 to 9 % of the total arsenic released during the sequential extraction ( $\text{As}_{\text{tot,seq,ext}}$ ). In contrast, the soil-ash mixtures released just 2 % of the total. Lowering of pH of the extractant in the second step (Table 3) led to a release of 30-32 % of  $\text{As}_{\text{tot,seq,ext}}$  from the ash but only 11 % of  $\text{As}_{\text{tot,seq,ext}}$  from the soil-ash mixtures. During the third step (Table 3), under reducing conditions, the ash released 51-52 % of  $\text{As}_{\text{tot,seq,ext}}$  but the soil-ash mixtures 76-80 % of the  $\text{As}_{\text{tot,seq,ext}}$ . The fourth and last step (Table 3) reveals no significant differences between ash and soil-ash mixtures, the former releasing 9 % of the  $\text{As}_{\text{tot,seq,ext}}$ , the latter 8-11 % of the  $\text{As}_{\text{tot,seq,ext}}$  (see Table 4 for a summary).

It is instructive to monitor the behavior of other elements, not only the pollutant of interest, during the extractions. From the elements Ca, Mn, Al, and Fe, the first, mild step of the extraction released an enormous amount of Ca and very small amounts of Fe, Al, and Mn (Table 5). The mild extraction with 1 M  $\text{MgCl}_2$  released ~15 % of the total Ca content of the ash (compare Table 5 and Table 2), indicating that Ca is bound in this material in a highly mobile form. Similar results were obtained by extraction in deionized water (results not shown). The extractable amount of Fe, Al, and Mn increases in the following, more aggressive solutions; the amount of Ca, on the other hand, decreases (Table 5).

In summary, about 40 % of the total arsenic content of the ash and soil-ash mixtures was dissolved through the lowering of the pH and under reducing conditions (Fig. 3). However, the fact that only 50 % of the total arsenic can be found via sequential extraction calls for a more detailed microscopic investigation.

### *Constituents of the lagooned ash waste*

The lagooned ash waste from Zemianske Kostol'any (Bo 1 & Bo 2) is a loose material, with black to grayish color and pieces of porous clinker up to 2 cm large. No minerals or phases can be distinguished macroscopically. Microscopically, seven different constituents were identified (Fig. 4) based on their optical properties and morphology. They are described in detail below and include unburned coal particles, glasses of variable morphology and chemical composition, minerals of the wall-rocks of the coal seams and traces of iron oxides.

(1) Unburned coal particles (Fig. 4A) are irregular or rounded, with sizes from a few micrometers up to 2 mm with rough surfaces structures. Within these particles, anisotropic regions and embedded mineral grains, mostly quartz, can be observed. Most unburned coal particles are highly porous, only a few particles are more compact. The particles are frequently pervaded by ~1-10  $\mu\text{m}$  thick calcite veinlets (Fig. 4B) with typical high interference colors in crossed nicols in polarized light.

(2) Vesicular glass particles (Fig. 4C) are the dominant form of glasses. These spherical to semi-spherical, porous grains attain sizes of 30  $\mu\text{m}$  to 1 mm. The proportion of vesicles decreases rapidly below grain sizes of 100  $\mu\text{m}$  and diminishes completely at ~50  $\mu\text{m}$ . The vesicles lie usually near the surface of the glass particles. In crossed nicols, the glasses are completely extinct, with a few tiny bright spots, probably the initial products of devitrification.

(3) Spheroidal glass (Fig. 4D) are another common glass variety. Almost perfect spherical shapes indicate a derivation from melts with relatively low viscosity [7]. Average grain size lies between 3-30  $\mu\text{m}$  and rarely exceeds 50  $\mu\text{m}$ . Above 30  $\mu\text{m}$  the degree of sphericity is decreasing and first vesicles appear along the margins of the grain. In crossed nicols in polarized light, the spheres are completely extinct. The main reasons to differentiate the spheroidal from the vesicular glasses are their



chemical differences and the perfect spherical shape of the former. However, as described above, hybrid forms of these glasses occur around 30-50  $\mu\text{m}$  which show sphericity and the first signs of vesicle formation.

(4) Compact glass particles are yet another, more uncommon variation of glasses free of vesicles. The particles vary from large to very small, 1 mm to less than 10  $\mu\text{m}$ . They have irregular, sometime splintery shapes. Higher magnifications reveal inhomogeneous patches structures within the glasses, which let assume a derivation from melts with relatively high viscosity [7]. In crossed nicols in polarized light, these glasses are completely extinct.

(5) Mineral fragments of quartz, plagioclase and K-feldspar are another common constituent of the ash. The grains are anhedral or partially rounded, and 30-400  $\mu\text{m}$  large. Some quartz grains show undulatory extinctions, others display indications of magmatic corrosion. Probably most of the mineral fragments within the ash come from the host rocks of the coals. These minerals occur either individually or embedded in glasses and unburned coal particles.

(6) Iron oxides, identified as hematite can be found as traces in the ash. The small brownish to reddish anhedral flakes reach sizes of 100  $\mu\text{m}$ .

(7) Brownish anhedral grains, 50-900  $\mu\text{m}$  large were tentatively identified as mullite. At higher magnifications, colorless anisotropic regions can be observed, while other regions in the crystal are isotropic.

#### *Constituents of the soil-ash mixture*

Soil-ash mixtures from the flood plain of the Nitra river, in front of the active impoundment, were taken with a hand drill between the depths of 10 and 50 cm. At the sampling site, the ash layer from the impoundment failure in 1965 begins at a

depth of 40 cm. The four soil-ash mixtures (Bo 3-6) are light brown to grayish, with no macroscopic mineral grains. Microscopically, all soil-ash mixtures show the same constituents in different quantities. In addition to the constituents present in the lagooned ash waste, three additional constituents were identified.

(8) Most grains are cemented by a fine-grained, brown to **ochreous matrix** (Fig. 4E). We suppose that the matrix is rich in iron oxides and clays; no individual minerals can be recognized.

(9) Calcite crystals occur commonly in all soil-ash mixtures (Fig. 4F). The colorless euhedral to subhedral crystals are 0.5-2.25 mm large, show excellent cleavage and polysynthetic twinning.

(10) Decomposing wood and root fragments are another organic constituent beside the unburned coal particles. Reddish-brown pieces with sizes of ~0.5-4 mm can be observed. In transmitted light, vascular structures are common. In crossed nicols in polarized light, those structures are anisotropic, probably because of the cellulose within the herbal cell walls.

#### *Chemical composition of the constituents – electron microprobe (EMP)*

Knowing the concentration of As in the ash and soil-ash mixtures, as well as their different constituents, the question of the distribution of As among the constituents was tackled by EMP analyses. The As content of the constituents was measured by the WDS analyses and the volume fraction of the constituents was calculated by BSE image analysis. The contribution of each constituent toward the total arsenic budget of the ash is given in Table 6.

The vesicular glasses are the main constituent of the ash (86.29 vol.%) with an average concentration of 0.13 wt%  $\text{As}_2\text{O}_5$ . Despite the seemingly low As

concentration, these particles hold a considerable amount of the total As (Table 6). The spheroidal glasses reveal the highest As concentrations, up to 19.42 wt%  $\text{As}_2\text{O}_5$  with an average value of 1.35 wt%  $\text{As}_2\text{O}_5$ . However, their small volume fraction (2.53 %) in the ash makes them of lesser relevance as an As carrier. Calcite veins in unburned coal particles show also high As amounts, with an average value of 1.60 wt%  $\text{As}_2\text{O}_5$ , but their accessory occurrence (0.27 %) excludes them from being an important As reservoir. The unburned coal particles contain little As (an average of 0.10 wt%  $\text{As}_2\text{O}_5$ ) and despite their abundance (7.76 %) do not belong to important As carriers. The mineral fraction with quartz, plagioclase, iron oxides, and iron sulfides contains no arsenic and make up a rather small volume fraction (3.15 %) of the ash. The element distribution maps show an unburned coal particle with calcite veins (Fig. 5) and a vesicular glass particle (Fig. 6). Within the unburned coal particle (Fig. 5), arsenic occurs dominantly within the calcite veins, but can also be recognized in much lower concentrations in every other part of the particle. Phosphorus, most likely as phosphate which is geochemically similar to arsenate, also correlates with the calcite veins. Iron and sulfur occur together in a few spots, tentatively identified as pyrrhotite ( $\text{Fe}_{1-x}\text{S}$ ), but sulfur itself occurs in lower concentrations in the whole unburned coal particle, except for the calcite veins and mineral fragments. The vesicular glass particle in Fig. 6 is a good example of the heterogeneity of the glasses. Although the arsenic concentrations in the vesicular glasses are uniform within the resolution of the instrument at such low concentrations, other elements show a conspicuously different picture. Ca, Fe, Si and K are enriched or depleted in different domains of the vesicular glass particle.

Generally, the spot analyses and the element distribution maps show that (i) the chemical composition of the glasses is very variable. The main elements Si, Al, Ca, and Fe vary significantly (Figs. 6, 7), even within a single glass particle. (ii) Within the

glasses, arsenic shows high affinity toward Ca (Fig. 7). Glasses rich in Si and Al have essentially no As; glasses enriched in Fe are generally As-poor, although exceptions were found (Fig. 7). (iii) Arsenic is enriched in the calcite veinlets in the unburned coal particles.

Within the soil-ash mixtures, the spheroidal glasses (average 0.44 wt%  $\text{As}_2\text{O}_5$ ), unburned coal particles (0.46 wt%  $\text{As}_2\text{O}_5$ ) and their calcite veins (0.33 wt%  $\text{As}_2\text{O}_5$ ) reveal the highest As concentrations (Table 7). However, their abundance in the soil-ash mixtures is much diminished in comparison with the ash, mostly at the expense of quartz and plagioclase. The calcite crystals and the decomposing organic fragments are devoid of As. Much more interesting is the grain-binding matrix that cements the mineral grains. Even at the highest magnification achievable with the electron microprobe, no individual mineral grains could be resolved. Given the predominance of Si, Al, and Fe in the matrix and its extremely fine-grained nature, suitable minerals would be poorly crystalline clays and iron oxides. Although the As concentrations are rather low (0.05 wt%  $\text{As}_2\text{O}_5$ ), the matrix is ubiquitous and its volume fraction is rather high.

The fine-grained nature of the matrix, unclear boundaries between the matrix and the decomposing minerals and glasses, and the chemical similarity (in terms of the major elements) between the constituents precluded a thorough quantitative analysis of the soil-ash mixtures.

#### *X-ray diffraction and X-ray microdiffraction (XRD and $\mu\text{XRD}$ )*

The bulk X-ray diffraction analysis was performed as an overview for the dominant crystalline phases in the ash. In agreement with the optical microscopy results, quartz and plagioclase are the dominant crystalline phases. Despite the high intensity and excellent angular resolution of the synchrotron beam, the trace of the

XRD pattern (Fig. 8) shows clearly only the peaks of quartz. Plagioclase was identified with certainty only with a full-profile Rietveld fit (refined cell parameters:  $a = 8.187(4) \text{ \AA}$ ,  $b = 12.891(6) \text{ \AA}$ ,  $c = 7.117(3) \text{ \AA}$ ,  $\alpha = 93.62(7)^\circ$ ,  $\beta = 116.06(3)^\circ$ ,  $\gamma = 90.29(6)^\circ$  with a starting model from Wenk et al. [25]. Traces of hematite were also identified.

The  $\mu$ XRD provided or confirmed the identification of selected microscopic phases important in the context of this study. One of them were the veins in the unburned coal particles. The EMP analyses had always low totals but the  $\mu$ XRD data corroborated that the mineral within the veins is calcite (Fig. 9). Vesicular glasses are completely X-ray amorphous. Spheroidal glasses are mostly X-ray amorphous, however, some of the Ca-rich spheres show weak calcite peaks and some of the Fe-rich spheres magnetite peaks. We have also measured the constituent 7, tentatively identified as mullite based on the EMP analyses. The background-to-signal ratio, however, was too poor for a conclusive mineral identification

#### *Micro X-ray Absorption Near-Edge Structure ( $\mu$ XANES) Spectroscopy*

The XANES spectra were obtained to determine the oxidation state of the As within the different constituents. Pentavalent arsenic ( $\text{As}^{5+}$ ) accounts for more than 90 % of the total As in all measured spots (Fig. 10). Small amount of  $\text{As}^{3+}$  may be present and seen in the spectra as a weak feature in the low energy flank of the  $\text{As}^{5+}$  whiteline. We observed beam-induced reduction of As during repeated measurements but the weak pre-edge feature is visible also in the first spectrum measured at the selected spots.

## **DISCUSSION AND CONCLUSIONS**

The constituents of the studied ash are similar to those identified and described by Ramsden & Shibaoka [7], Kukier et al. [8], or Vassilev & Vassileva [26],

among others. These are unfused minerals, glasses of variable morphology and composition, high-temperature crystalline combustion products, and unburned coal particles. Among the glasses, Ramsden & Shibaoka [7] distinguished the irregular-spongy particles, vesicular and compact glasses; Kukier et al. [8] reported vesicular, spongy, spherical, and dendritic particles; Vassilev & Vassileva [26] described glassy angular, irregular, rounded, spherical, and spheroidal particles. We divided the glasses into the categories vesicular, compact, and spheroidal based on their morphology and the differences in their As content. Unburned coal particles, referred to as unburned char particles [7] or slightly changed, semi-coked, and coked particles [26] are also common in fly and bottom ashes from coal-fueled power plants where they may be derived from overrun of feed coal [7]. The unburned organic material can be further classified according to their morphology or optical properties [27] or chemical composition [28] which was not necessary for the purposes of the present study.

The predominance of  $\text{As}^{5+}$  in our samples agrees with conclusions of Huggins et al. [29], Shoji et al. [30], Huggins et al. [31] and Goodarzi et al. [3] who also studied As speciation in fly ashes. Soils amended with fly ashes were investigated by Jackson & Miller [32] who also found that  $\text{As}^{5+}$  is the dominant arsenic oxidation state.

For the question of the toxicity of As in ash and possible remediation techniques, the combination of mineralogical and geochemical comprehension of the ash is important. The bulk analyses, for example sequential extractions, seem to be insufficient for an understanding of a complex and heterogeneous materials like the ash. Our sequential extractions retrieved only 50 % of the total arsenic content through variation of pH and Eh. The other 50 % of the arsenic is bound in a much less soluble state. With microtechniques, we were able to identify the main constituents of the ash and soil-ash mixtures and quantify their arsenic load. In the

ash, the main constituents are glasses and unburned coal particles with calcite veins. The principal As carriers are vesicular and spheroidal glasses. It is important to note that the vesicular glasses contain only very little As; their role as the major As carrier is given by their sheer abundance within the ash. The calcite veinlets also contain significant amount of As but their abundance is quite low.

In the terms of the environmental impact, however, the occurrence of arsenic in almost all constituents of the ash poses a complicated question. First, bulk of the As is stored in the major constituent of the ash and therefore separation into a small volume of highly polluted and larger volume of As-free material is not possible. Extreme concentrations of As were detected in the spheroidal glasses which tend to be small (< 50  $\mu\text{m}$ ). Second, slow decomposition and devitrification of the glasses will produce a steady, long-term supply of As into the environment. These processes could be slowed down only if the ash is isolated from rain or ground water.

In the soil-ash mixtures, the arsenic carriers could not be identified with certainty, owing to the analytical difficulties. Although the composition of the soil-ash mixtures is quite similar to the ash, the proportion of ash particles is much smaller than in the ash. In this case, the abundant constituent with low As concentrations is the omnipresent grain-binding matrix. The reddish to brownish color of the matrix and its high Fe content indicates the presence of iron oxides which are well known as minerals which bind As strongly (e.g. [33], [34]).

Knowing the geology of the coal deposit and given the data presented in this work, we can track the fate of the main chemical components and As. Clays from the host rocks or inside the coal are fused [7]; refractory minerals such as quartz may be partially molten and feldspars remain unchanged [35]. The decomposition (i.e., loss of  $\text{CO}_2$ ) of calcite ( $\text{CaCO}_3$ ) and dolomite [ $\text{CaMg}(\text{CO}_3)_2$ ] begins at 500 °C and is complete by 650-950 °C, respectively [30, 34, 35]. During the decomposition of

calcite, highly reactive CaO is formed [35] and consumed at temperatures  $>1000$  °C in reactions with SiO<sub>2</sub>, Al<sub>2</sub>O<sub>3</sub>, and MgO to form pyroxenes ( $\sim$ CaMgSi<sub>2</sub>O<sub>6</sub>) [36], wollastonite (CaSiO<sub>3</sub>) [34, 36], anorthite (CaAl<sub>2</sub>Si<sub>2</sub>O<sub>8</sub>) [34, 37], and gehlenite (Ca<sub>2</sub>Al<sub>2</sub>SiO<sub>7</sub>) [34, 37]. The absence of such phases in our ash and the poor crystallinity of the tentatively identified mullite indicate that our samples did not experience such temperatures. Formation of well-crystalline mullite requires temperatures around 940-950 °C [33, 38], thus placing another, similar temperature constraint on the ash. This also means that it is likely that the bottom ash contained reactive CaO as it cooled down, was mixed with water, and transported to the tailing ponds.

The source of arsenic in the coal from Nováky is the hydrothermal arsenic sulfides, especially orpiment, As<sub>2</sub>S<sub>3</sub>. This arsenic mineralogy is unusual; arsenic is usually bound in coal in the structure of pyrite (FeS<sub>2</sub>), less commonly as As<sup>3+</sup> or As<sup>5+</sup> associated with organic material [41]. Arsenic is oxidized, volatilized, and released when the coal is being burnt; part of the arsenic is incorporated in low concentrations in the glasses, another portion reacts with Ca phases once the ash is cooled down and mixed with water.

Once deposited in the tailing ponds, the ash reacts with water and atmospheric CO<sub>2</sub>. As shown by our extractions, mild leaching with water or MgCl<sub>2</sub> solution releases a massive amount of Ca ions. These ions are probably a reaction product of the CaO generated during burning. We speculate that at least some of the Ca-rich glasses seen in our samples may be aggregates of unreacted poorly crystalline CaO. Indeed, Rodriguez-Navarro et al. [42] showed that the calcination of calcite proceeds via formation of CaO nanocrystals which coarsen only at higher temperatures. In excess Ca in the slurry delivered to the tailing ponds, As reacts to form Ca arsenates ([43], [44]). These arsenates, however, appear to be unstable with respect to calcite under



atmospheric concentrations of CO<sub>2</sub> [44] and are being replaced by this mineral. The association of As and Ca has been reported before, for example by Kukier et al. [8]. These authors reported a “slight preference of As for the fraction higher in Ca”, most likely only slight because in their coal samples, most of the arsenic was bound in pyrite and was transferred to iron oxides during combustion. Zhang et al. [45] note that lethal problems with household burning of high-As coal from China may be alleviated by addition of a calcium-based sorbent.

Hence, the dissolution of the unstable calcium arsenates embedded within the Ca-rich or calcite matrix may be responsible for the As release in the initial steps of the sequential extraction or in the contact of the ash with rain water. The slower decomposition and devitrification of the Ca-poorer glasses also releases As; this pool of arsenic appears to be partially retained in the waste or soils on the surfaces of the pre-existing or newly-formed iron oxides and clays which presumably occur within the fine-grained matrix. Further fate of the arsenic associated with iron oxides depends on the physico-chemical conditions in the soils. Arsenic is known to be released when the iron oxides are reduced or immobilized when ferric arsenates crystallize under acidic conditions [46].

## **ACKNOWLEDGEMENTS**

We thank Dr. Hiltrud Müller-Sigmund for her support during the microprobe analyses, Sigrid Hirth-Walter for her help with the AAS and Ines Kamp as well as Dr. Dirk Merten for the ICP-OES and ICP-MS measurements. We would like to thank the Karlsruhe Institute of Technology for the beam time at the Angströmquelle Karlsruhe (ANKA). We are grateful to the Albert-Ludwigs-University Freiburg and the Friedrich-Schiller-University Jena, where most of the analyses were conducted. Additionally we want to thank the anonymous reviewers for their comments and suggestions and the

editor for editorial handling. This research was funded by the DFG Research Training Group GRK 1257/1 within the Jena School of Microbial Communications (JSMC) and by the Slovak Grant Agency, grant no. VEGA 1/1034/11.

## REFERENCES

- [1] Energy Information Administration. Annual Energy Review 2009.
- [2] Matschullat J. Arsenic in the geosphere - a review. *Sci Total Environ* 2000;249:297-312.
- [3] Goodarzi F, Huggins FE, Sanei H. Assessment of elements, speciation of As, Cr, Ni and emitted Hg for a Canadian power plant burning bituminous coal. *Int J Coal Geol* 2008;74;1:1-12.
- [4] Hiller E, Jurkovič L, Kordík J, Slaninka I, Jankulár M, Majzlan J, Göttlicher J, Steininger R. Arsenic mobility from anthropogenic impoundment sediments - consequences of contamination to biota, water and sediments, Poša, Eastern Slovakia. *Appl Geochem* 2009;24:2175-2185.
- [5] Onishi H. In: Wedepohl KH. *Handbook of Geochemistry* Berlin: Springer; 1996.
- [6] Smedley PL, Kinniburgh DG. A review of the source, behavior and distribution of arsenic in natural waters. *Appl Geochem* 2002;17:517-568.
- [7] Ramsden AR, Shibaoka M. Characterization and Analyses of Individual Fly-Ash Particles from Coal-Fired Power Stations by a Combination of Optical Microscopy, Electron Microscopy and Quantitative Electron Microprobe Analysis. *Atmos Environ* 1982;16;9:2191-2206.
- [8] Kukier U, Ishak CF, Sumner ME, Miller WP. Composition and element solubility of magnetic and non-magnetic fly ash fractions. *Environ Pollut* 2003;123:255-266.
- [9] Vassilev SV, Vassileva CG, Karayigit AI, Bulut Y, Alastuey A, Querol X. Phase-mineral and chemical composition of composite samples from feed coals, bottom ashes and fly ashes at the Soma power station, Turkey. *Internat J Coal Geol* 2005;61:35-63.
- [10] Vassilev S, Menendez R. Phase-mineral and chemical composition of coal fly ashes as a basis for their multicomponent utilization. 4. Characterization of heavy concentrates and improved fly ash residues. *Fuel* 2005;84:973-991.
- [11] Chengfeng Z, Qiang Y, Junming S. Characteristics of particulate matter from emissions of four typical coal-fired power plants in China. *Fuel Process Technol* 2005;86:757-768.
- [12] Machajová Z, Verbich F, Sýkorová I. The geology, petrography and mineralogy composition of coal from Nováky deposit. *Acta Montan Slovaca* 2002;1:28-33.

- 
- [13] Halmo J, Šarkan J, Gurský S, Toma S, Lalúch I, Bogdan P. 11th mining section of the Nováky mine: New exploitation capacity in the Horná Nitra region. *Mineral Slovaca* 2010;42;1:133–140 Slovak.
- [14] Šimon L, Elečko M, Lexa J, Kohút M, Halouzká R, Gross P, Pristaš J, Konečný V, Mello J, Hók J. Explanations of the geological map 36-133 (Handlová), 35-244 (Prievidza-4), 36-131 (Ráztočno). Bratislava: Archive of Geofond; 1994 Slovak.
- [15] Pacific Northwest National Laboratory, Washington, DC. Preliminary Business Plan; District heating company for the city of Handlova, Slovakia. 1996 Jun. US Department of Energy; Contract-No.: DE-AC06-76RLO 1830.
- [16] Verbich F. Geochemistry and mineralization of Novaky coal seam. *Acta Montan Slovaca* 1998;3:378-383 (in Slovak).
- [17] Mecháček E, Petrík F. Distribution of rare elements in coal layers of Handlova-Novaky deposit. *Geologicky průzkum* 8, Praha, 1967, 266-268 (in Slovak).
- [18] Čech F, Petrík F. Classification and description of the mineral impurities in the seams of the Handlová-Nováky region. *Mineralia Slovaca IV* 1972:257-265 Slovak.
- [19] Keegan TJ, Fargo ME, Thornton I, Hong B, Colvile RN, Pesch B, Jakubis P, Nieuwenhuijsen MJ. Dispersion of As and selected heavy metals around a coal-burning power station in central Slovakia. *Sci Total Environ* 2006;358:61-71.
- [20] Satp.sk [Internet]. Bratislava: Slovak Environmental Agency; [updated 2011 Feb 16; cited 2010 Oct 02]. Environmental regional classification of the SR and endangered areas; [about 2 screens]. Available from: <http://www.sazp.sk/slovak/periodika/sprava/sprava98eng/2/kap5/hornanr.htm>
- [21] Tessier A, Campbell PGC, Bisson M. Sequential Extraction Procedure for the Speciation of Particulate Trace Metals, *Anal Chem* 1979;51;7:844.
- [22] Larson AC, von Dreele RB. GSAS. General Structure Analysis System. LANSCE, MS-H805 1994.
- [23] Hammersley AP, Svensson SO, Hanfland M, Fitch AN, Hausermann D. Two-dimensional detector software: From real detector to idealised image or two-theta scan. *High Pressure Res* 1996;14:235-218.
- [24] Ravel B, Newville M. ATHENA, ARTEMIS, HEPHAESTUS: data analysis for X-ray absorption spectroscopy using IFEFFIT. *J Synchrotron Radiat* 2005;12:537-541.
- [25] Wenk HR, Joswig W, Tagai T, Korekawa M, Smith BK. The average structure of An 62-66 labradorite. *Am Mineral* 1980;65:81-95.
- [26] Vassilev SV, Vassileva CG. Methods for characterization of composition of fly ashes from coal-fired power stations: A critical overview. *Energ Fuel* 2005;19:1084-1098.
- [27] Vassilev SV, Menendez R, Borrego AG, Diaz-Somoano M, Martinez-Tarazone MR. Phase-mineral and chemical composition of coal fly ashes as a basis for their multicomponent utilization. 3. Characterization of magnetic and char concentrates. *Fuel* 2004;83:1563-1583.

- 
- [28] Rose NL, Juggins S, Watt J. The characterisation of carbonaceous fly-ash particles from major European fossil-fuel types and applications to environmental samples. *Atmos Environ* 1999;33:2699-2713.
- [29] Huggins FE, Shah N, Zhao J, Lu F, Huffman GP. Nondestructive Determination of Trace Element Speciation in Coal and Coal Ash by XAFS Spectroscopy. *Energ Fuel* 1993;7:482-489.
- [30] Shoji T, Huggins FE, Huffman GP, Linak WP, Miller CA. XAFS Spectroscopy Analysis of Selected Elements in Fine Particulate Matter Derived from Coal Combustion, *Energ Fuel* 2002;16:325-329.
- [31] Huggins FE, Senior CL, Chu P, Ladwig K, Huffman GP. Selenium and arsenic speciation in fly ash from full-scale coal-burning utility plants. *Environ Sci Technol* 2007;41:3284-3289.
- [32] Jackson BP, Miller WP. Soluble Arsenic and Selenium Species in Fly Ash/Organic Waste-Amended Soils Using Ion Chromatography-Inductively Coupled Plasma Mass Spectrometry. *Environ Sci Technol* 1999;33(2);270-275.
- [33] Majzlan J, Lalinská B, Chovan M, Jurkovič L, Milovská S, Göttlicher J. The formation, structure, and ageing of As-rich hydrous ferric oxide at the abandoned Sb deposit Pezinok (Slovakia). *Geochim Cosmochim Acta* 2007;71:4206-4220.
- [34] Anawar HM, Garcia-Sanchez A, Regina IS, Mihaljevič M, Majzlan J, Moyano A. Assessment of arsenic fractionation, mobility, and bioavailability in mining-affected soils, and remediation measures. *Land Contamin Reclam* 2010;18:279-292.
- [35] Reifenstein AP, Kahraman H, Coin CDA, Calos NJ, Miller G, Uwins P. Behaviour of selected minerals in an improved ash fusion test: quartz, potassium feldspar, sodium feldspar, kaolinite, illite, calcite, dolomite, siderite, pyrite and apatite. *Fuel* 1999;78:1449-14461.
- [36] Peters T, Iberg R. Mineralogical changes during firing of calcium-rich brick clays. *Am Ceram Soc Bull* 1978;57:503-509.
- [37] Grapes R. *Pyrometamorphism*. Berlin: Springer; 2006
- [38] Chinchón JS, Querol X, Fernández-Turiel JL, López-Soler A. Environmental impact of mineral transformations undergone during coal combustion. *Environ Geol Water Sci* 1991;18:11-15.
- [39] Majoral MC, Izquierdo MT, Andrés JM, Rubio R. Aluminosilicates transformations in combustion followed by DSC. *Thermochim Acta* 2001;373:173-180.
- [40] Lee S, Kim YJ, Moon HS. Phase transformation sequence from kaolinite to mullite investigated by an energy-filtering transmission electron microprobe. *J Am Ceram Soc* 1999;82;10:2841-2848.
- [41] Kolker A, Huggins FE, Palmer CA, Shah N, Crowley SS, Huffman GP, Finkelman RB. Mode of occurrence of arsenic in four US coals. *Fuel Process Technol* 2000;63:167-178.
- [42] Rodriguez-Navarro C, Ruiz-Agudo E, Luque A, Rodriguez-Navarro AB, Ortega-Huertas M. Thermal decomposition of calcite: Mechanisms of formation and textural evolution of CaO nanocrystals. *Am Mineral* 2009;94, 578–593.

- [43] Bothe JV, Brown PW. Arsenic immobilization by calcium arsenate formation. *Environ Sci Technol* 1999;33:3806-3811.
- [44] Welham NJ, Malatt KA, Vukcevic S. The stability of iron phases presently used for disposal from metallurgical systems - A review. *Miner Eng* 2000;13:911-931.
- [45] Zhang J, Zhao Y, Huang W, Li Y, Song ., Dai S, Zhao F, Zheng C. Arsenic emission of high-arsenic coal combustion from southwestern Guizhou, China. *Chinese Journal of Geochemistry* 2006;25 Suppl 49.
- [46] Langmuir D, Mahoney J, Rowson J. Solubility products of amorphous ferric arsenate and crystalline scorodite ( $\text{FeAsO}_4 \cdot 2\text{H}_2\text{O}$ ) and their application to arsenic behaviour in buried mine tailings. *Geochim Cosmochim Ac* 2006;70:2942-2956.

## FIGURE CAPTIONS

Figure 1: A: Coal deposits of Nováky and Handlová, modified after Halmo et al. (2010). Inset shows the position of Nováky in Slovakia. B: An aerial photograph of the studied area with sampling locations. The Nitra river is marked for clarity by a thick white line.

Figure 2: Soil profile of the ash flow near Zemianske Kostolány covered by soil. Our samples of the ash-soil mixtures were collected from the ash buried under soil.

Figure 3: Fraction of As extracted in each step of the sequential extraction normalized to the total arsenic concentration ( $As_{\text{tot,digestion}}$ , Table 2) for a sample of the lagooned ash waste (Bo 2) and an ash-soil mixture (Bo 5). Numbers in the sectors are the steps of the sequential extraction (see Table 1).

Figure 4: Back-scattered electron images of an (A) unburned coal particle in ash, (B) calcite veins within an unburned coal particle in ash, (C) vesicular glass particle in ash, (D) spheroidal glass particle in ash, (E) grain-binding matrix in soil-ash mixture and (F) calcite crystal in soil-ash mixture.

Figure 5: Element distribution map of an unburned coal particle with calcite veins in the ash.

Figure 6: Element distribution map of a vesicular glass particle in the ash.

Figure 7: A triangular plot of spheroidal (grey) and vesicular (black) glasses. The circle size is scaled to the As concentration in the glass.

Figure 8: Bulk X-ray diffraction (synchrotron radiation,  $\lambda = 1.18241 \text{ \AA}$ ). The ticks below the pattern mark the calculated positions of diffraction peaks; top row – hematite, middle – plagioclase, bottom – quartz.

Figure 9:  $\mu$ XRD pattern ( $\lambda = 0.886 \text{ \AA}$ ) of calcite of an unburned coal particle with calcite veins. The ticks below the pattern mark the calculated positions of diffraction peaks of calcite.

Figure 10: XANES spectra of constituents of the lagooned ash waste (bottom four spectra) and the ash-soil mixtures (middle four spectra), compared to the spectra of references with  $\text{As}^{3+}$  (top spectrum, thin line) and  $\text{As}^{5+}$  (top spectrum, thick line). All spectra were normalized to an edge jump of 1.

Table 1: Mineralogical composition of the lignite coal after <sup>a</sup>Verbich (1998)[16] and <sup>b</sup>Mecháček & Petrík (1967) [17].

class	minerals
silicates	biotite <sup>a</sup> , chlorite <sup>a</sup> , amphibole <sup>a</sup> , muscovite <sup>a</sup> , garnet <sup>a</sup> , plagioclase <sup>a</sup> , feldspar <sup>a</sup> , hydromica <sup>a</sup> , pyroxenes <sup>a</sup>
carbonates	calcite <sup>a</sup> , siderite <sup>a</sup> , manganocalcite <sup>a</sup>
sulfates	gypsum <sup>a</sup> , anhydrite <sup>a</sup> , melanterite <sup>a</sup>
oxides/hydrox.	quartz <sup>a</sup> , magnetite <sup>a</sup> , opal <sup>a</sup> , limonite <sup>a</sup>
sulfides	pyrite <sup>a</sup> , marcasite <sup>a</sup> , realgar <sup>a</sup> , orpiment <sup>a</sup> , arsenopyrite <sup>b</sup>
phosphates	apatite <sup>a</sup> , phosphorite <sup>a</sup>
clay minerals	kaolinite <sup>a</sup> , illite <sup>a</sup> , montmorillonite <sup>a</sup> , halloysite <sup>a</sup>

Table 2: Sampling positions with GPS coordinates and chemical composition of the ash waste and soil-ash mixtures measured by X-ray fluorescence (XRF) spectrometry. XRF data in weight %.

sample	ash			soil-ash mixtures		
	Bo 1	Bo 2	Bo 3	Bo 4	Bo 5	Bo 6
longitude	48.688500°	48.688194°	48.689444°	48.689139°	48.688583°	48.688000°
latitude	18.506722°	18.506444°	18.516417°	18.517028°	18.518556°	18.519583°
SiO <sub>2</sub>	54.20	53.94	54.21	55.84	57.99	55.67
TiO <sub>2</sub>	1.44	1.47	2.48	2.29	2.21	1.97
Al <sub>2</sub> O <sub>3</sub>	17.09	17.32	15.92	16.24	16.09	16.10
CaO	10.48	10.48	11.43	9.54	9.11	11.11
FeO	8.85	8.83	8.34	8.03	6.95	7.35
MgO	1.62	1.72	2.05	2.09	1.63	1.75
MnO	0.34	0.35	0.36	0.35	0.35	0.36
BaO	0.21	0.25	0.22	0.26	0.23	0.25
SrO	0.13	0.12	0.12	0.10	0.10	0.10
K <sub>2</sub> O	3.54	3.45	3.17	3.62	3.61	3.81
Na <sub>2</sub> O	0.64	0.61	0.81	0.85	0.67	0.69
SO <sub>2</sub>	0.84	0.79	0.17	0.13	0.21	0.19
As <sub>2</sub> O <sub>5</sub>	0.27	0.32	0.27	0.28	0.38	0.30
P <sub>2</sub> O <sub>5</sub>	0.25	0.26	0.33	0.24	0.32	0.23

Table 3: Sequential extraction procedure used in this study (after Tessier et al. 1979).

step	sample	added solutions	extraction	temp.
1	1 g	add 8 mL MgCl <sub>2</sub> (1 M), pH 7	agitate 1 h	25°C
2	resid. step 1	add 8 mL NaCH <sub>3</sub> COO (1 M), pH 5	agitate 5 h	25°C
3	resid. step 2	add 20 mL Na <sub>2</sub> S <sub>2</sub> O <sub>3</sub> (0.3 M) + sodium citrate (0.175 M) + citric acid (0.025 M)	heat 6 h	96°C
4	resid. step 3	add 3 mL HNO <sub>3</sub> (0.02 M)	heat 2 h	85°C
		add 5 mL H <sub>2</sub> O <sub>2</sub> (30%, pH 2)	heat 3 h	85°C
		add 3 mL H <sub>2</sub> O <sub>2</sub> (30%, pH 2)	agitate 30 min	25°C
		add 5 mL NH <sub>4</sub> OAc (3.2 M) in HNO <sub>3</sub> (20 %) and dilute to 20 mL		

Table 4: Arsenic concentration (in mg/kg) determined by the total digestion ( $As_{tot,digestion}$ ) and each step of the sequential extraction of the ash and soil-ash mixtures measured by atomic absorption spectroscopy (AAS).  $As_{tot,seq.ex}$  shows the total arsenic retrieved in all steps of the sequential extraction.

sample	ash			soil-ash mixtures		
	Bo 1	Bo 2	Bo 3	Bo 4	Bo 5	Bo 6
$As_{tot,digestion}$	1136	1411	1109	1078	1381	1196
step 1	43.84	63.96	12.58	8.56	12.11	9.78
step 2	178.59	210.62	59.99	51.3	75.52	2.52
step 3	280.17	365.16	433.28	401.69	522.38	367.11
step 4	49.52	62.05	57.67	38.05	74.39	77.47
$As_{tot,seq.ex}$	552.12	701.79	563.52	499.6	684.4	456.88

Table 5: Concentrations of Al, Ca, Fe, and Mn (in mg/kg) released from the ash (sample Bo 1) in each step of the sequential extraction after Tessier et al. 1979 measured by ICP-OES.

	Al	Ca	Fe	Mn
step 1	26	14885	17	0
step 2	771	4895	681	51
step 3	2164	3046	5079	84
step 4	5489	4001	3452	76



Table 6: Electron microprobe analysis for the constituents of the ash.  $n$  is the number of analyses averaged, the value in parenthesis is one standard deviation. All analytical data in weight %. The row volume % reports the estimate of the proportions of the constituents determined by areal integration of back-scattered electron images. The bottom row is the amount of As in each constituent in ppm.

	unburned coal particles	calcite veins	vesicular and compact glasses	spheroidal glasses	quartz	feldspar	mullite
$n$	24	54	39	80	14	19	6
SiO <sub>2</sub>	11.82(14.97)	2.92(6.84)	48.16(27.64)	20.17(19.93)	99.61(0.41)	55.93(3.34)	23.87(0.66)
TiO <sub>2</sub>	0.18(0.48)	0.06(0.14)	0.56(0.71)	0.54(1.23)	0.01(0.01)	0.12(0.22)	2.39(0.14)
Al <sub>2</sub> O <sub>3</sub>	5.29(6.72)	1.21(2.73)	14.36(8.24)	8.92(8.53)	0.01(0.01)	27.15(2.60)	21.43(1.00)
CaO	3.98(5.06)	32.89(19.88)	5.00(6.53)	23.09(21.58)	0.02(0.01)	8.69(4.82)	0.35(0.06)
FeO	6.94(20.04)	10.65(24.64)	16.64(25.34)	20.92(26.89)	0.05(0.03)	1.48(2.17)	0.40(0.03)
MgO	0.93(0.46)	1.43(1.35)	2.24(3.11)	2.41(2.69)	0.00(0.00)	0.58(1.02)	0.30(0.01)
MnO	0.06(0.14)	0.08(0.19)	0.27(0.71)	0.30(0.58)	0.00(0.01)	0.01(0.02)	0.00(0.01)
SO <sub>2</sub>	3.92(3.92)	1.71(1.04)	2.24(9.39)	1.48(5.83)	0.01(0.01)	0.03(0.04)	0.05(0.00)
As <sub>2</sub> O <sub>5</sub>	0.10(0.19)	1.60(1.13)	0.13(0.49)	1.35(2.57)	0.01(0.01)	0.00(0.00)	0.00(0.00)
P <sub>2</sub> O <sub>5</sub>	0.07(0.07)	0.29(0.25)	0.20(0.20)	0.44(0.47)	0.01(0.02)	0.03(0.02)	0.14(0.05)
total	33.29(33.29)	52.84(21.56)	89.80(13.28)	79.60(18.78)	99.73(0.40)	94.02(1.84)	48.93(1.55)
volume %	7.76	0.27	86.29	2.53	quartz, feldspar, mullite together: 3.15		
As (ppm)	51	28	731	223	quartz, feldspar, mullite together: 2		

Table 7: Electron microprobe analysis for the constituents of the soil-ash mixtures.  $n$  is the number of analyses averaged, the value in parenthesis is one standard deviation. All analytical data in weight %.

	unburned coal particles	calcite veins	vesicular glasses	spheroidal glasses	quartz	feldspar	matrix	organic compounds
$n$	12	11	19	40	32	14	50	4
SiO <sub>2</sub>	20.04(10.66)	0.11(0.28)	49.51(11.39)	29.25(12.92)	100.09(0.92)	59.69(9.17)	46.24(14.37)	0.10(0.04)
TiO <sub>2</sub>	0.14(0.08)	0.00(0.01)	0.82(0.97)	1.54(12.92)	0.01(0.01)	0.83(0.83)	0.69(1.09)	0.07(0.03)
Al <sub>2</sub> O <sub>3</sub>	7.70(4.78)	0.16(0.20)	22.93(4.94)	14.30(6.78)	0.03(0.05)	24.92(7.36)	16.89(6.39)	0.22(0.13)
CaO	5.99(4.45)	32.76(24.50)	8.10(5.83)	13.69(10.37)	0.02(0.01)	0.36(4.68)	1.13(0.65)	2.63(1.11)
FeO	1.99(1.16)	0.08(0.08)	7.35(5.63)	21.28(18.52)	0.06(0.04)	1.10(1.78)	5.43(1.92)	0.13(0.07)
MgO	0.81(0.74)	4.30(8.90)	2.89(1.40)	3.72(3.03)	0.00(0.00)	0.57(0.57)	1.60(0.64)	0.17(0.17)
MnO	0.04(0.05)	0.01(0.01)	0.09(0.07)	0.28(0.27)	0.00(0.01)	0.01(0.01)	0.10(0.19)	0.01(0.02)
SO <sub>2</sub>	0.39(0.27)	1.08(0.22)	0.05(0.06)	0.11(0.22)	0.01(0.01)	0.02(0.02)	0.11(0.16)	0.90(0.36)
As <sub>2</sub> O <sub>5</sub>	0.46(0.54)	0.33(0.20)	0.03(0.08)	0.44(0.79)	0.00(0.01)	0.01(0.02)	0.05(0.07)	0.00(0.00)
P <sub>2</sub> O <sub>5</sub>	0.22(0.27)	0.08(0.09)	0.61(2.22)	0.56(1.74)	0.02(0.02)	0.08(0.08)	0.30(0.33)	0.02(0.02)
total	37.78(20.32)	38.91(25.25)	92.38(5.85)	85.18(18.80)	100.25(0.93)	89.57(3.93)	72.56(13.24)	4.26(1.67)

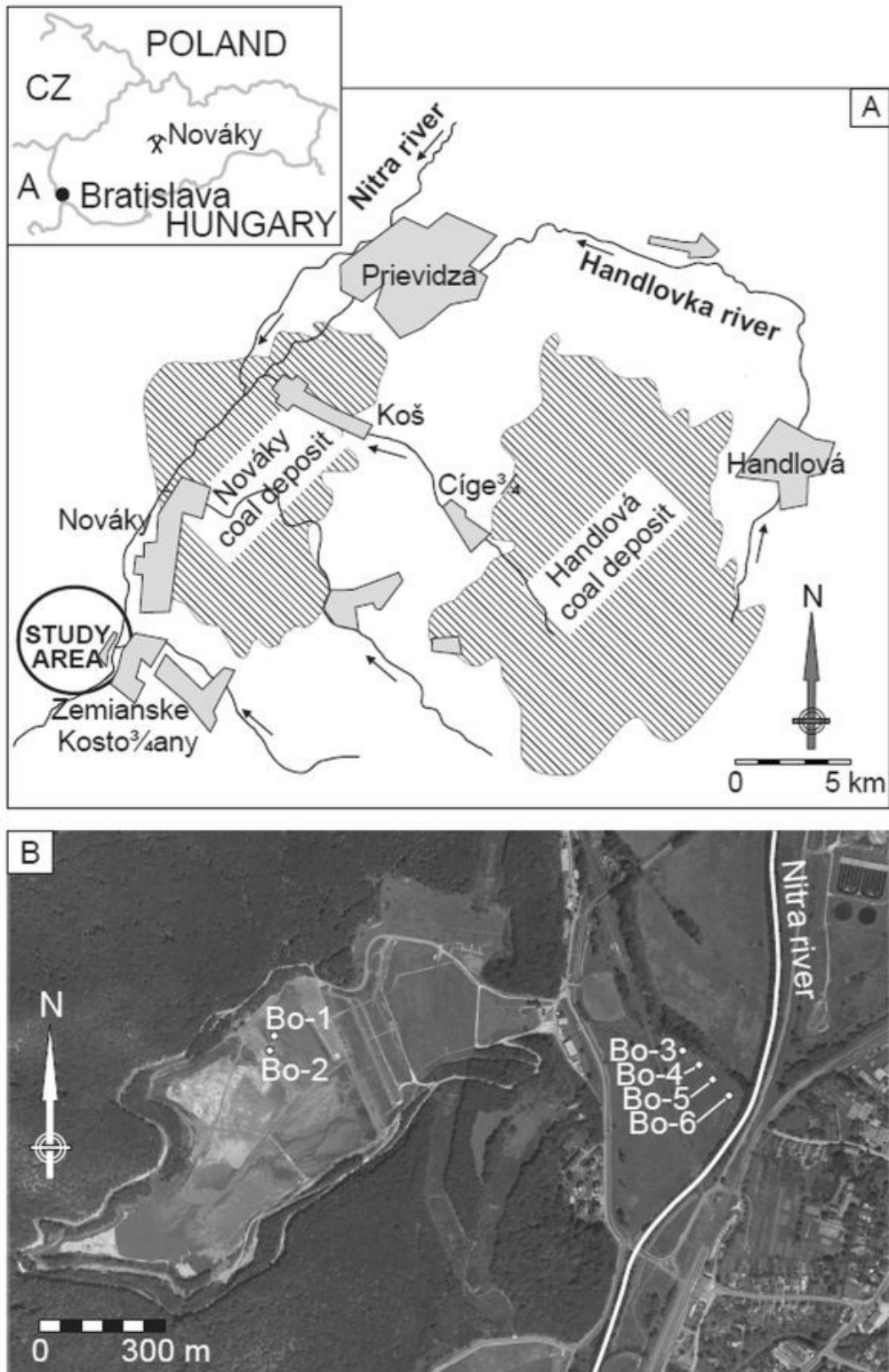


Figure 1: A: Coal deposits of Nováky and Handlová, modified after Halmo et al. (2010). Inset shows the position of Nováky in Slovakia. B: An aerial photograph of the studied area with sampling locations. The Nitra river is marked for clarity by a thick white line.



Figure 2: Soil profile of the ash flow near Zemianske Kostol'any covered by soil. Our samples of the ash-soil mixtures were collected from the ash buried under soil.

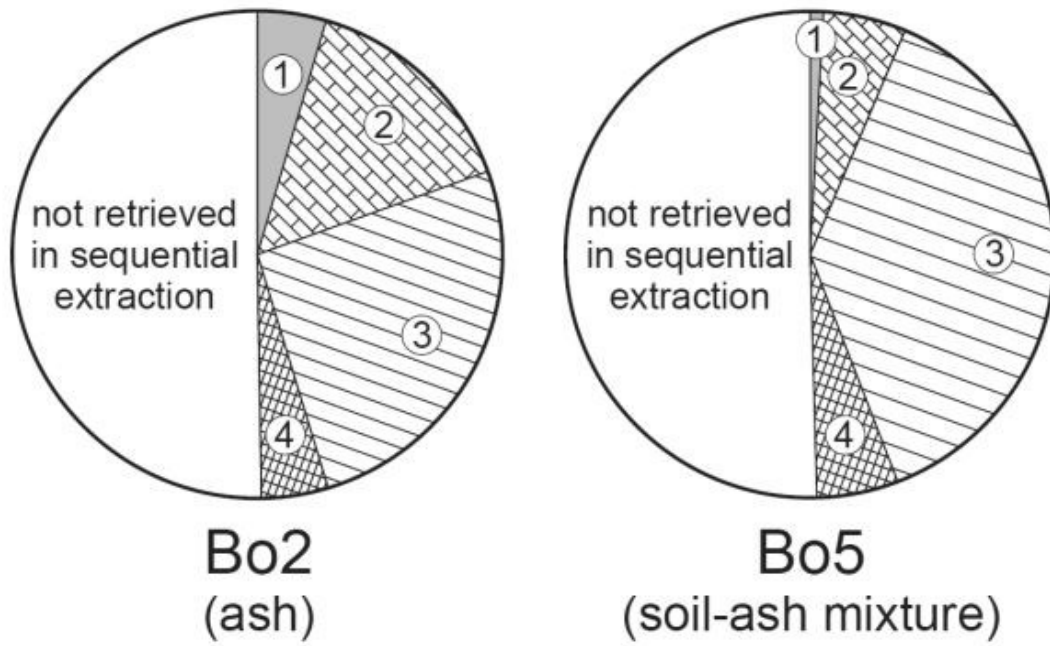


Figure 3: Fraction of As extracted in each step of the sequential extraction normalized to the total arsenic concentration ( $As_{\text{tot,digestion}}$ , Table 2) for a sample of the lagooned ash waste (Bo 2) and an ash-soil mixture (Bo 5). Numbers in the sectors are the steps of the sequential extraction (see Table 1).

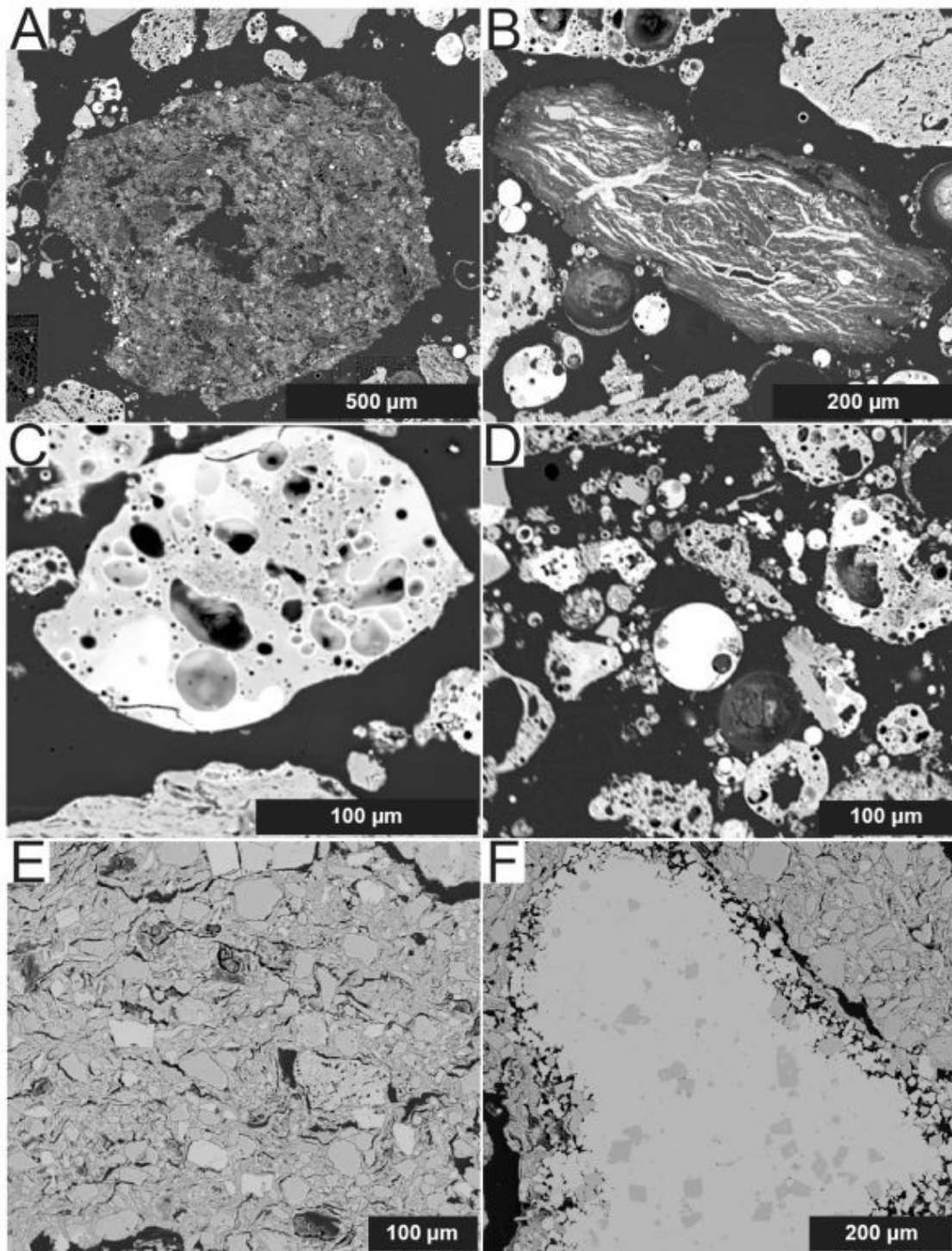


Figure 4: Back-scattered electron images of an (A) unburned coal particle in ash, (B) calcite veins within an unburned coal particle in ash, (C) vesicular glass particle in ash, (D) spheroidal glass particle in ash, (E) grain-binding matrix in soil-ash mixture and (F) calcite crystal in soil-ash mixture.

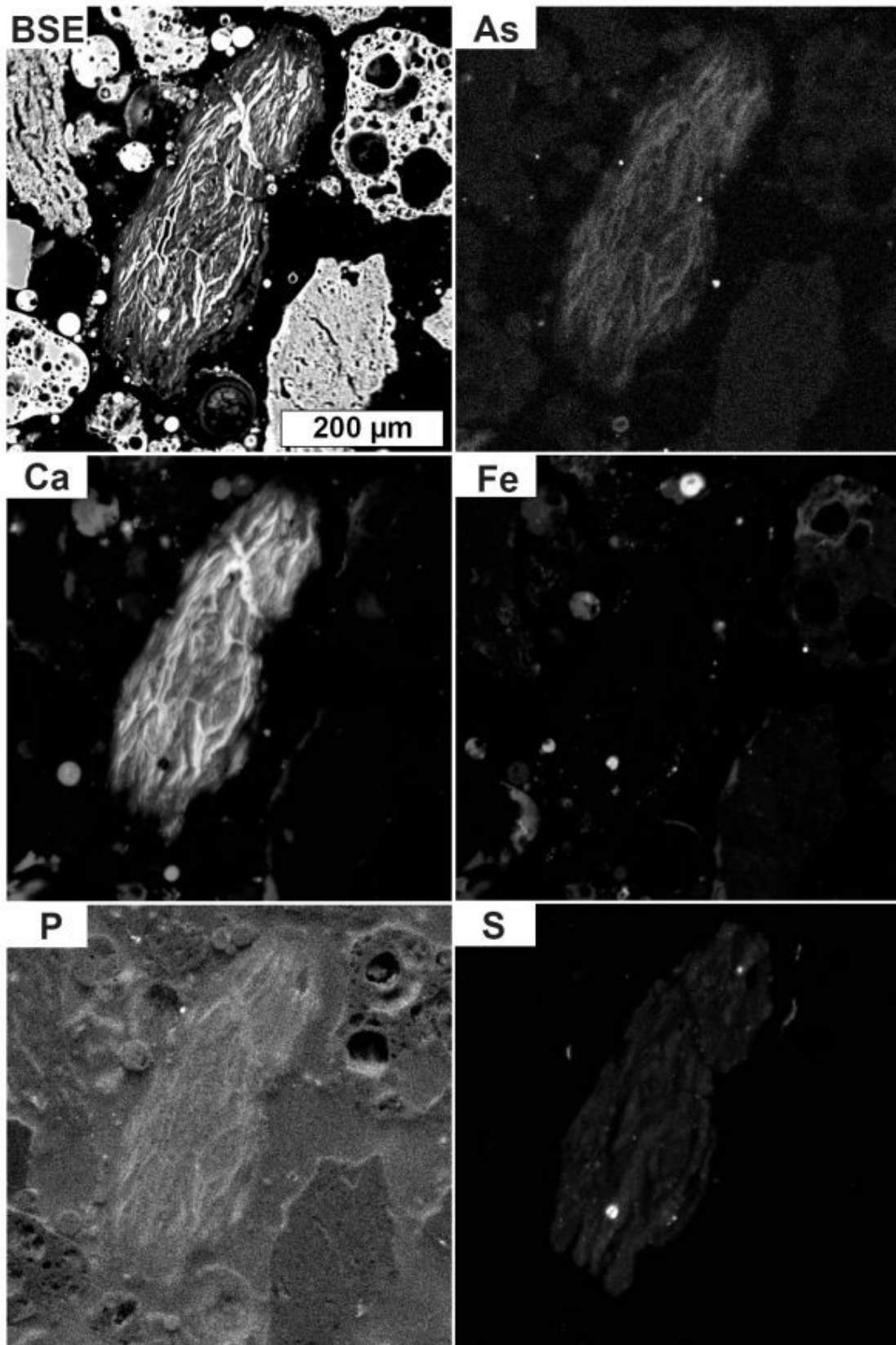


Figure 5: Element distribution map of an unburned coal particle with calcite veins in the ash.

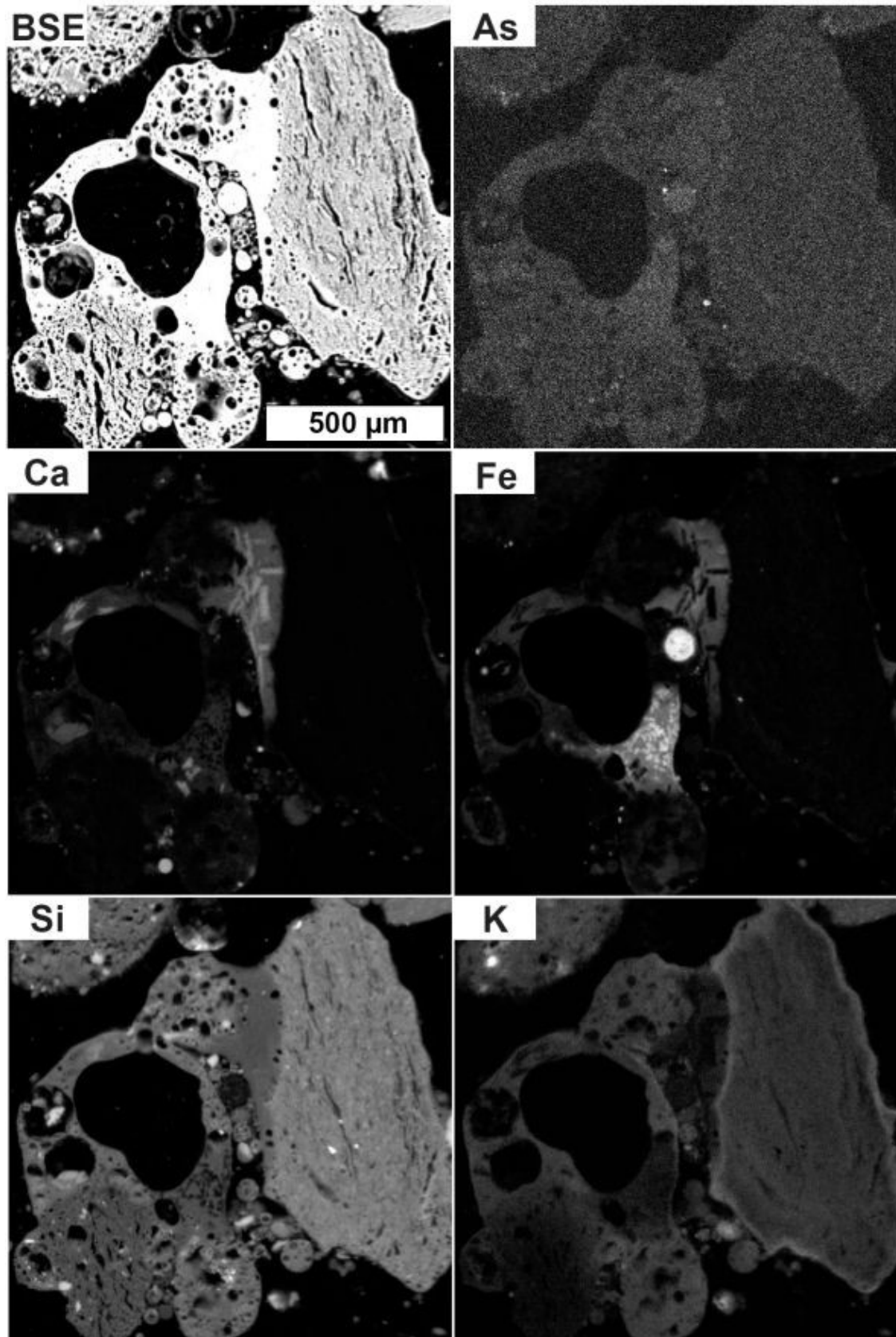


Figure 6: Element distribution map of a vesicular glass particle in the ash.

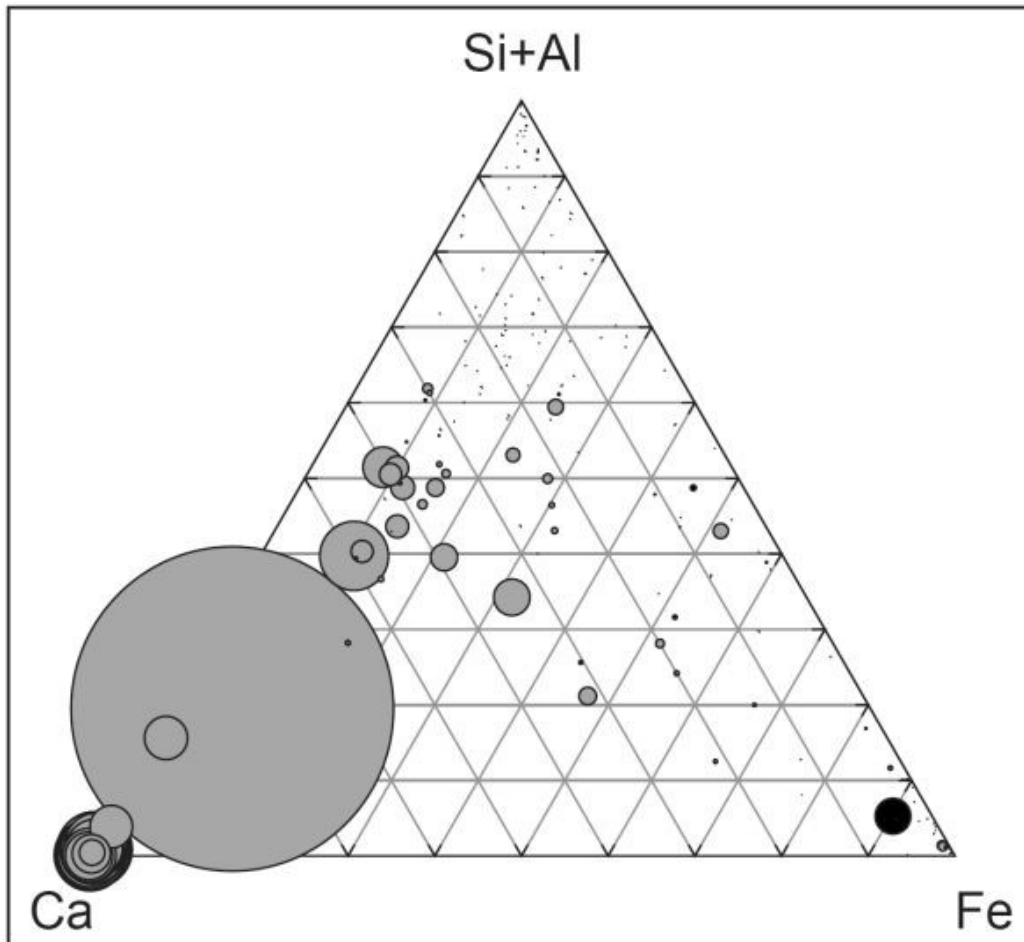


Figure 7: A triangular plot of spheroidal (grey) and vesicular (black) glasses. The circle size is scaled to the As concentration in the glass.



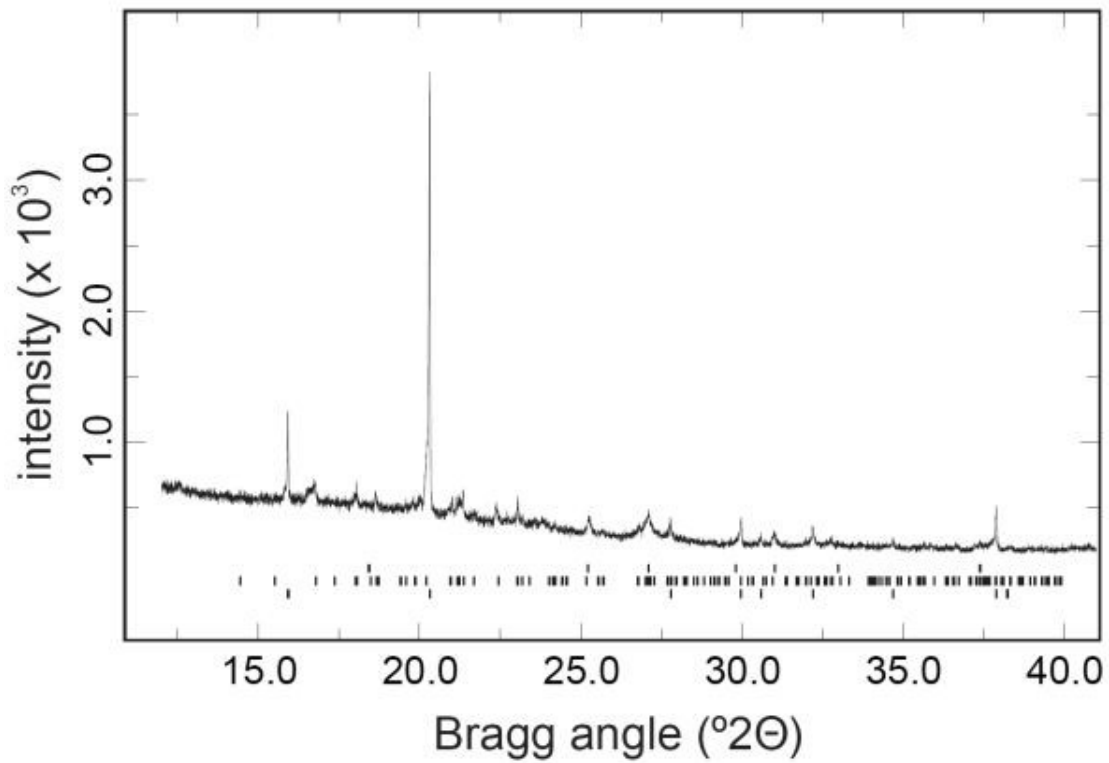


Figure 8: Bulk X-ray diffraction (synchrotron radiation,  $\lambda = 1.18241 \text{ \AA}$ ). The ticks below the pattern mark the calculated positions of diffraction peaks; top row – hematite, middle – plagioclase, bottom – quartz.

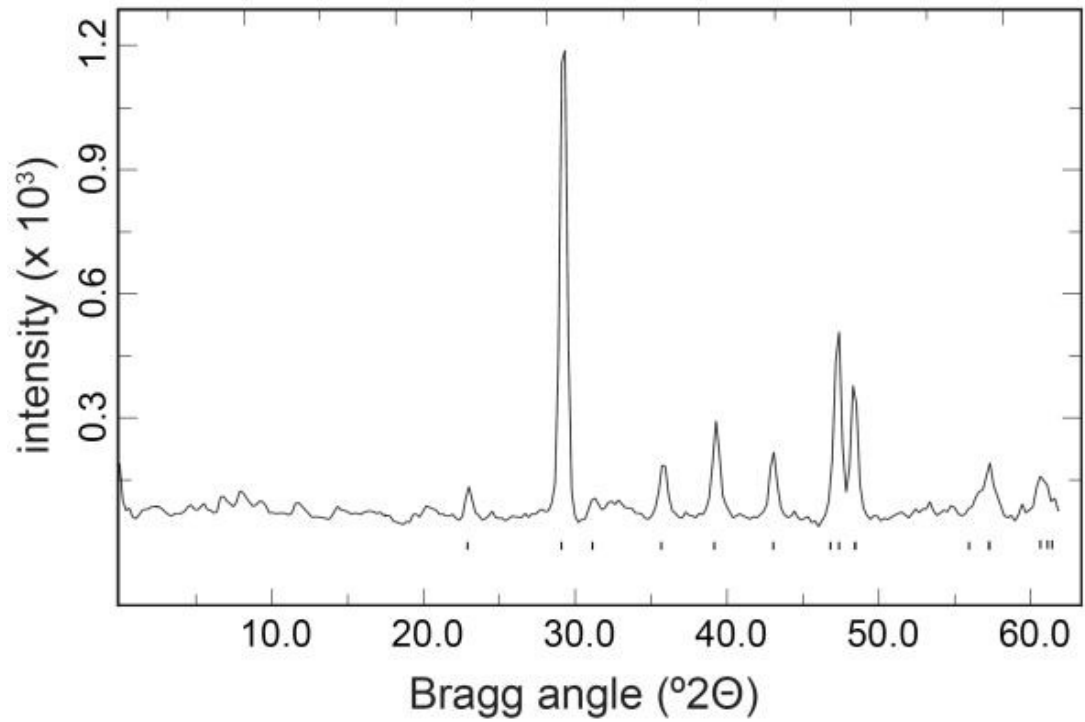


Figure 9:  $\mu$ XRD pattern ( $\lambda = 0.886 \text{ \AA}$ ) of calcite of an unburned coal particle with calcite veins. The ticks below the pattern mark the calculated positions of diffraction peaks of calcite.

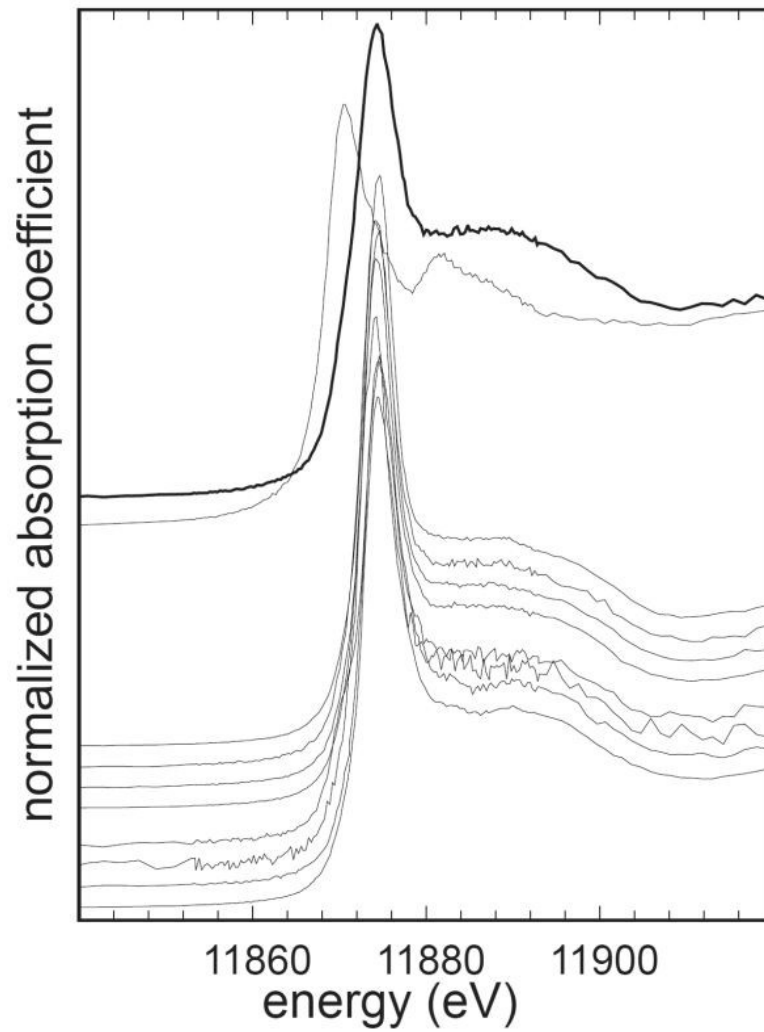


Figure 10: XANES spectra of constituents of the lagooned ash waste (bottom four spectra) and the ash-soil mixtures (middle four spectra), compared to the spectra of references with  $As^{3+}$  (top spectrum, thin line) and  $As^{5+}$  (top spectrum, thick line). All spectra were normalized to an edge jump of 1.

## **Chapter two**

## Structural incorporation of As<sup>5+</sup> into hematite

Ralph M. Bolanz<sup>1\*</sup>, Maria Wierzbicka-Wieczorek<sup>1</sup>, Mária Čaplovičová<sup>2</sup>, Peter Uhlík<sup>2</sup>,  
Jörg Göttlicher<sup>3</sup>, Ralph Steininger<sup>3</sup>, and Juraj Majzlan<sup>1</sup>

<sup>1</sup>Friedrich-Schiller-University Jena, Institute of Geosciences, 07745 Jena, Germany

<sup>2</sup>Comenius University in Bratislava, Department of Economic Geology, 842 15 Bratislava, Slovakia

<sup>3</sup>Institute of Synchrotron Radiation, Karlsruhe Institute of Technology, 76344 Eggenstein-Leopoldshafen,  
Germany

\* corresponding author: Tel. +49-3641-948704, fax +49-3641-948602, email  
address: [Ralph.Bolanz@uni-jena.de](mailto:Ralph.Bolanz@uni-jena.de)

### *Authors contact details*

Maria Wierzbicka-Wieczorek:	<a href="mailto:Maria.Wierzbicka-Wieczorek@uni-jena.de">Maria.Wierzbicka-Wieczorek@uni-jena.de</a>
Mária Čaplovičová:	<a href="mailto:Caplovicova@fns.uniba.sk">Caplovicova@fns.uniba.sk</a>
Peter Uhlík:	<a href="mailto:Uhlik@fns.uniba.sk">Uhlik@fns.uniba.sk</a>
Jörg Göttlicher:	<a href="mailto:joerg.goettlicher@kit.edu">joerg.goettlicher@kit.edu</a>
Ralph Steininger:	<a href="mailto:ralph.steininger@kit.edu">ralph.steininger@kit.edu</a>
Juraj Majzlan:	<a href="mailto:Juraj.Majzlan@uni-jena.de">Juraj.Majzlan@uni-jena.de</a>

### *Rational*

Arsenic is one of the most widespread contaminants and a well known poison. The adsorption of As<sup>5+</sup> to the surface of iron oxides was studied in detail, but the possibility of As<sup>5+</sup> incorporation in iron oxides was never considered. This manuscript addresses the issues of ES&T, since it contains a complete new and unknown immobilization mechanism for As<sup>5+</sup>, is of significant environmental concern and contains information about a new disposal technique for As<sup>5+</sup>.

Submitted to: December 2012  
Reviews received: April 2013  
Revised: June 2013  
Accepted: July 2013

Reproduced according to the rules of Environmental Science and Technology, submitted for publication. Unpublished work copyright 2012 American Chemical Society.

**ABSTRACT**

Hematite ( $\alpha\text{-Fe}_2\text{O}_3$ ) is one of the most common iron oxides and a sink for the toxic metalloid arsenic. Arsenic can be immobilized by adsorption to the hematite surface, however, the incorporation of As in hematite was never seriously considered. In our study we present evidence that, besides adsorption, the incorporation of As into the hematite crystals can be of great relevance for As immobilization. With the coupling of nano-resolution techniques and X-ray absorption spectroscopy the presence of As (up to 1.9 wt. %) within the hematite crystals could be demonstrated. The incorporated  $\text{As}^{5+}$  displays a short-range order similar to angelellite-like clusters, epitaxially intergrown with hematite. Angelellite ( $\text{Fe}_4\text{As}_2\text{O}_{11}$ ), a triclinic iron arsenate with structural relations to hematite, can epitaxially intergrow along the (210) plane with the (0001) plane of hematite. This structural composite of hematite and angelellite-like clusters represents a new immobilization mechanism and potentially long-lasting storage facility for  $\text{As}^{5+}$  by iron oxides.

## INTRODUCTION

Arsenic is one of the world's most widespread inorganic contaminants and represents a considerable risk potential for human health and the biosphere as a whole [1]. Although, arsenic in its trivalent form ( $\text{As}^{3+}$ ) is considered to be more toxic than in the pentavalent state ( $\text{As}^{5+}$ ) [1], in oxidized systems near or at the surface,  $\text{As}^{5+}$  dominates over  $\text{As}^{3+}$  [1]. When  $\text{As}^{5+}$  is released into the environment and reaches soils or sediments, it can be immobilized by adsorption to the surfaces of iron oxide minerals (e.g. [2,3,4]). However, the possibility of  $\text{As}^{5+}$  incorporation into iron oxides received much less attention. Adsorption and the formation of inner- or outer-sphere complexes are short-term immobilization mechanisms for  $\text{As}^{5+}$  in systems where iron oxides existed prior to the contamination. In many natural systems, however, the neoformation and recrystallization of iron oxides proceeds at all times, often simultaneously with the contamination. The neoformation of iron oxides typically starts with the oxidation of ferrous iron, supplied from weathering bedrock, and the deposition of ferric iron as poorly crystalline iron oxides, ferrihydrite ( $\sim\text{FeOOH}\cdot n\text{H}_2\text{O}$ ) [5,6,7]. Ferrihydrite itself is metastable and transforms with time to goethite ( $\alpha\text{-FeOOH}$ ) or hematite ( $\alpha\text{-Fe}_2\text{O}_3$ ) [7]. Previous studies show that in the presence of  $\text{As}^{5+}$ , the transformation of ferrihydrite to goethite and hematite is retarded, and the transformation product hematite ( $\alpha\text{-Fe}_2\text{O}_3$ ) is favored (e.g. [8,9]).

The structural incorporation of  $\text{P}^{5+}$  into hematite was investigated previously by Galvez *et al.* (1999) [10]. Because  $\text{P}^{5+}$ , like  $\text{As}^{5+}$ , is tetrahedrally coordinated by oxygen, has the same electronic configuration, and shows the analogous chemical species in aqueous solution,  $\text{P}^{5+}$  is often referred as a chemical analogue to  $\text{As}^{5+}$ .



The incorporation of phosphate into hematite was positively correlated with iron loss and hydrogen gain [10]. These observations led to the conclusion that the crystal structure of hematite could hold  $P^{5+}$ , namely that  $P^{5+}$  could occupy the unoccupied tetrahedral interstices of the hematite structure [10]. Since  $P^{5+}$  and  $As^{5+}$  are chemically similar, it was assumed that this model could also be valid for  $As^{5+}$  [11].

In this work, we investigated the  $As^{5+}$  incorporation into the crystal structure of hematite on products from syntheses in aqueous suspension by transmission electron microscopy (TEM), and X-ray absorption spectroscopy (XAS). We examined the possibility of the insertion of  $As^{5+}$  into the otherwise unoccupied tetrahedral interstices (cf. [10]). In addition, a number of iron arsenates were used as reference compounds for the XAS work and additional structural models were constructed by considering As-containing phases, which could intergrow in a regular, crystallographic precisely defined manner with hematite. A careful statistical treatment of the models allows deciphering the mode of  $As^{5+}$  incorporation into hematite and shows that incorporation is a viable option for immobilization of As under natural settings.

## **EXPERIMENTAL**

The precursor for all As-doped hematite samples in this study was two-line ferrihydrite (subsequently referred to as ferrihydrite), synthesized after Schwertmann & Cornell (2000) [12]. A mass of 10.1 g  $Fe(NO_3)_3 \cdot 9H_2O$  was dissolved in 200 mL deionized water and transformed into ferrihydrite by adding 45 mL 5 M potassium hydroxide (KOH) solution rapidly under constant stirring. The suspension volume was brought to 490 mL with deionized water with an end-point pH of about 13 and

afterwards adjusted to 500 mL with deionized water. The so synthesized ferrihydrite slurry was immediately adjusted to pH 4 by adding 65 % HNO<sub>3</sub> and doped with pre-selected volumes of a 15 mM As<sub>2</sub>O<sub>5</sub> solution, except for the blank, where no As<sub>2</sub>O<sub>5</sub> solution was added. The synthesized ferrihydrite was not washed in order to maintain the calculated Fe concentration and therefore the Fe/As ratio constant. The volumes of the As<sub>2</sub>O<sub>5</sub> solutions were calculated to reach at the As<sup>5+</sup> molarity of 0.00 mM (sample HEM<sub>0.00</sub>), which represents the control, 0.23 mM (HEM<sub>0.23</sub>), 0.75 mM (HEM<sub>0.75</sub>), and 2.25 mM (HEM<sub>2.25</sub>) after adjusting to 500 mL with deionized water. After bringing the volume to about 490 mL, the pH was checked and adjusted again to pH 4 if necessary by adding 65 % HNO<sub>3</sub> or 5 M KOH solution and the volume finally brought to 500 mL with deionized water. These suspensions were stored at 70 °C for 16 days and afterwards washed, air-dried, and sealed in glass vials.

A second series of As<sup>5+</sup> doped hematite was synthesized by transforming ferrihydrite, synthesized after a modified version of [12]. A mass of 5.05 g Fe(NO<sub>3</sub>)<sub>3</sub>·9H<sub>2</sub>O was dissolved in 100 mL deionized water and transformed into ferrihydrite by a rapid addition 22.5 mL 5 M KOH solution under constant stirring. This slurry was carefully washed to diminish the potassium and nitrate content, adjusted to pH 4 by adding 65 % HNO<sub>3</sub>, and doped with 1.44 g arsenic pentoxide (As<sub>2</sub>O<sub>5</sub>) dissolved in 25 mL deionized water. Upon addition of the As<sub>2</sub>O<sub>5</sub> solution, the pH of the slurry dropped and was re-adjusted again to pH 4 by 5 M KOH solution. This sample, with a molar As : Fe ratio of 1 was allowed to transform into hematite in a pressure bomb for seven days at 200 °C. The need for such high temperatures arose from the slow transformation speed of ferrihydrite at increased As<sup>5+</sup> concentrations [9]. The product was labeled as the sample HEM<sub>1to1</sub>. In order to remove as much As<sup>5+</sup> as possible from the surface of the HEM<sub>1to1</sub> sample, but also to ensure that no traces of ferrihydrite are left, the sample was washed for 2 hours with

250 mL of a 15 % HCl solution at room temperature. After the HCl treatment, the product was washed with deionized water, air-dried, and sealed in a glass vial.

Pure angelellite was synthesized after Wright et al. (2000) [13], but the temperature of 700°C was maintained for 36 h instead of 12 h, since the reactants were still present after 12 h.

Elemental composition of the samples (Fe, As) was determined by inductively-coupled plasma optical emission spectrometry (ICP-OES) with a Variant 725 ICP-OES with a charge-couple device (CCD) detector. For the measurements, about 50 mg of each sample was digested in 5 mL 10 % hydrochloric acid at 100 °C, filled to a defined volume of 10 mL, and stored in corrosion-resistant sample tubes.

Reference compounds used for the X-ray absorption work were angelellite ( $\text{Fe}_4(\text{AsO}_4)_2\text{O}_3$ ), scorodite ( $\text{FeAsO}_4 \cdot 2\text{H}_2\text{O}$ ), kaňkite ( $\text{FeAsO}_4 \cdot 3.5\text{H}_2\text{O}$ ), and parasymphesite ( $\text{Fe}_3(\text{AsO}_4)_2 \cdot 8\text{H}_2\text{O}$ ). Scorodite (from the locality Schwarzenberg, Saxony, Germany) and parasymphesite (from the locality Saubach, Saxony, Germany) were natural samples taken from the Mineralogical Collection Jena, and the specimen of kaňkite came from a natural sample kindly provided by J. Plášil.

Powder X-ray diffraction (XRD) patterns of all samples and reference compounds were collected with a Bruker D8 AXS Advance diffractometer at Cu K $\alpha$  radiation ( $\lambda = 1.54058 \text{ \AA}$ ). The patterns were collected at room temperature between 5-130 °2 $\theta$  with a step size of 0.02 °2 $\theta$  and a dwell time of 10 seconds. In order to reduce the noise from Fe-fluorescence, the energy window of the detector was set to 0.18-0.25 V. All samples were refined by a full-profile fit with the program TOPAS<sup>®</sup>. For the full-profile fit a Pearson VII function was used and a fitting range between 15-130 °2 $\theta$  was chosen. For each fit, the statistical measures of the deviation of the fit

from the obtained data are given including the residuals for the weighted profile ( $R_{wp}$ ) and the goodness-of-fit (GOF). Crystallite size and stain were determined by a Gaussian function implemented in TOPAS<sup>®</sup>.

Scanning electron microscopy (SEM) was employed for microphotographs and morphology determination, using a Carl Zeiss ULTRA PLUS FE-SEM with an Inlens SE-detector, operating at 20 kV and a JEOL JEM-2000 FX microscope, operating at 160 kV, with an ASID 20 scanning unit.

In order to obtain information about the distribution of  $As^{5+}$  within the individual hematite crystals, crystals of the sample HEM<sub>1to1</sub> were embedded in agar, which was saturated with water for five days. Subsequently, the water was replaced by methanol, methanol by propylene oxide and propylene oxide finally by Spurr resin after Tessier (1984) [14]. Sections of about 70-90 nm in thickness were cut parallel to the flattening direction of the particles (available in the Supplemental Material Figure 1S), using a diamond knife and Reichert Ultracut microtome. Energy-dispersive point chemical analyses of the sections and electron diffraction patterns were acquired with a Philips 420 STEM microscope, operating at 120 kV, with a Link AN 10000 energy-dispersive analyzer with a windowless Si-Li detector.

Extended X-ray absorption fine-structure (EXAFS) spectra of the sample HEM<sub>1to1</sub> and the reference compounds angelellite, scorodite, kaňkite, and parasymplectite were collected at the As *K* edge at the SUL-X beamline of the Angströmquelle Karlsruhe (ANKA, Karlsruhe, Germany) using a silicon (111) crystal pair with a fixed beam exit as monochromator. A portion of each samples and reference substances, calculated by the program XAFSmass [15], was mixed with cellulose powder, homogenized, and pressed to a pellet. The spectra were collected with a step width of 5 eV in the region -150 to -50 eV, 1 eV in the region -50 to -20 eV

below the edge, 0.3 eV in the region -20 to +50 eV relative to the edge, and  $0.05k$  up to  $15k$  (860 eV) above the absorption edge. Depending on the As and Fe concentration, the spectra were either measured in transmission or fluorescence mode. A gold foil was mounted between ionization chamber 2 and 3 and the Au L3 edge was recorded parallel to each sample spectrum for energy calibration. Five spectra were measured for each sample and two spectra for each reference compound. All EXAFS spectra were processed and fit by the Athena and Artemis software package [16]. For the fitting, we used paths generated from different models including angelellite [17], scorodite [18], parasymphesite [19], and a combined model of hematite with an included angelellite-like cluster (see Figure 1 and Figure 2S). The specifications of the cluster model are given in section “*Structures of interest*”.

In order to reduce the number of atoms of the angelellite-like cluster model in the FEFF calculation, three spheres with a radius of 5 Å around three adjacent  $\text{As}^{5+}$  atoms were chosen for the calculation of the paths (see Figure 3S). Parameters for these paths were calculated by FEFF6 [20] embedded in the Artemis software package. For the fit, the statistical measures of the deviation of the fit from the obtained data are given, including the number of variables allowed to float in the fit ( $N_{\text{var}}$ ), number of independent data points ( $N_{\text{idp}}$ ), and the  $R$  factor. The  $N_{\text{idp}}$  is equal to  $2\Delta kR/\pi$  where  $k$  and  $R$  are the fitting ranges. The  $R$  factor is defined as

$$R = \frac{\sum [\chi_i^{\text{data}} - \chi_i^{\text{model}}(\mathbf{x})]^2}{\sum [\chi_i^{\text{data}}]^2}$$

where  $\chi$  is the magnitude of the EXAFS oscillations and  $\mathbf{x}$  is the set of variables to be refined.

The EXAFS spectra of the reference compounds were fit with the respective structures. These spectra were used to identify problems that could be encountered when fitting a model to the structurally unknown sample.

## STRUCTURES OF INTEREST

**Hematite**,  $\alpha\text{-Fe}_2^{3+}\text{O}_3$ , is built by a hexagonally close-packed (hcp) array of oxygen atoms in which the  $\text{Fe}^{3+}$  cations occupy two thirds of the octahedral interstices. The tetrahedral interstices remain vacant, and the tetrahedra centered on those interstices share two edges and two faces with the adjacent  $\text{Fe}^{3+}\text{O}_6$ -octahedra [21]. The  $\text{Fe}^{3+}\text{O}_6$ -octahedra share three of their edges with neighboring  $\text{Fe}^{3+}\text{O}_6$ -octahedra within the (0001) plane, and one face with an  $\text{Fe}^{3+}\text{O}_6$ -octahedron of an adjacent plane [22].

**Angelellite**,  $\text{Fe}_4^{3+}(\text{AsO}_4)_2\text{O}_3$ , is a triclinic phase, built by a cubic array of oxygen atoms, just like hematite. The ccp array of angelellite holds  $\text{Fe}^{3+}$  in the octahedral interstices, but unlike in hematite, the tetrahedral interstices are occupied by  $\text{As}^{5+}$  [17]. The  $\text{Fe}^{3+}\text{O}_6$ -octahedra condense into chains parallel to the *c* axis, in which each octahedron shares edges with three neighboring octahedra. All ligands of the arsenate tetrahedron bridge  $\text{As}^{5+}$  and  $\text{Fe}^{3+}$ .

**Scorodite**,  $\text{Fe}^{3+}\text{AsO}_4\cdot 2\text{H}_2\text{O}$ , is an orthorhombic iron arsenate. The  $\text{Fe}^{3+}\text{O}_6$ -octahedra share vertices only with arsenate tetrahedra, i.e., no ligands bridge two  $\text{Fe}^{3+}$  cations. Full polymerization of the structure is precluded by the presence of  $\text{H}_2\text{O}$  as ligands of  $\text{Fe}^{3+}$  [18]. The crystal structure of scorodite is a relatively dense framework of  $\text{FeO}_4(\text{OH}_2)_2$  octahedra and  $\text{AsO}_4$ -tetrahedra where the polyhedra attach to each exclusively by corner sharing.

**Kaňkite**,  $\text{Fe}^{3+}\text{AsO}_4 \cdot 3.5\text{H}_2\text{O}$ , is a monoclinic iron arsenate with a structure that consists of corrugated sheets. Within the sheets, the polyhedra share only edges; the sheets are connected by a network of hydrogen bonds (unpublished data).

**Parasymplesite**,  $\text{Fe}_3^{2+}(\text{AsO}_4)_2 \cdot 8\text{H}_2\text{O}$ , unlike the previous phases, is an arsenate of ferrous iron, with monoclinic symmetry. Each oxygen of the  $\text{As}^{5+}\text{O}_4$ -tetrahedron has one bond to an adjacent  $\text{Fe}^{2+}$ -atom, resulting in four corner-sharing  $\text{Fe}^{2+}\text{O}_6$ -octahedra on one  $\text{As}^{5+}\text{O}_4$ -tetrahedron. The  $\text{Fe}^{2+}\text{O}_6$ -octahedra are either connected to  $\text{As}^{5+}\text{O}_4$ -tetrahedra only, in which case four oxygen are protonated, or edge-sharing with an adjacent  $\text{Fe}^{2+}\text{O}_6$ -octahedra where they possess two protonated oxygen [19].

**Crystallographic relationships between the phases considered here.** Of the phases described above, hematite and angelellite are closely related. They are known to integrow epitaxially [23,24] by  $(0001)_{\text{hematite}}$  and  $(210)_{\text{angelellite}}$  [17], where the  $(210)$  plane of angelellite refers to the unit-cell orientation chosen by [17]. The possibility of epitaxial intergrowth led us to the construction of a model, where a cluster of angelellite is included in a hematite host.

The two oxygen layers and all  $\text{Fe}^{3+}$  and  $\text{As}^{5+}$  atoms between them were incorporated, parallel to the  $(0001)$  plane of hematite, into the hematite structure. For steric reasons,  $\text{Fe}^{3+}$  atoms of the hematite structure, closer than 3.10 Å to a nearby (inserted)  $\text{As}^{5+}$  atom were excluded (see Figure 1 and File 1S in the Supplementary Material).

All structures of interest are shown in Figure 4S in the Supplementary Material.

## RESULTS

### *Characterization of the ferrihydrite transformation products*

The  $\text{As}^{5+}$  concentrations in the samples, the refined lattice parameters, strain, and crystallite size of all full-profile fits are given in Table 1. Immediately obvious is the positive correlation between the lattice parameter  $c$  of hematite and  $\text{As}^{5+}$  concentration in the samples. The lattice parameter  $c$  of hematite increases from 13.7690(7) Å in the absence of  $\text{As}^{5+}$  to 13.7943(5) Å at a molar As : Fe ratio of 1. The unit cell parameter  $a$  does not show any correlation to the  $\text{As}^{5+}$  concentration within its uncertainties. Both observations comply with those reported for hematite grown in the presence of  $\text{P}^{5+}$  [10].

Although sample  $\text{HEM}_{2.25}$  was formed at lower  $\text{As}^{5+}$  concentrations than the sample  $\text{HEM}_{1\text{to}1}$ , the measured  $\text{As}^{5+}$  concentration is higher in the sample  $\text{HEM}_{2.25}$ . It should be considered that both samples were formed at different temperatures over different times, and that sample  $\text{HEM}_{1\text{to}1}$  was treated with HCl to remove any remaining ferrihydrite and  $\text{As}^{5+}$  bound to the surface of hematite.

Grain size and morphology of the hematite samples depend on the synthesis conditions. Hematite crystals formed in the absence of  $\text{As}^{5+}$  at pH 4 and 70 °C are ~30-150 nm large rhombohedra (Figure 2a) and the same morphology was observed for hematite formed at the same temperature and starting  $\text{As}^{5+}$  molarities of 0.23-2.25 mM (Figure 2b). Hematite grown at a molar As : Fe ratio of 1, pH 4, and 200 °C (the sample  $\text{HEM}_{1\text{to}1}$ ) has a form of spheroidal platelets, with particle sizes of 300-2000 nm (Figure 2c). Angelellite forms flattened spheroidal particles with sizes of 100-2000 nm, similar to those of the sample  $\text{HEM}_{1\text{to}1}$  (Figure 2d).



---

### *Characterization of the reference compounds*

The crystal structures of angelellite, scorodite, and parasymplectite were also refined by a full-profile fit using TOPAS<sup>®</sup> with the starting model from [17,18,19], respectively. A minor impurity within the angelellite sample was tentatively identified as FeAsO<sub>4</sub>. The formation of this iron arsenate during the angelellite synthesis, described by [13], yields a fraction of 9.5(7) wt%.

### *Chemical analysis of the hematite crystals by TEM-EDX*

The chemical analysis by ICP-OES is a bulk analysis, and the As<sup>5+</sup> detected may reside on the surface of the hematite particles, in the crystal structure of hematite, or in an impurity phase. To locate As<sup>5+</sup> within our samples, the sample HEM<sub>1to1</sub>, treated with HCl to remove adsorbed As<sup>5+</sup> and residues of untransformed ferrihydrite, was embedded in resin and cut into electron-transparent slices. The chemical composition of the sliced crystals was measured in profiles across the crystals, hence testing the hypothesis that As<sup>5+</sup> is found inside the crystals. Nine crystals were measured at 69 points and the measured Fe concentration was 68.0±0.7 wt.% (mean value) and As concentration of 1.9±0.8 wt.% (mean value). With the exception of carbon and oxygen, both present in the resin, no other elements could be detected by EDX. Since the morphology of the hematite, grown at a molar As : Fe ratio of 1, and angelellite is very similar (see Figure 3), the crystals measured by EDX were additionally investigated by selected-area electron diffraction (SAED) (see Figure 3). In all cases, SAED confirmed that the analyzed crystals were hematite and not an angelellite impurity.

---

*XANES and EXAFS at the As K edge*

Arsenic in sample HEM<sub>1to1</sub> and all reference materials (structures of interest) occurs exclusively as As<sup>5+</sup> (see Figure 5S). EXAFS measurements were performed to obtain information about the local environment of As<sup>5+</sup> in the As-doped hematite. The FT EXAFS spectra of the sample HEM<sub>1to1</sub>, angelellite, scorodite, kaňkite, and parasymphesite are compared in Figure 4. The spectra of the sample HEM<sub>1to1</sub> and all reference compounds share many similar features. The EXAFS spectrum of sample HEM<sub>1to1</sub> was therefore fitted with the calculated paths from angelellite [17], scorodite [18], kaňkite (unpublished data), parasymphesite [19], and a combined model of hematite with an included angelellite-like cluster (see Figure 1). As expected for As<sup>5+</sup>, the fitting shows that the absorber atom (As) is surrounded by four oxygen atoms with a distance of 1.692 Å, slightly longer compared to the As-O distance in angelellite (1.666-1.691 Å), scorodite (1.670-1.684 Å) and, parasymphesite (1.596-1.695 Å), taken from the crystallographic information files. Paths for multiple-scattering (MS) As-O-O-As were also included in the fitting procedure. The  $\Delta r$  of the multiple scattering path ( $\Delta r_{\text{As-O-O-As}}$ ) was assumed to be twice the  $\Delta r_{\text{As-O-As}}$  value, which was refined for the first shell. The variable  $\sigma^2_{\text{As-O-O-As}}$  of the MS path was also assumed to be twice the value of  $\sigma^2_{\text{As-O-As}}$  of the first shell.

In the first set of attempt to reduce the data, we used the structural model of our reference compounds and tested these models against the measured data for the sample HEM<sub>1to1</sub>. The angelellite model performed well for all three shells of our dataset. The second shell, however, displays minor differences at 2.4 Å (all distances in this paragraph uncorrected for the phase shift), leading to an increased *R* factor (see Figure 6S). For scorodite, the first and third shell can be fitted within acceptable parameters, the second shell, however, displays significant differences at 2.4 Å and

shows no further similarities with our sample (Figure 6S). A parasymphesite model could fit the first and second shell, however, the similarities between the parasymphesite structure and our data ended after 3.3 Å. For the kaňkite model, the first shell could be fitted well, like for all the other arsenates, but already the second shell displayed considerable differences to our sample HEM<sub>1to1</sub>. In summary, the structural models from the reference compounds fit well the first shell, not all of them can fit the second shell, and only angelellite can fit the third shell.

The best fit was accomplished with the angelellite-like cluster model, explained in detail in the section “*Structures of interest*”. For the fit, the 7 closest Fe and 28 closest O atoms, including the four nearest oxygen neighbors of As<sup>5+</sup>, of the angelellite-like cluster model were used. In order to reduce the number of atoms for the FEFF calculation, a sphere of atoms with a radius of 5 Å around three adjacent As<sup>5+</sup> atoms (Figure 1) were included (see Table 1 and Figure 5).

Multiple scattering (MS) paths involving atoms of the first shell were included, MS paths involving atoms of the second and third shell were excluded. The third shell was split into two groups of scattering paths variations from the model ( $\Delta r$ ) with a single Debye-Waller factor ( $\sigma^2$ ). During the fit, all parameters including CN,  $\Delta r$ , and  $\sigma^2$  were consecutively refined.

For a comparison between the fits of the most likely models, angelellite, scorodite, and the angelellite-like cluster see Tables 1S-3S in the supplementary materials. No tables were included for kaňkite parasymphesite, since the parameters of both models drifted to unreasonable values.

## DISCUSSION

### *Relevance of hematite for As<sup>5+</sup> immobilization*

Ferrihydrite with its large surface area of 200-300 m<sup>2</sup>/g is known as a potent adsorber of arsenate, much more efficient than hematite with a typical surface area of < 30 m<sup>2</sup>/g [22]. These values are in excellent agreement with the surface area values for our ferrihydrite and hematite samples (hematite produced at 70 °C) [9]. The surface area of the disc-shaped hematite particles in the sample HEM<sub>1to1</sub> was calculated from the SEM images to be around 1 m<sup>2</sup>/g. Therefore, if the surface area is taken as the most important criterion for the capacity to bind As<sup>5+</sup>, hematite is considered to be of inferior importance for the immobilization of As<sup>5+</sup> in the environment, when other, high-surface area phases like ferrihydrite are present. This line of thinking is valid but does not take the possibility of structurally bound As<sup>5+</sup> into account. Our work shows that even hematite with large particle size (very low surface area of 1 m<sup>2</sup>/g) can hold a considerable amount of As<sup>5+</sup> (1.8 wt%) if this hematite formed by transformation of As<sup>5+</sup>-doped ferrihydrite. These high As<sup>5+</sup> values exceed by far the amount that can be attached to the surface, hence indicating a second binding mechanism, other than adsorption. We assume that most of the As<sup>5+</sup> is incorporated within the hematite crystals and only a minor fraction of As<sup>5+</sup> is adsorbed on the surface of hematite.

### *As<sup>5+</sup> in the hematite structure*

The incorporation of As<sup>5+</sup> into the tetrahedral interstices of the hematite structure, analogous to that described for P<sup>5+</sup> by [10], involves several difficulties. Although P<sup>5+</sup> is often referred as a chemical analogue for As<sup>5+</sup>, the small ionic radius (~ 0.17 Å) of P<sup>5+</sup> with tetrahedral coordination [25] leads to considerably shorter P-O

bonds, which, for natural samples, are typically at 1.44-1.63 Å [26]. In comparison, tetrahedrally coordinated  $\text{As}^{5+}$  with an ionic radius of 0.335 Å [25] prefers As-O distances of 1.60-1.70 Å [17,18,19,27]. Anyway, a hypothetical cation in the center of hematite's tetrahedral interstices would have a distance of about 1.77 Å to the four surrounding O atoms, too long for both,  $\text{P}^{5+}$  and  $\text{As}^{5+}$ .

Furthermore, within the densely packed hematite structure,  $\text{Fe}^{3+}$  occupies two thirds of the octahedral interstices, which excludes the possibility of insertion of a tetrahedral high-charge cation if the  $\text{Fe}^{3+}$  array is to remain intact. The mere incorporation of an  $\text{As}^{5+}$  atom into an empty tetrahedral interstitial site would inevitably lead to too short  $\text{Fe}^{3+}$ - $\text{As}^{5+}$  distances, since the coordination polyhedra ( $\text{Fe}^{3+}$  octahedra and  $\text{As}^{5+}$  tetrahedra) would share edges or faces. The distance between the  $\text{As}^{5+}$  and  $\text{Fe}^{3+}$  neighbors would be about 1.65-1.95 Å for the face-sharing and 2.68-2.69 Å for the edge-sharing polyhedra. Such short distances between highly charged cations are unrealistic because they would lead to strong repulsive forces and destabilize the structure.

In order to solve this problem, for each  $\text{As}^{5+}$ , at least four  $\text{Fe}^{3+}$  atoms would have to be removed from the hematite structure, which are in a face- or edge-sharing contact with the  $\text{As}^{5+}$  tetrahedron. The removal of four  $\text{Fe}^{3+}$  leads to an excess of 12 negative charges, from which the newly incorporated  $\text{As}^{5+}$  can balance only five. By examining the structural hematite model of Blake et al. (1966) it must be noticed that no oxygen atoms are lost or gained upon removal of 4  $\text{Fe}^{3+}$  cations and insertion of  $\text{As}^{5+}$ . Hence, the remaining 7 negative charges must be balanced by another mechanism. An option entertained by [10] is protonation. When examining the  $\text{As}^{5+}$ -centered cluster, however, we were not able to locate more than two oxygen atoms which could be protonated, based on simple arguments of bond valence.

*Intergrowth instead of forced incorporation*

Epitaxial intergrowth of two phases with different compositions, out of which one contains the element of interest, is another way of element incorporation. The element of interest (here  $\text{As}^{5+}$ ) is therefore not directly incorporated in the host phase (in our case hematite) but is piggybacking in a carrier phase (angelellite), which possesses  $\text{As}^{5+}$  in its structure. In this case, such carrier phase is angelellite. The host, hematite, does not necessarily possess the ability to incorporate the  $\text{As}^{5+}$ , but is required to epitaxially intergrow with the carrier phase angelellite. Hematite and angelellite can intergrow epitaxially, because the oxygen atoms of the  $(0001)_{\text{hematite}}$  plane of hematite can be aligned to the oxygen atoms of the  $(210)_{\text{angelellite}}$  plane, acting as an interface between both structures (see Figure 1).

The oxygen nets of the  $(0001)_{\text{hematite}}$  plane and the  $(210)_{\text{angelellite}}$  plane show small variations in their distance from one layer to the other. In hematite the distance between the oxygen nets of the  $(0001)$  plane is 2.295 Å, whereas in angelellite the two oxygen layers of the  $(210)$  plane have a distance of 2.333 Å. Assuming an angelellite-like layer would intergrow with hematite, the hematite structure would expand parallel to the  $c$  direction and therefore the unit-cell parameter  $c$  of hematite would increase, depending on the number of angelellite-like layers intergrown. This phenomenon was observed in our study by a positive correlation between an increase of the lattice parameter  $c$  in hematite and its  $\text{As}^{5+}$  concentration (Table 1), but it was also observed by similar studies with  $\text{P}^{5+}$  [10].

The epitaxial intergrowth of hematite and angelellite within such localized dimension can be considered to have only a minor influence on the long-range order within the hematite crystal. The short-range order around the  $\text{As}^{5+}$  atom, however, changes completely. As shown in our EXAFS results, the dataset for  $\text{HEM}_{1\text{to}1}$  is similar to the

other iron arsenates like angelellite, scorodite, and parasymphesite. Because all syntheses were carried out in oxidizing conditions, the formation of parasymphesite within our sample can be excluded, since parasymphesite is a  $\text{Fe}^{2+}$  arsenate.

Scorodite could form under the conditions of our syntheses, but the XRD analysis shows no sign of scorodite formation and TEM-EDX proved that a considerable amount of  $\text{As}^{5+}$  occurs within the hematite crystals. Additionally, if  $\text{As}^{5+}$  would occur in nanometer sized scorodite crystals, the EXAFS spectrum of our sample would have to fit to the paths, calculated from the crystal structure of scorodite. This, however, is not the case. Only the first and the third shell can be fitted to the spectrum of our sample, whereas the second shell exhibits considerable differences and cannot be fitted by scorodite.

The most suitable candidate for a single-phase fitting is angelellite. Crystals in the low nanometer range could intergrow with hematite and hold the  $\text{As}^{5+}$ , which we analyze. Though, crystals of angelellite within the hematite matrix, accidentally measured by TEM-EDX can be excluded, since the electron diffraction pattern of the measured crystals can be indexed exclusively by hematite. Larger crystals as a separated phase can also be excluded by XRD, where no other phase than hematite was observed (Figure 7S). However, the size of the angelellite-like clusters may vary and cannot accurately be determined by EXAFS, which allows a good fit for small angelellite-like clusters and an acceptable fit for angelellite as a single phase.

Our proposed model of angelellite-like clusters intergrown with hematite can explain satisfactorily all observations. Like shown in Figure 1, a cluster of angelellite can intergrow with hematite almost perfectly, leading to a slight increase in the unit cell parameter  $c$  of hematite as observed by XRD. Chemical analyses of the cross-sections of the hematite crystals proved that  $\text{As}^{5+}$  is not exclusively bound by the

surface of hematite or another precipitated As compound; arsenic is present inside the crystals. The EXAFS spectrum of the hematite sample HEM<sub>1to1</sub> can be fitted to the model of the angelellite-like clusters, where the first and second shell is almost completely covered by atoms belonging to the original angelellite model, whereas the third shell can be fitted with the more distant Fe and O atoms of the hematite based structure (Table 1).

The formation of angelellite-like local clusters during the transformation of ferrihydrite to hematite offers a new immobilization mechanism for As<sup>5+</sup> by iron oxides. Incorporated As<sup>5+</sup> will stay within the hematite crystals as long the hematite itself remains stable. In this study, we propose that the preferential formation of hematite (instead of goethite) from As<sup>5+</sup>-doped ferrihydrite is templated by angelellite-like clusters. Earlier assumptions [28] such as formation of hematite simply by enhanced aggregation of ferrihydrite particles can be revised in the light of our findings.

## ASSOCIATED CONTENT

Supporting figures and tables can be found in the supplementary material. Figure 1S: Sample preparation for SEM and TEM, Figure 2S: Colored image of an angelellite cluster intergrown with hematite, Figure 3S: Colored image of the angelellite-like cluster used for fitting, Figure 4S: Colored image of the Structures of Interest, Figure 5S: XANES spectra of sample HEM<sub>1to1</sub> and corresponding reference substances, Figure 6S: Fits of angelellite and scorodite to sample HEM<sub>1to1</sub>, Table 1S: Fitting results for angelellite to sample HEM<sub>1to1</sub>, Table 2S: Fitting results for scorodite to sample HEM<sub>1to1</sub>, Table 3S: Fitting results of the angelellite-like local cluster to



sample HEM<sub>1to1</sub>, File 1S: Crystallographic information file for the angelellite-like cluster used for EXAFS fitting.

## ACKNOWLEDGEMENTS

We want to thank Birgit Kreher-Hartmann for the parasymplectite and scorodite specimens supplied by the Mineralogische Sammlung Jena and Jakub Plášil (Institute of Physics, Czech Academy of Sciences in Prague) for the kaňkite sample. We thank Dirk Merten and Ines Kamp for their support during the ICP-OES analyses. We are thankful to the two anonymous reviewers for their constructive suggestions and criticism. We are grateful to the Karlsruhe Institute of Technology for the beam time at the Angströmquelle Karlsruhe (ANKA). Thanks go to the Friedrich-Schiller-University Jena, Germany and the Comenius University Bratislava, Slovakia, where most of the experiments were conducted. This research was funded by the DFG Research Training Group GRK 1257/1 within the Jena School of Microbial Communications (JSMC).

## LITERATURE CITED

- [1] Henke, K. *Arsenic – Environmental Chemistry, Health Threats and Waste Treatment*. John Wiley & sons Ltd. Chichester, UK, **2009**.
- [2] Waychunas, G.A.; Rea, B.A.; Fuller, C.C.; Davis, J.A. Surface chemistry of ferrihydrite: Part 1. EXAFS studies of the geometry of coprecipitated and adsorbed arsenate. *Geochim. Cosmochim. Acta* **1993**, 57, 2251-2269.
- [3] Waychunas, G.A.; Davis, J.A.; Fuller, C.C. Geometry of sorbed arsenate on ferrihydrite and crystalline FeOOH: Re-evaluation of EXAFS results and topological factors in predicting sorbate geometry, and evidence for monodentate complexes. *Geochim. Cosmochim. Acta* **1995**, 59, 3655-3661.

- 
- [4] Manceau, A. The mechanism of anion adsorption on iron oxides: evidence for the bonding of arsenate tetrahedral on free  $\text{Fe}(\text{O},\text{OH})_6$  edges. *Geochim. Cosmochim. Acta* **1995**, 59, 3647-3653.
- [5] Michel, M.F.; Ehm, L.; Antao, S.M.; Lee, P.L.; Chupas, P.J.; Liu, G.; Strongin, D.; Schoonen, M.A.A.; Phillips, B.L.; Parise, J.B. The structure of ferrihydrite, a nanocrystalline material. *Science* **2007**, 316, 5832, 1726-1729.
- [6] Loan, M.; Parkinson, G.M.; Richmond, W.R. The effect of zinc sulfide on phase transformations of ferrihydrite. *Am. Mineral.* **2005**, 90, 258-261.
- [7] Cudennec, Y.; Lecerf, A. The transformation of ferrihydrite into goethite or hematite, revisited. *J. Solid State Chem.* **2006**, 179, 716-722.
- [8] Paige, C.R.; Snodgrass, W.J.; Nicholson, R.V.; Scharer, J.M. The crystallization of arsenate contaminated iron hydroxide solids at high pH. *Water Environ. Res.* **1996**, 68, 6, 981-987.
- [9] Bolanz, R.M.; Bläss, U.; Ackermann, A.; Ciobotă, V.; Rösch, P.; Tarcea, N.; Popp, J.; Majzlan, J. The effect of antimonate, arsenate and phosphate on the transformation of ferrihydrite to goethite, hematite, feroxyhyte, and tripuhyte. *Clay. Clay. Miner.* **2013**, 61, 11-25.
- [10] Gálvez, N.; Barrón, V.; Torrent, J. Preparation and properties of hematite with structural phosphorus. *Clay. Clay. Miner.* **1999**, 47, 375-385.
- [11] Violante, A.; Gaudio, S.D.; Pigna, M.; Ricciardella, M.; Banerjee, D. Coprecipitation of arsenate with metal oxides. 2. Nature, mineralogy, and reactivity of iron(III) precipitates. *Environ. Sci. Technol.* **2007**, 41, 8275-8280.
- [12] Schwertmann, U.; Cornell, R.M. *Iron oxides in the laboratory: Preparation and Characterization, 2nd edition*. Wiley-VCH Verlag, Weinheim **2000**.
- [13] Wright, J.P.; McLaughlin, A.C.; Atfield, J.P. Partial frustration of magnetic order in synthetic angelellite,  $\text{Fe}_4\text{As}_2\text{O}_{11}$ . *J. Chem. Soc., Dalton Trans.* **2000**, 3663-3668.
- [14] Tessier, D. *Étude expérimentale de l'organisation des matériaux argileux*. Ph.D. Dissertation, Université Paris VII, France, **1984**.
- [15] Klementiev K.V. XAFS<sub>mass</sub>, April 2012, website: [www.cells.es/Beamlines/CLAESS/software/xafsmass.html](http://www.cells.es/Beamlines/CLAESS/software/xafsmass.html)
- [16] Ravel, B.; Newville, M. ATHENA, ARTEMIS, HEPHAESTUS: data analysis for X-ray absorption spectroscopy using IFEFFIT. *J. Synchrotron. Radiat.* **2005**; 12, 537-541.
- [17] Moore, P.B.; Araki, T. Angelellite,  $\text{Fe}_4^{3+}\text{O}_3(\text{As}^{5+}\text{O}_4)_2$ : a novel cubic close-packed oxide structure. *N. Jb. Miner. Abh.* **1978**, 132, 91-100.
- [18] Kitahama, K.; Kiriya, R.; Baba, Y. Refinement of the crystal structure of scorodite. *Acta Cryst.* **1975**, B31, 322-324.
- [19] Mori, H.; Ito, T. The structure of vivianite and symplectite. *Acta Cryst.* **1950**, 3, 1-6.
- [20] de Leon, M.J.; Rehr, J.J.; Zabinsky, S.I.; Albers, R.C. Ab initio curved-wave X-ray-absorption fine structure. *Phys. Rev.* **1991**, B44, 4146-4156.
- [21] Blake, R.L.; Hessevic, R.E.; Zoltai, T.; Finger, L.W. Refinement of hematite structure. *Am. Mineral.* **1966**, 51, 123-129.

- [22] Cornell, R.M.; Schwertmann, U. *The iron oxides, properties, reactions, occurrences, and uses*. Wiley-VCH Verlag, Weinheim **2003**.
- [23] Rahmdor, P.; Ahlfeld, F.; Berndt, F. Angelellit, einnatürliches triklines Eisen-Arsenat,  $2\text{Fe}_2\text{O}_3 \cdot \text{As}_2\text{O}_5$ . *N. Jb. Miner. Monat.* **1959**, 132, 91-100.
- [24] Weber, K. Crystallographic study of angelellite,  $2\text{Fe}_2\text{O}_3 \cdot \text{As}_2\text{O}_5$ . *N. Jb. Miner. Monat.* **1959**, 152-158.
- [25] Shannon, R.D. Revised effective ionic radii and systematic studies of interatomic distances in halides and chalcogenides. *Acta Cryst.*, **1976**, A32, 751-767.
- [26] Huminicki, D.M.C.; Hawthorne, F.C. The crystal chemistry of the phosphate minerals. *Rev. Mineral. Geochem.* **2002**, 48, 123-253.
- [27] Majzlan, J.; Lazic, B.; Armbruster, T.; Johnson, M.B.; White, M.A.; Fisher, R.A.; Plašil, J.; Loun, J. Crystal structure, thermodynamic properties, and petrogenesis of bukovskýite,  $\text{Fe}_2(\text{AsO}_4)(\text{SO}_4)(\text{OH}) \cdot 9\text{H}_2\text{O}$ . *J. Miner. Petrol. Sci.* **2012**, 107, 133-148.
- [28] Paige, C.R., Snodgrass, W.J., Nicholson, R.V., and Scharer, J.M. The crystallization of arsenate-contaminated iron hydroxide solids at high pH. *Water Environment Research*, **1996**, 68, 6, 981-987.

## FIGURE CAPTIONS

Figure 1: The structure of hematite with an included angelellite-like cluster. The (210) plane of angelellite runs parallel to the (0001) plane of hematite.  $\text{Fe}^{3+}$  atoms of the hematite structure closer than 3.1 Å to the next  $\text{As}^{5+}$  atom of angelellite were excluded. A colored version of this figure is available in the supplementary material (Figure 2S).

Figure 2: SEM microphotographs of the ferrihydrite transformation products. (a) rhombohedral crystals of hematite grown at 70°C at pH 4 in the absence of  $\text{As}^{5+}$  in aqueous solution. (b) rhombohedral hematite crystals grown at 70 °C at pH 4 in 0.23 mM  $\text{As}^{5+}$  solution. (c) disc-shaped hematite crystals grown at 200 °C at pH 4 at an molar As : Fe ratio of 1. (d) disc-shaped crystals of angelellite grown at 700 °C via a solid-state synthesis.

Figure 3: Bright field TEM image (a) and corresponding selected area electron diffraction pattern (b) of a sliced hematite crystal. The crystal is oriented near the  $[\bar{2} 205]$  zone axis parallel to the primary electron beam.

Figure 4: Fourier transforms of the As K-edge spectra taken from sample HEM<sub>1to1</sub> (a), angelellite (b), scorodite (c), kaňkite (d), and parasymphesite (e). The grey dashed lines indicate prominent features of the second and third shell of sample HEM<sub>1to1</sub>.

Figure 5: (a) Normalized,  $k^3$ -weighted As K-edge EXAFS spectrum of sample HEM<sub>1to1</sub>. (b) real part of the Fourier transform of the As K-edge EXAFS spectrum of sample HEM<sub>1to1</sub>. (c) magnitude of the Fourier transform of the As K-edge EXAFS spectrum of sample HEM<sub>1to1</sub>. The black dots indicate the measured data, whereas the solid grey lines show the achieved fit.

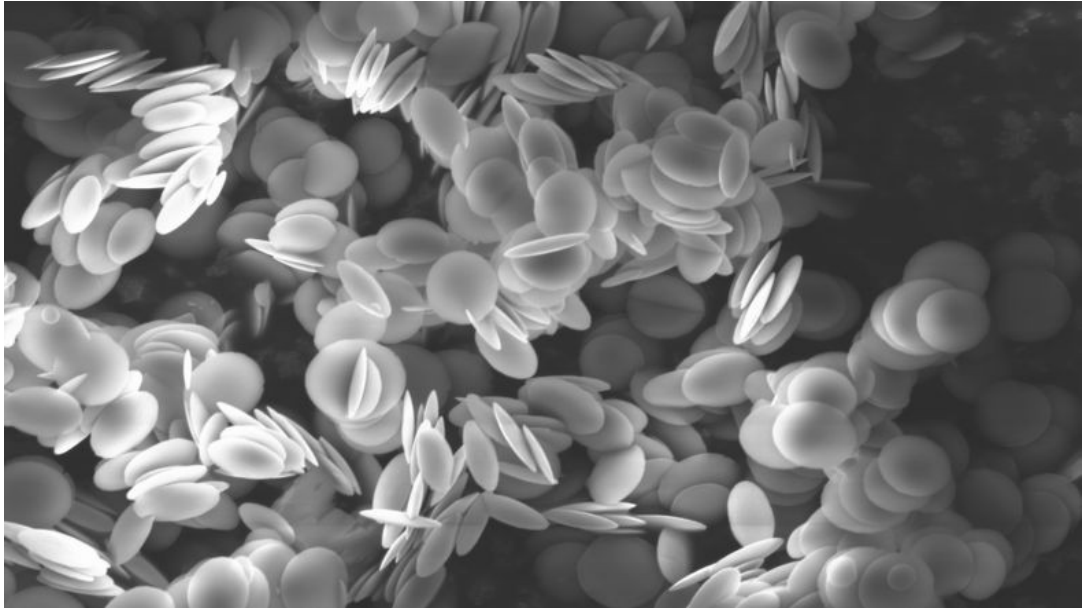
Table 1: Lattice parameters of the ferrihydrite transformation products grown in the absence and presence of As<sup>5+</sup>. The numbers in parentheses are the standard deviations of the measurements on the last decimal digit reported.

sample	As (wt%)	a(Å)	c(Å)	strain(G)	cryst. size (nm)	R <sub>wp</sub>	GOF
HEM0.00	0.00(0)	5.0372(0)	13.7690(7)	0.02(7)	145 ± 2	3.749	1.70
HEM0.23	0.31(7)	5.0387(4)	13.7787(0)	0.10(1)	183 ± 2	3.787	1.64
HEM0.75	0.90(1)	5.0388(6)	13.7846(7)	0.15(0)	160 ± 3	4.030	1.80
HEM2.25	2.64(1)	5.0389(0)	13.7853(5)	0.15(2)	139 ± 3	4.201	1.93
HEM <sub>1to1</sub>	1.80(4)	5.0357(8)	13.7943(5)	0.07(8)	298 ± 4	4.424	1.84

Table 2: Scattering paths, coordination numbers (CN),  $\Delta r$ , and  $\sigma^2$  of the angelellite-like cluster fit to sample HEM<sub>1to1</sub>. The third shell was split into 3-1 and 3-2 with two independent  $\Delta r$  values.

	d (Å)	CN	$\Delta r$	$\sigma^2$
Shell 1 (As-O)	1.692	4.190	0.002	0.005
Shell 2 (As-Fe)	3.313	1.047	-0.115	0.006
Shell 2 (As-O)	2.804, 3.135, 3.247, 3.299, 3.350, 3.361, 3.403, 3.424			
Shell 3-1 (As-Fe)	3.828, 4.075, 4.437	0.966	0.134	0.006
Shell 3-1 (As-O)	3.768, 3.877, 4.258, 4.575, 4.653, 4.712			
Shell 3-1 (As-As)	3.698			
Shell 3-2 (As-Fe)	3.929, 4.025, 4.487	0.966	-0.188	0.006
Shell 3-2 (As-O)	3.844, 3.847, 3.933, 4.013, 4.019, 4.052, 4.201, 4.231, 4.251, 4.038			

$\Delta E_0 = -2.51$ ,  $N_{\text{var}} = 7$ ,  $N_{\text{idp}} = 26.5$ ,  $R = 0.018$ , k range 2.8-12.2, R range 1-4.5, R window type: hanning



Abstract artwork (TOC)

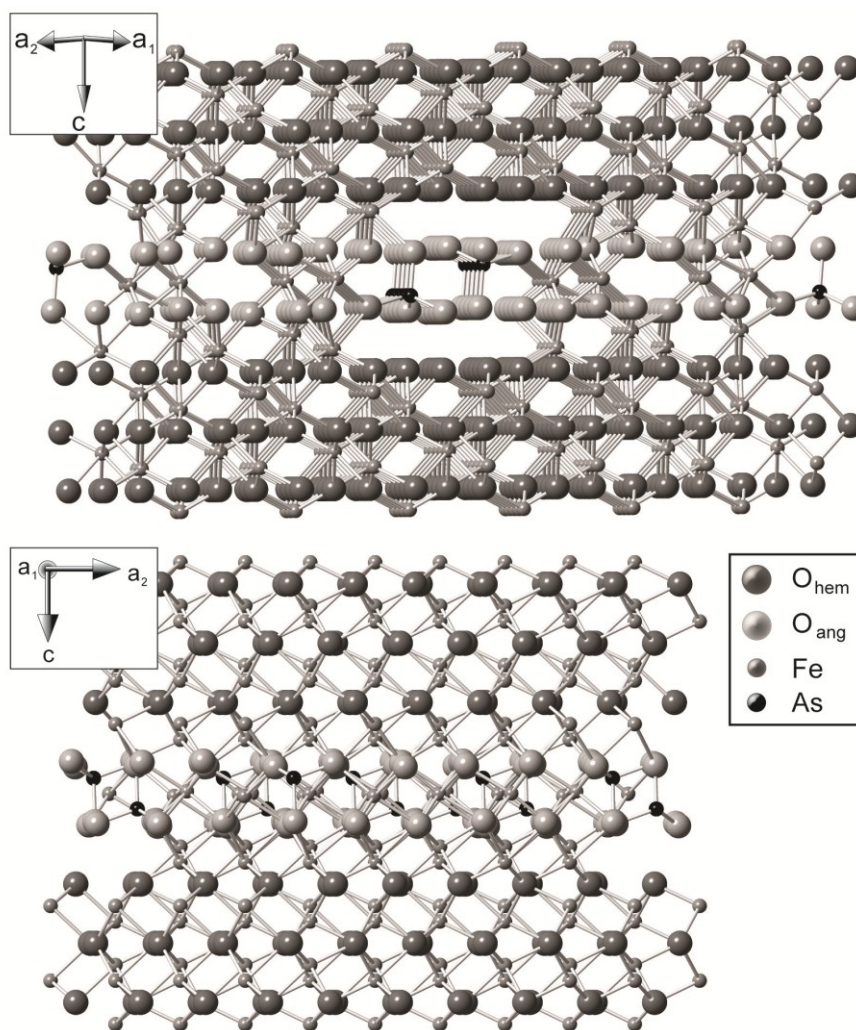


Figure 1: The structure of hematite with an included angelellite-like cluster. The (210) plane of angelellite runs parallel to the (0001) plane of hematite.  $\text{Fe}^{3+}$  atoms of the hematite structure closer than  $3.1 \text{ \AA}$  to the next  $\text{As}^{5+}$  atom of angelellite were excluded. A colored version of this figure is available in the supplementary material (Figure 2S).

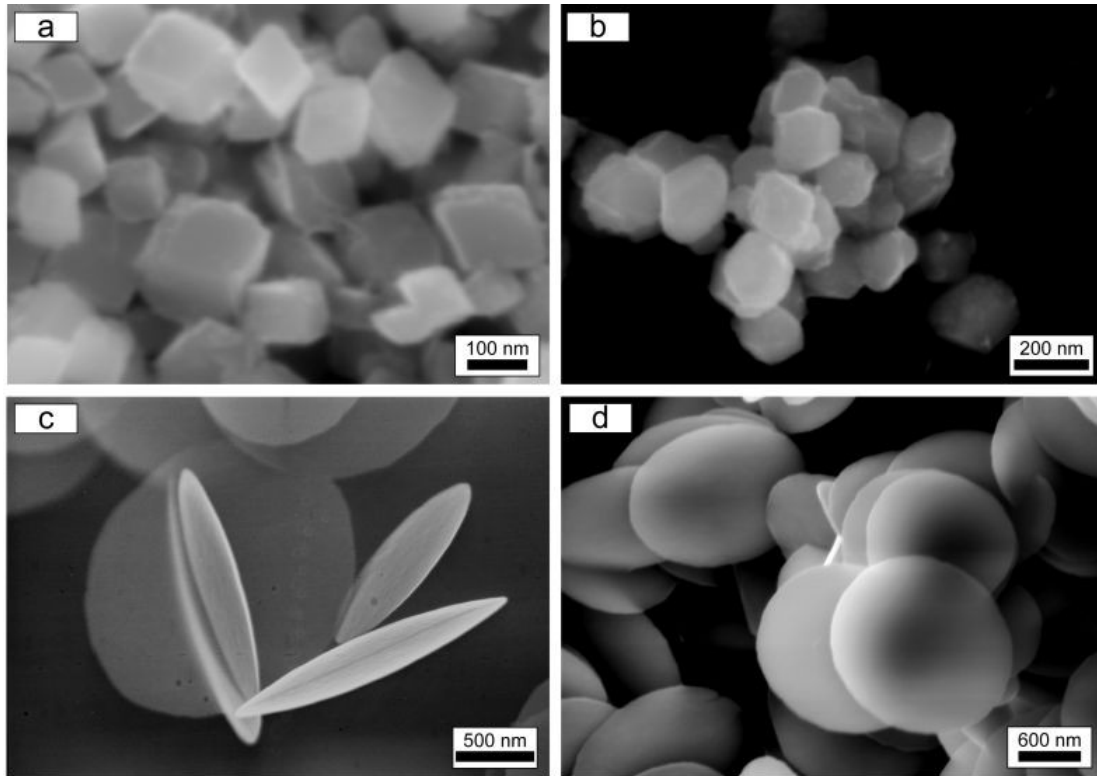


Figure 2: SEM microphotographs of the ferrihydrite transformation products. (a) rhombohedral crystals of hematite grown at 70°C at pH 4 in the absence of  $\text{As}^{5+}$  in aqueous solution. (b) rhombohedral hematite crystals grown at 70 °C at pH 4 in 0.23 mM  $\text{As}^{5+}$  solution. (c) disc-shaped hematite crystals grown at 200 °C at pH 4 at an molar As : Fe ratio of 1. (d) disc-shaped crystals of angelellite grown at 700 °C via a solid-state synthesis.

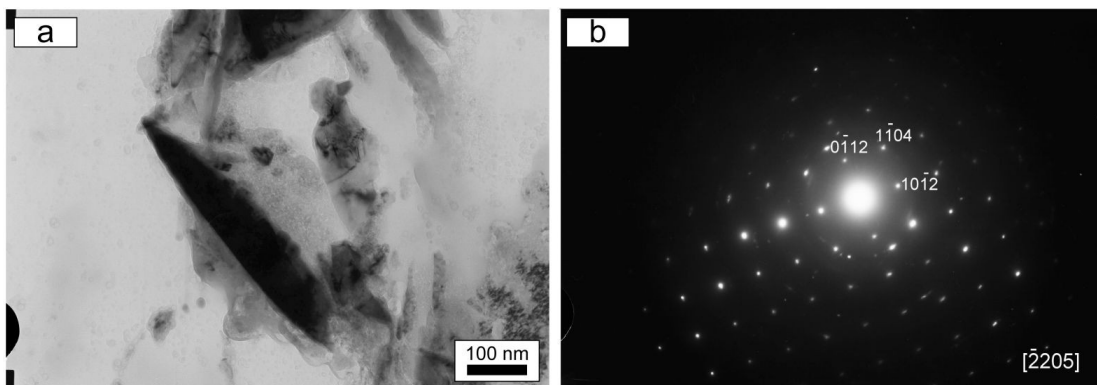


Figure 3: Bright field TEM image (a) and corresponding selected area electron diffraction pattern (b) of a sliced hematite crystal. The crystal is oriented near the  $[\bar{2} 205]$  zone axis parallel to the primary electron beam.



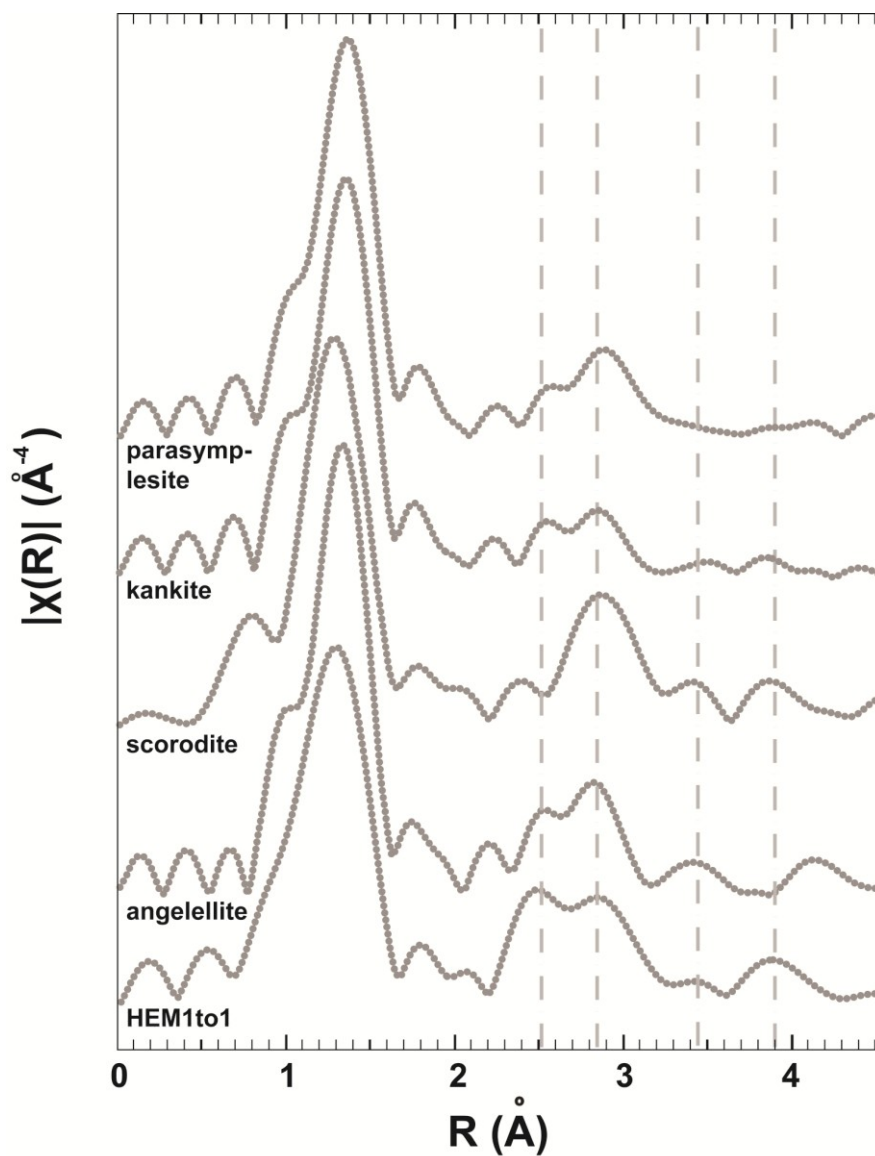


Figure 4: Fourier transforms of the As K-edge spectra taken from sample HEM<sub>1to1</sub> (a), angelellite (b), scorodite (c), kankite (d), and parasymplectite (e). The grey dashed lines indicate prominent features of the second and third shell of sample HEM<sub>1to1</sub>.

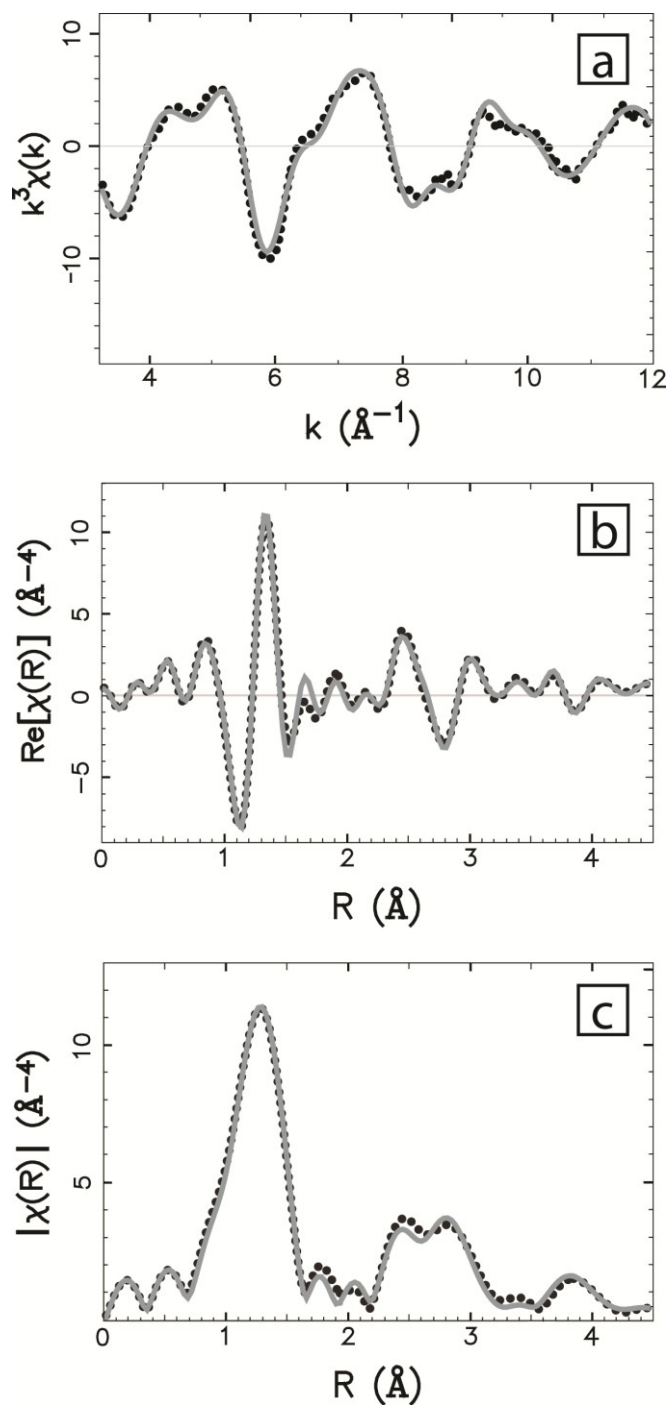


Figure 5: (a) Normalized,  $k^3$ -weighted As K-edge EXAFS spectrum of sample  $\text{HEM}_{1\text{to}1}$ . (b) real part of the Fourier transform of the As K-edge EXAFS spectrum of sample  $\text{HEM}_{1\text{to}1}$ . (c) magnitude of the Fourier transform of the As K-edge EXAFS spectrum of sample  $\text{HEM}_{1\text{to}1}$ . The black dots indicate the measured data, whereas the solid grey lines show the achieved fit.

# Supplementary figures, tables, and files to:

*R.M. Bolanz, M. Wierzbicka-Wieczorek, M. Čaplovičová, P. Uhlík, J.*

*Göttlicher, R. Steininger, and J. Majzlan:*

*Structural incorporation of As<sup>5+</sup> in hematite*

Submitted to *Environmental Science & Technology*

## CONTENT

- Figure 1S: (a) SEM microphotograph of a disc-shaped hematite crystal grown at 200°C, pH 4, and a molar As : Fe ratio of 1. (b) Scheme of the part, which was sliced out of the hematite crystal. The cut was chosen to be parallel to the flattening direction of the spheroidal particle. (c) Slice of a hematite crystal which was analyzed later by TEM-EDX.
- Figure 2S. Images of the structure of angelellite-like clusters, intergrown with hematite. O<sup>2-</sup> atoms belonging to the original hematite structure are marked in red, Fe<sup>3+</sup> atoms belonging to hematite are marked in brown. The O<sup>2-</sup> atoms of angelellite are marked in green, whereas the Fe<sup>3+</sup> atoms are marked in blue. As<sup>5+</sup> atoms are marked in violet.
- Figure 3S: Image of the angelellite-like cluster, which was used for the FEFF calculation. The radius of three spheres around three adjacent As atoms was chosen to be 5 Å. O<sup>2-</sup> atoms belonging to the original hematite structure are marked in red, Fe<sup>3+</sup> atoms belonging to hematite are marked in brown. The O<sup>2-</sup> atoms of angelellite are marked in green, whereas the Fe<sup>3+</sup> atoms are marked in blue. As<sup>5+</sup> atoms are marked in violet.
- Figure 4S. Structures of interest as described in the corresponding section. The structure of hematite was taken from Blake et al. (1966), angelellite (Moore & Araki, 1978), scorodite (Kitahama et al., 1975), kaňkite (unpublished data), and parasymphesite (Mori & Ito, 1950).
- Figure 5S: XANES spectra of sample HEM<sub>1to1</sub>, reference compounds, and As<sub>2</sub>O<sub>5</sub> and As<sub>2</sub>O<sub>3</sub> for the determination of the oxidation state of arsenic.

- Figure 6S: (a) Fit of the structure of angelellite to sample HEM<sub>1to1</sub> as real part of the Fourier transform of the As K-edge EXAFS spectrum. (b) Fit of the structure of angelellite to sample HEM<sub>1to1</sub> as magnitude of the Fourier transform of the As K-edge EXAFS spectrum. (c) Fit of the structure of scorodite to sample HEM<sub>1to1</sub> as real part of the Fourier transform of the As K-edge EXAFS spectrum. (d) Fit of the structure of scorodite to sample HEM<sub>1to1</sub> as magnitude of the Fourier transform of the As K-edge EXAFS spectrum. The blue dots indicate the measured data, whereas the solid red lines show the achieved fit.
- Figure 7S: Powder XRD pattern of sample HEM<sub>1to1</sub>. The red bars show the calculated hematite peak positions.
- Table 1S: Scattering paths, coordination numbers (CN),  $\Delta r$ , and  $\sigma^2$  of angelellite fit to sample HEM<sub>1to1</sub>. The third shell was split into 3-1 and 3-2 with two independent  $\Delta r$  values. Values with an asterisk (\*) were restrained during the fit.
- Table 2S: Scattering paths, coordination numbers (CN),  $\Delta r$ , and  $\sigma^2$  of scorodite fit to sample HEM<sub>1to1</sub>. Values with an asterisk (\*) were restrained during the fit.
- Table 3S: Scattering paths, coordination numbers (CN),  $\Delta r$ , and  $\sigma^2$  of the angelellite-like cluster fit to sample HEM<sub>1to1</sub>. The third shell was split into 3-1 and 3-2 with two independent  $\Delta r$  values.
- File 1S: Crystallographic information file for the angelellite-like sheeted cluster used for EXAFS fitting.

Figure 1S. (a) SEM microphotograph of a disc-shaped hematite crystal grown at 200°C, pH 4, and a molar As : Fe ratio of 1. (b) Scheme of the part, which was sliced out of the hematite crystal. The cut was chosen to be parallel to the flattening direction of the spheroidal particle. (c) Slice of a hematite crystal which was analyzed later by TEM-EDX.

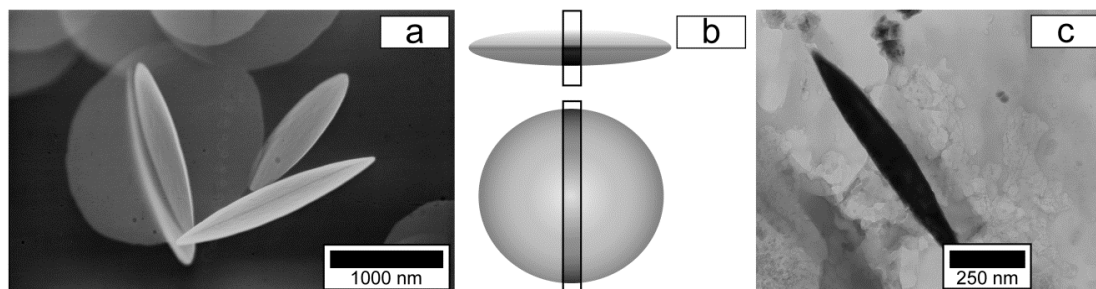


Figure 2S. Images of the structure of angelellite-like clusters, intergrown with hematite.  $O^{2-}$  atoms belonging to the original hematite structure are marked in red,  $Fe^{3+}$  atoms belonging to hematite are marked in brown. The  $O^{2-}$  atoms of angelellite are marked in green, whereas the  $Fe^{3+}$  atoms are marked in blue.  $As^{5+}$  atoms are marked in violet.

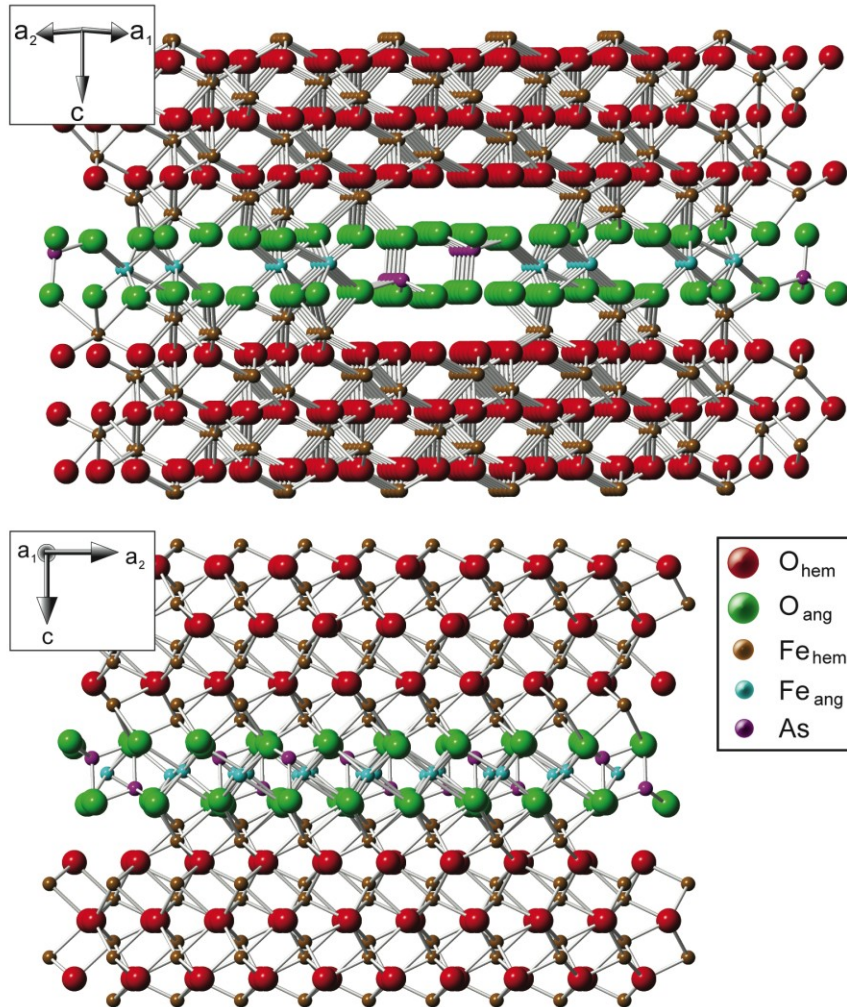


Figure 3S: Image of the angelellite-like cluster, which was used for the FEFF calculation. The radius of three spheres around three adjacent As atoms was chosen to be 5 Å. O<sup>2-</sup> atoms belonging to the original hematite structure are marked in red, Fe<sup>3+</sup> atoms belonging to hematite are marked in brown. The O<sup>2-</sup> atoms of angelellite are marked in green, whereas the Fe<sup>3+</sup> atoms are marked in blue. As<sup>5+</sup> atoms are marked in violet.

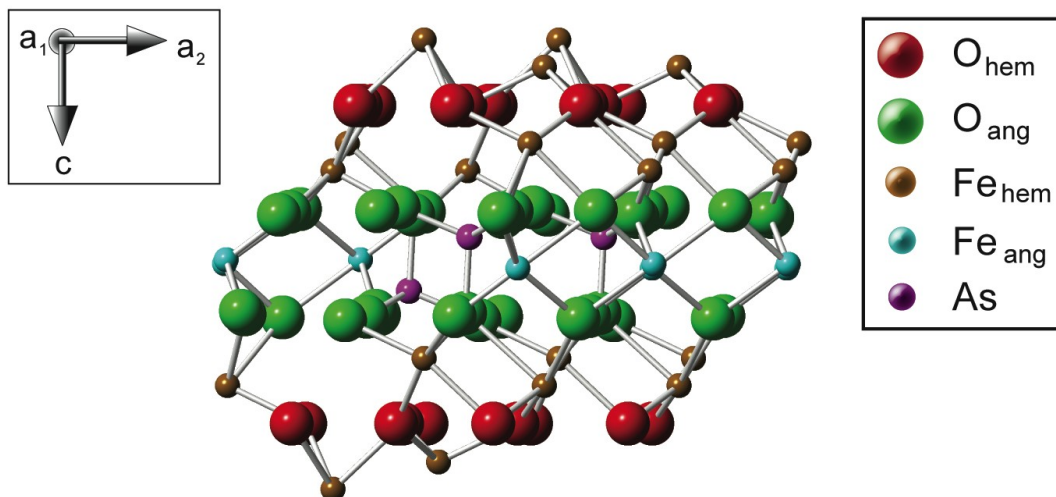


Figure 4S: Structures of interest as described in the corresponding section. The structure of hematite was taken from Blake et al. (1966), angelellite (Moore & Araki, 1978), scorodite (Kitahama et al., 1975), kaňkite (unpublished data), and parasymphesite (Mori & Ito, 1950).

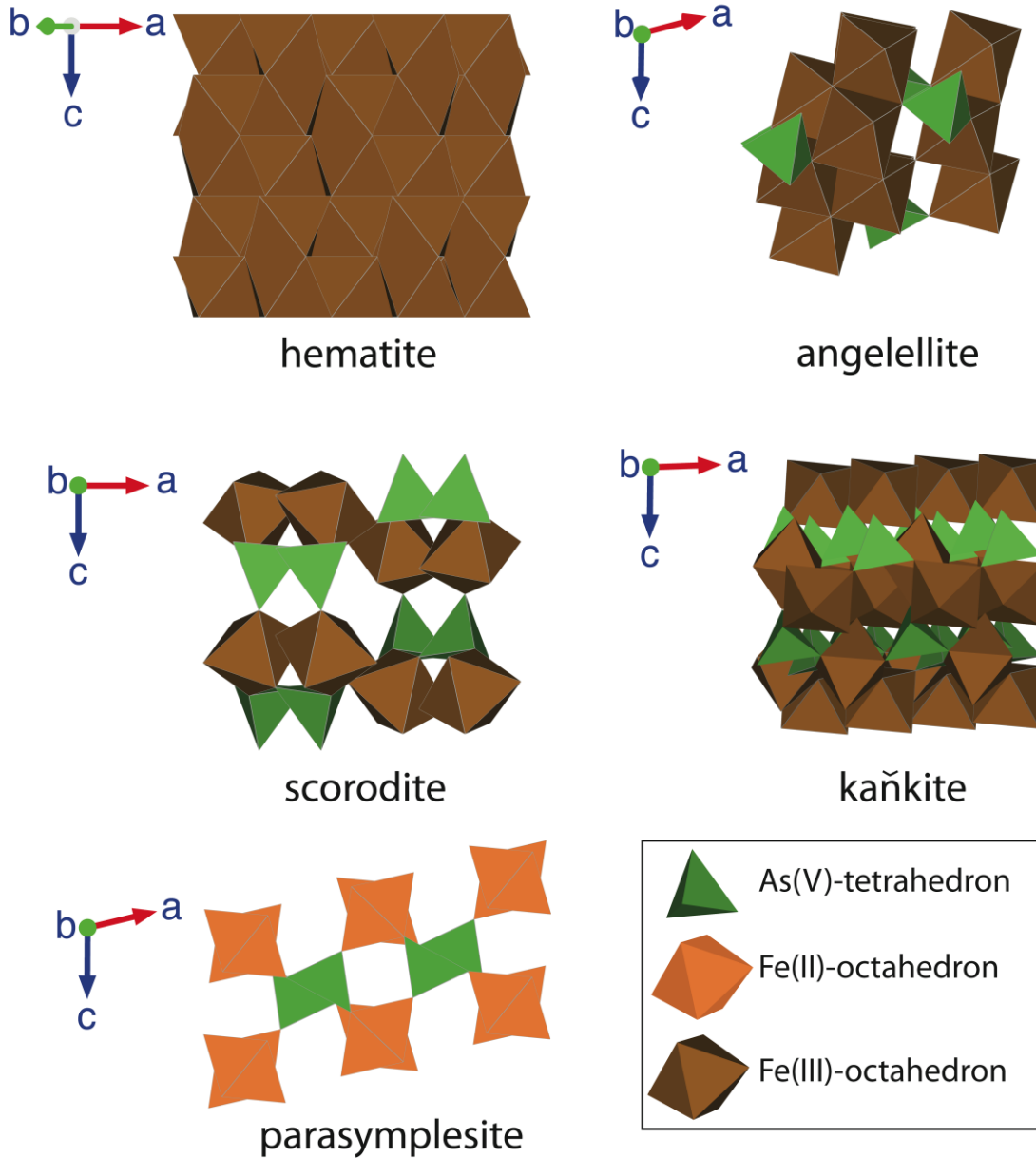




Figure 5S: XANES spectra of sample HEM<sub>1to1</sub>, reference compounds, and As<sub>2</sub>O<sub>5</sub> and As<sub>2</sub>O<sub>3</sub> for the determination of the oxidation state of arsenic.

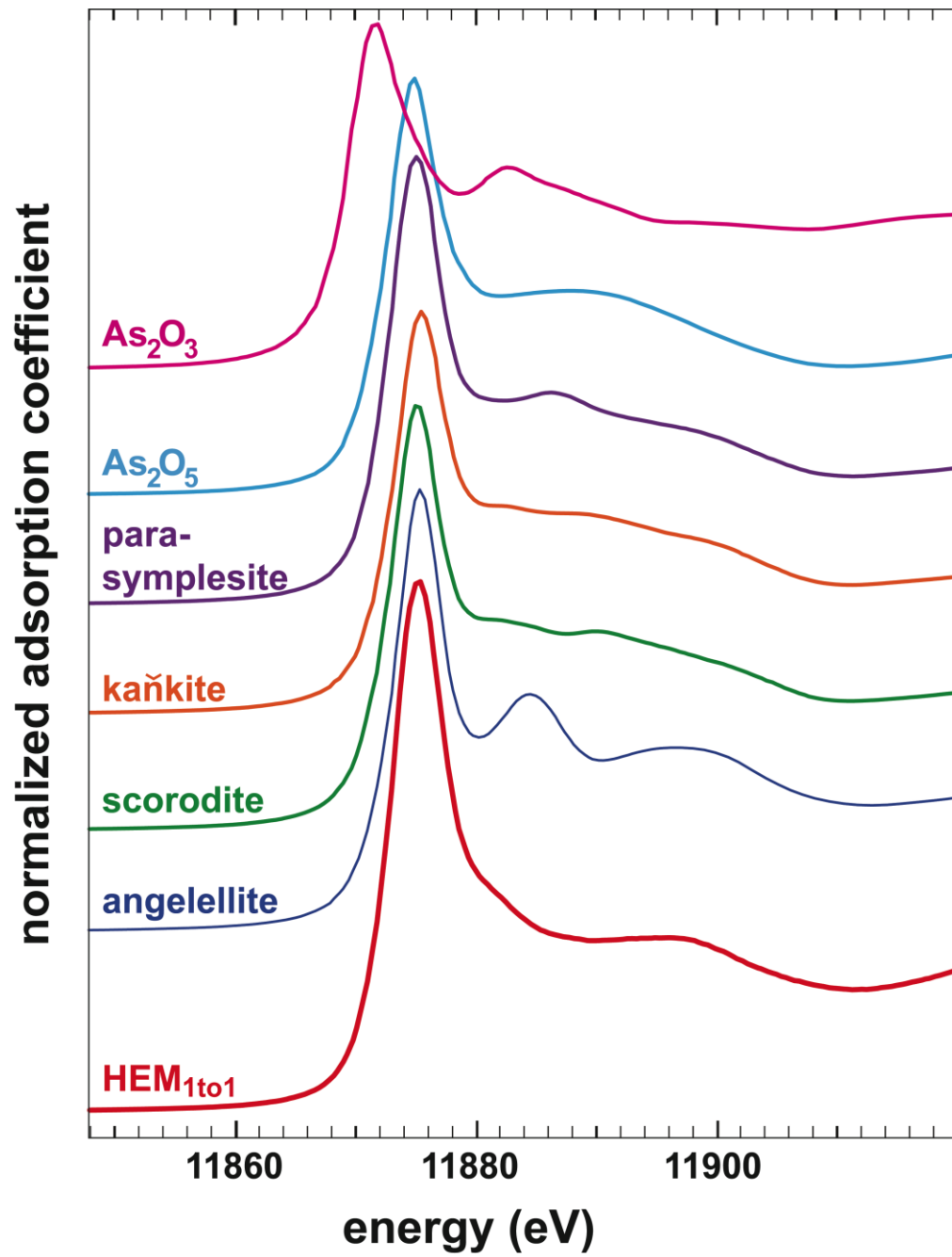


Figure 6S: (a) Fit of the structure of angelellite to sample HEM<sub>1to1</sub> as real part of the Fourier transform of the As K-edge EXAFS spectrum. (b) Fit of the structure of angelellite to sample HEM<sub>1to1</sub> as magnitude of the Fourier transform of the As K-edge EXAFS spectrum. (c) Fit of the structure of scorodite to sample HEM<sub>1to1</sub> as real part of the Fourier transform of the As K-edge EXAFS spectrum. (d) Fit of the structure of scorodite to sample HEM<sub>1to1</sub> as magnitude of the Fourier transform of the As K-edge EXAFS spectrum. The blue dots indicate the measured data, whereas the solid red lines show the achieved fit.

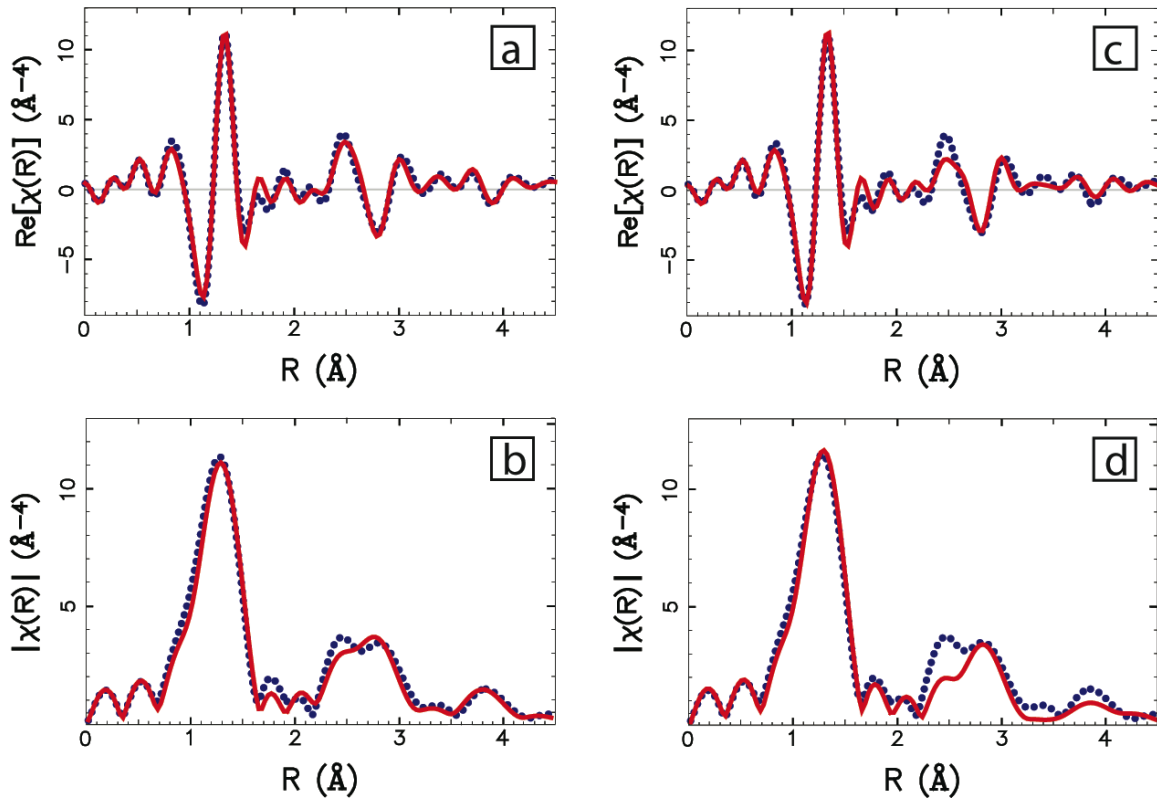


Figure 7S: Powder XRD pattern of sample HEM<sub>1to1</sub>. The red bars indicate the calculated hematite peak positions until 90 °2 $\theta$ .

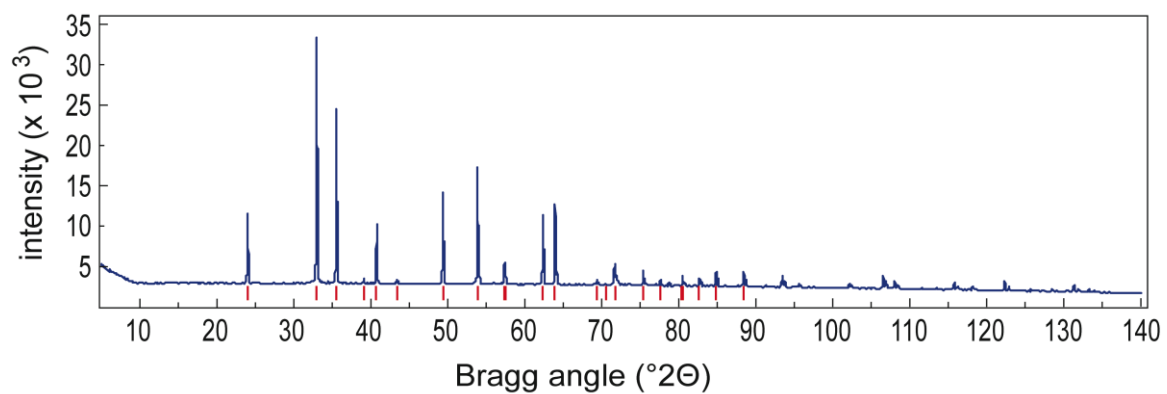


Table 1S: Scattering paths, coordination numbers (CN),  $\Delta r$ , and  $\sigma^2$  of angelellite fit to sample HEM<sub>1to1</sub>. The third shell was split into 3-1 and 3-2 with two independent  $\Delta r$  values. Values with an asterisk (\*) were restrained during the fit.

	d (Å)	CN	$\Delta r$	$\sigma^2$
Shell 1 (As-O)	1.704	4.183	0.038	0.005
Shell 2 (As-Fe)	3.211, 3.266, 3.321, 3.337, 3.394, 3.414	1.050	-0.014	0.011
Shell 2 (As-O)	3.235, 3.347, 3.347, 3.380, 3.401, 3.404, 3.453, 3.463, 3.505			
Shell 3-1 (As-Fe)	3.482	1.000*	-0.054	0.014
Shell 3-1 (As-O)	3.689, 4.191, 4.213, 4.336, 4.363, 4.365, 4.431, 4.441			
Shell 3-1 (As-As)	4.392			
Shell 3-2 (As-Fe)	4.012, 4.108, 4.108	1.000*	-0.201	0.014
Shell 3-2 (As-O)	3.336, 3.337, 3.434, 3.928, 4.041, 4.092			
Shell 3-2 (As-As)	3.363, 4.378, 4.378			

$\Delta E_0 = 1.018$ ,  $N_{\text{var}} = 9$ ,  $N_{\text{idp}} = 26.5$ ,  $R = 0.026$ , k range 2.8-12.2, R range 1-4.5, R window type: hanning

Table 2S: Scattering paths, coordination numbers (CN),  $\Delta r$ , and  $\sigma^2$  of scorodite fit to sample HEM<sub>1to1</sub>. Values with an asterisk (\*) were restrained during the fit.

	d (Å)	CN	$\Delta r$	$\sigma^2$
Shell 1 (As-O)	1.699	4.170	0.030	0.005
Shell 2 (As-Fe)	3.342, 3.350, 3.367, 3.392	1.000*	0.004	0.012
Shell 2 (As-O)	3.247, 3.833, 3.996, 4.019			
Shell 2 (As-OH)	3.359, 3.460, 3.462, 3.492, 3.589, 3.777, 3.950			
Shell 3 (As-Fe)		1.044	0.182	0.007
Shell 3 (As-O)	4.324, 4.438, 4.461			
Shell 3 (As-OH)	4.298, 4.369			
Shell 3 (As-As)	??????			

$\Delta E_0 = -0.312$ ,  $N_{\text{var}} = 9$ ,  $N_{\text{idp}} = 26.5$ ,  $R = 0.043$ , k range 2.8-12.2, R range 1-4.5, R window type: hanning

Table 3S: Scattering paths, coordination numbers (CN),  $\Delta r$ , and  $\sigma^2$  of the angelellite-like cluster fit to sample HEM<sub>1to1</sub>. The third shell was split into 3-1 and 3-2 with two independent  $\Delta r$  values.

	d (Å)	CN	$\Delta r$	$\sigma^2$
Shell 1 (As-O)	1.692	4.190	0.002	0.005
Shell 2 (As-Fe)	3.313	1.047	-0.115	0.006
Shell 2 (As-O)	2.804, 3.135, 3.247, 3.299, 3.350, 3.361, 3.403, 3.424			
Shell 3-1 (As-Fe)	3.828, 4.075, 4.437	0.966	0.134	0.006
Shell 3-1 (As-O)	3.768, 3.877, 4.258, 4.575, 4.653, 4.712			
Shell 3-1 (As-As)	3.698			
Shell 3-2 (As-Fe)	3.929, 4.025, 4.487	0.966	-0.188	0.006
Shell 3-2 (As-O)	3.844, 3.847, 3.933, 4.013, 4.019, 4.052, 4.201, 4.231, 4.251, 4.038			

$\Delta E_0 = -2.51$ ,  $N_{var} = 7$ ,  $N_{idp} = 26.5$ ,  $R = 0.018$ , k range 2.8-12.2, R range 1-4.5, R window type: hanning

## File 1S: Crystallographic information file for the angelellite-like sheeted cluster used for EXAFS fitting.

```

#####
# Cluster Data
#-----
_cell_length_a      14.9298(0)
_cell_length_b      19.1102(0)
_cell_length_c      19.3250(0)
_cell_angle_alpha   90.0000(0)
_cell_angle_beta    90.0000(0)
_cell_angle_gamma   90.0000(0)

_symmetry_space_group_name_H-M  'P 1'
_symmetry_int_tables_number      1
_symmetry_cell_setting          triclinic
loop_
_symmetry_equiv_pos_as_xyz
'+x,+y,+z'

loop_
_atom_site_label
_atom_site_type_symbol
_atom_site_occupancy
_atom_site_fract_x
_atom_site_fract_y
_atom_site_fract_z
As  As 1.0000  0.4805  0.4538  0.6229
As  As 1.0000  0.5604  0.3842  0.4633
As  As 1.0000  0.4805  0.6098  0.4128
Fe  Fe 1.0000  0.6605  0.7140  0.2726
Fe  Fe 1.0000  0.3418  0.8366  0.3617
Fe  Fe 1.0000  0.3824  0.4519  0.2439
Fe  Fe 1.0000  0.3418  0.3126  0.3043
Fe  Fe 1.0000  0.3824  0.8198  0.5113
Fe  Fe 1.0000  0.1881  0.5578  0.4826
Fe  Fe 1.0000  0.6605  0.5578  0.4826
Fe  Fe 1.0000  0.3418  0.6804  0.5718
Fe  Fe 1.0000  0.2286  0.6972  0.4222
Fe  Fe 1.0000  0.7010  0.6972  0.4222
Fe  Fe 1.0000  0.8142  0.4184  0.5431
Fe  Fe 1.0000  0.3824  0.2958  0.4539
Fe  Fe 1.0000  0.7010  0.1732  0.3648
Fe  Fe 1.0000  0.3824  0.6637  0.7214
Fe  Fe 1.0000  0.1881  0.4017  0.6927
Fe  Fe 1.0000  0.6605  0.4017  0.6927
Fe  Fe 1.0000  0.3418  0.5243  0.7818
Fe  Fe 1.0000  0.2286  0.5410  0.6322
Fe  Fe 1.0000  0.7010  0.5410  0.6322
Fe  Fe 1.0000  0.8548  0.2958  0.4539
Fe2 Fe 1.0000  0.5210  0.8240  0.5301
Fe2 Fe 1.0000  0.5210  0.6681  0.7402
Fe2 Fe 1.0000  0.5199  0.1699  0.3460
Fel Fe 1.0000  0.5143  0.1716  0.5089
Fel Fe 1.0000  0.5143  0.3276  0.2988
Fel Fe 1.0000  0.5266  0.5104  0.7874
Fel Fe 1.0000  0.5266  0.6664  0.5773
Fel Fe 1.0000  0.5266  0.8223  0.3672
O   O 1.0000  0.2852  0.7464  0.3456
O   O 1.0000  0.7576  0.6662  0.3368
O   O 1.0000  0.2852  0.6338  0.2638
O   O 1.0000  0.7576  0.4042  0.3081
O   O 1.0000  0.2852  0.4843  0.3169
O   O 1.0000  0.7576  0.3693  0.6196
O   O 1.0000  0.2852  0.4340  0.7657
O   O 1.0000  0.2852  0.4494  0.6284
O   O 1.0000  0.7576  0.4818  0.7015
O   O 1.0000  0.2852  0.3215  0.6839
O   O 1.0000  0.2852  0.5835  0.7126
O   O 1.0000  0.7576  0.2634  0.3809
O   O 1.0000  0.2852  0.3282  0.5269
O   O 1.0000  0.2852  0.3436  0.3897
O   O 1.0000  0.7576  0.3759  0.4627

```

```

O  O 1.0000  0.7576  0.2480  0.5182
O  O 1.0000  0.7576  0.5254  0.4096
O  O 1.0000  0.2852  0.5902  0.5557
O  O 1.0000  0.2852  0.6056  0.4184
O  O 1.0000  0.7576  0.6380  0.4914
O  O 1.0000  0.7576  0.5100  0.5469
O  O 1.0000  0.2852  0.4777  0.4738
O  O 1.0000  0.2852  0.7397  0.5026
O1 O 1.0000  0.4510  0.8052  0.2776
O1 O 1.0000  0.4510  0.6492  0.4877
O1 O 1.0000  0.5899  0.3447  0.3885
O1 O 1.0000  0.4510  0.4933  0.6977
O1 O 1.0000  0.5899  0.1888  0.5985
O2 O 1.0000  0.6020  0.7365  0.5169
O2 O 1.0000  0.5933  0.6051  0.4065
O2 O 1.0000  0.4476  0.5448  0.2595
O2 O 1.0000  0.6020  0.5806  0.7270
O2 O 1.0000  0.5933  0.4492  0.6166
O2 O 1.0000  0.4476  0.3888  0.4696
O2 O 1.0000  0.4389  0.2574  0.3592
O2 O 1.0000  0.4476  0.2329  0.6797
O3 O 1.0000  0.5987  0.4907  0.3178
O3 O 1.0000  0.4422  0.6592  0.3482
O3 O 1.0000  0.5987  0.3348  0.5279
O3 O 1.0000  0.4422  0.5032  0.5583
O3 O 1.0000  0.4422  0.3473  0.7684
O4 O 1.0000  0.4368  0.6842  0.1989
O4 O 1.0000  0.6041  0.6217  0.2571
O4 O 1.0000  0.4368  0.5282  0.4090
O4 O 1.0000  0.6041  0.4657  0.4671
O4 O 1.0000  0.4368  0.3723  0.6191
O4 O 1.0000  0.6041  0.3098  0.6772
O5 O 1.0000  0.5976  0.7488  0.3567
O5 O 1.0000  0.5976  0.5929  0.5667
O5 O 1.0000  0.4433  0.4011  0.3094
O5 O 1.0000  0.5976  0.4369  0.7768
O5 O 1.0000  0.4433  0.2451  0.5194
O6 O 1.0000  0.4412  0.7567  0.5745
O6 O 1.0000  0.5956  0.3490  0.2206
O6 O 1.0000  0.4453  0.8009  0.4455
O6 O 1.0000  0.4412  0.6007  0.7845
O6 O 1.0000  0.5956  0.1931  0.4307
O6 O 1.0000  0.4453  0.6449  0.6555
O6 O 1.0000  0.5997  0.2373  0.3016
O6 O 1.0000  0.4453  0.4890  0.8656

```

**REFERENCES**

- Blake, R.L.; Hessevic, R.E.; Zoltai, T.; Finger, L.W. Refinement of hematite structure. *Am. Mineral.* **1966**, 51, 123-129.
- Kitahama, K.; Kiriyaama, R.; Baba, Y. Refinement of the crystal structure of scorodite. *Acta Cryst.* **1975**, B31, 322-324.
- Moore, P.B.; Araki, T. Angelellite,  $\text{Fe}_4^{3+}\text{O}_3(\text{As}^{5+}\text{O}_4)_2$ : a novel cubic close-packed oxide structure. *N. Jb. Miner. Abh.* **1978**, 132, 91-100.
- Mori, H.; Ito, T. The structure of vivianite and symplectite. *Acta Cryst.* **1950**, 3, 1-6.



## **Chapter three**

## **The effect of antimonate, arsenate and phosphate on the transformation of ferrihydrite to goethite, hematite, feroxyhyte, and tripuhyite**

Ralph Michael Bolanz<sup>1\*</sup>, Ulrich Bläss<sup>1</sup>, Sonia Ackermann<sup>1</sup>, Valerian Ciobotă<sup>2</sup>, Petra Rösch<sup>2</sup>, Nicolae Tarcea<sup>3</sup>, Jürgen Popp<sup>2,3</sup> and Juraj Majzlan<sup>1</sup>

<sup>1</sup>Institute of Geoscience, Friedrich-Schiller-University Jena, Germany

<sup>2</sup>Institute of Physical Chemistry, Friedrich-Schiller-University Jena, Germany

<sup>3</sup>Institute of Photonic Technology, Jena, Germany

\* corresponding author: Tel. +49-3641-948704, fax +49-3641-948602, email address: ralph.bolanz@uni-jena.de

**Submitted to: Clays and Clay Minerals, July 18, 2012**

**Review received: October 13, 2012**

**Revision submitted: November 12, 2012**

**Accepted: December 19, 2012**

**Published: February, 2013**

Reproduced according to the rules of The Clay Minerals Society, publisher of *Clays and Clay Minerals*.

**ABSTRACT**

Iron oxides, typical constituents of many soils, represent a natural immobilization mechanism for toxic elements. Most of these iron oxides are formed during the transformation of poorly crystalline ferrihydrite to more well-crystalline iron phases. This study examined the impact of well known contaminants, like P(V), As(V), and Sb(V) on the ferrihydrite transformation and investigated the transformation products with a set of bulk and nano-resolution methods. Irrespective of the pH, P(V) and As(V) favor the formation of hematite ( $\alpha$ -Fe<sub>2</sub>O<sub>3</sub>) over goethite ( $\alpha$ -FeOOH) and retard the transformation at high concentrations. Sb(V) on the other hand favors the formation of goethite, feroxyhyte ( $\delta'$ -FeOOH) and tripuhyite (FeSbO<sub>4</sub>) depending on pH and Sb(V) concentration. Elemental composition of the transformation products analyzed by ICP-OES show high loadings of Sb(V) with molar Sb:Fe ratios of 0.12, whereas molar P:Fe and As:Fe ratios do not exceed 0.03 and 0.06, respectively. The structural similarity of feroxyhyte and hematite was resolved by detailed electron diffraction studies and feroxyhyte was positively identified in a number of our samples. These results indicate, that in comparison to P(V) and As(V), Sb(V) can be incorporated into the structure of certain iron oxides through Fe(III)-Sb(V) substitution, coupled with other substitutions. However, the outcome of the ferrihydrite transformation (hematite, goethite, feroxyhyte, or tripuhyite) depends on the Sb(V)-concentration, pH and temperature.

**Keywords:** antimony, arsenic, ferrihydrite, feroxyhyte, goethite, hematite, iron oxides, phosphorous, transformation, tripuhyite

## INTRODUCTION

Iron oxides are omnipresent constituents of most soils and count as important sinks for heavy metals and toxic elements [1]. Amongst the iron oxides, poorly crystalline 2-line ferrihydrite (hereafter referred to as ferrihydrite) is the initial secondary iron oxide formed during the weathering of primary iron minerals [2]. Ferrihydrite is generally considered to be an intermediate step for the formation of well-crystalline iron oxides, such as goethite ( $\alpha$ -FeOOH) and hematite ( $\alpha$ -Fe<sub>2</sub>O<sub>3</sub>) [3]. The outcome of the ferrihydrite transformation depends on temperature, pH, and abundance of foreign ions (e.g. [3,4,5,6,7,8,9,10]). The most common products of the ferrihydrite transformation are goethite and hematite [11]. Near or at the surface of the Earth, both goethite and hematite are the two most stable iron oxides [10,11]. Although goethite and hematite can be formed by ferrihydrite transformation simultaneously [10], conditions which are favorable for goethite are unfavorable for hematite and *vice versa* [12]. The transformation of ferrihydrite to goethite is thought to be a process in which ferrihydrite dissolves and goethite is formed by nucleation/crystallization from bulk solution [11,12,13]. Hematite, on the other hand, is formed topotactically through atomic solid-solid rearrangement within the ferrihydrite matrix [3,11,12,14,]. Because of these two different competing formation mechanisms [15], one could speculate that any parameter which leads to the stabilization of ferrihydrite favors the formation of hematite, whereas any parameter leading to the dissolution of ferrihydrite favors goethite formation. The first of these parameters is the temperature. Elevated temperatures result in the aggregation of ferrihydrite particles [16] and lead to dehydration which favors the formation of hematite [3,11]. The second parameter is the pH. At room temperature, ferrihydrite is least soluble at pH 7-8 [12], where goethite formation has its minimum and hematite is favored. Conversely, goethite formation from ferrihydrite has its maximum at pH 12

in alkaline media and pH 4 in acidic media at room temperature [12]. The third notable parameter is the abundance of foreign ions during the transformation process, which can affect the transformation rate and cause variations in the transformation products (see [11,17] for a summary).

The focus of this study lies on the transformations of ferrihydrite in the presence of P(V), As(V), and Sb(V). In aqueous solution P(V) and As(V) are both coordinated tetrahedrally by four oxygen atoms and show, at pH 4-12, the same species ( $\text{H}_2\text{P}/\text{AsO}_4^-$ ,  $\text{HP}/\text{AsO}_4^{2-}$ , and  $\text{P}/\text{AsO}_4^{3-}$ ) [18]. Sb(V), however, displays from pH 4-12 only one dominant specie,  $\text{Sb}(\text{OH})_6^-$  [19]. In the presence of phosphate, the solubility [20] and consequently the transformation rate of ferrihydrite is reduced [7], further the aggregation of colloidal iron oxide particles is observed [21], which leads to a preferred formation of hematite [7]. In the same way as phosphate, arsenate favors the aggregation of ferrihydrite, decreases the transformation rate and promotes the formation of hematite over goethite [6].

P(V), As(V), and Sb(V) may occur together in Sb-mine tailings and compete for the same adsorption sites on the surfaces of the more abundant minerals, especially ferrihydrite or its transformation products goethite and hematite. This study therefore examines the transformation of ferrihydrite into other, better crystalline iron oxides in the presence of antimonate, and compares the results with those for phosphate- and arsenate-doped ferrihydrite, transformed at the same conditions. To our knowledge, no comparable transformation experiments were performed with antimonate. The newly formed products were characterized with a set of bulk and nano-resolution methods.

## MATERIALS AND METHODS

Two-line ferrihydrite was synthesized after [22]. A mass of 10.1 g  $\text{Fe}(\text{NO}_3)_3 \cdot 9\text{H}_2\text{O}$  (Alfa Aesar) was dissolved in 200 mL deionized water and transformed into 2-line ferrihydrite by adding 45 mL 5 M potassium hydroxide (Merck) solution under constant stirring. The suspension was adjusted to 490 mL with deionized water, resulting in an end-point pH of about 13. The suspension was afterwards adjusted to 500 mL with deionized water. The resulting brown aggregates (flocks) settled after a few minutes in suspension and showed a dry weight of ~7 g (air-dried). The so-synthesized ferrihydrite slurry was immediately adjusted to the desired pH (4, 7, or 12) by adding nitric acid (65 %) (J.T. Baker) and doped with pre-selected volumes of a 15 mM solution of potassium hexahydroxoantimonate (Merck) for Sb(V), arsenic pentoxide (Alfa Aesar) for As(V), and potassium dihydrogen phosphate (Merck) for P(V). Previous studies indicated that nitrate does not significantly interfere with the adsorption of P(V), As(V), and Sb(V) onto amorphous  $\text{Fe}(\text{OH})_3$  [23,24]. The synthesized ferrihydrite was therefore not washed, in order to keep the calculated Fe concentration and thus, the Fe to P/As/Sb ratio constant. The volumes of the doping solutions were calculated to arrive at the P(V)/As(V)/Sb(V) molarity of 0 mM, 0.225 mM, 0.750 mM, 2.250 mM and 6.000 mM after adjusting to 500 mL with deionized water. After bringing the volume to about 490 mL, the pH was checked and adjusted again if necessary by adding nitric acid (65 %) or 5 M potassium hydroxide solution and the volume finally brought to 500 mL with deionized water. The samples were then stored at 70 °C for up to 16 days and sample aliquots were taken every second day, washed, air-dried, and sealed in glass vials. The synthesis of ferrihydrite involves high pH conditions under which Si may be mobilized into the aqueous solutions. That is why no glassware, but exclusively polyethylene (PE) containers were used during this work.

A second series of ferrihydrite samples was synthesized as described above. In this series, ferrihydrite was doped at pH 4 in smaller concentration steps with molar Sb:Fe ratios of 0.000-0.080 in steps of 0.005; 0.090; 0.100; 0.300; 0.300-0.500 in steps of 0.025; and 0.500-1.000 in steps of 0.100. The doped ferrihydrite was again incubated for 16 days at 70 °C, washed, air-dried, and sealed in glass vials.

Several reference compounds were synthesized for the Raman spectroscopy measurements. The hematite ( $\alpha$ -Fe<sub>2</sub>O<sub>3</sub>) reference was synthesized by transforming 2-line ferrihydrite at pH 4 and 70 °C in aqueous solution for 16 days. The sample was washed, air-dried, and sealed in a glass vial. Pure feroxyhyte ( $\delta'$ -FeOOH) was synthesized after [22]. A mass of 5.96 g FeCl<sub>2</sub>·4H<sub>2</sub>O was dissolved in 300 mL deionized water and adjusted to pH 8 with 5 M sodium hydroxide solution. Rapidly, 40 mL H<sub>2</sub>O<sub>2</sub> (30%) were added and the pH was again adjusted to 8. The product was washed, air-dried, and sealed in glass vials. Tripuhyite reference 1 was synthesized according to a modified recipe of [25]. A solution of 0.1 M Fe<sub>2</sub>(SO<sub>4</sub>)<sub>3</sub>·H<sub>2</sub>O (Sigma-Aldrich) was mixed with a 0.1 M KSb(OH)<sub>6</sub> (Merck) solution in a ratio of 1:2. The brown precipitate was refluxed for three days at 100 °C, afterwards washed, air-dried, and sealed in a glass vial. Tripuhyite reference 2 was synthesized after a modified recipe of [26]. Hematite, synthesized as described above, was mixed with Sb<sub>2</sub>O<sub>5</sub> (Alfa Aesar) and heated in a sintered corundum crucible for 24 h at 600 °C, followed by 48 h at 900 °C and afterwards cooled down over 12 h to 25 °C. Immediately after the synthesis tripuhyite was washed, air-dried, and sealed in a glass vial. All reference compounds were analyzed and checked for impurities by X-ray diffraction.

The pH was measured with a pH100 pH-meter (VWR), which was calibrated with a pH 6.86 (HANNA Instruments) and a pH 4.00 buffer solution (HANNA Instruments) according to the calibration procedure.

Elemental composition (P, As, Sb, and Fe) was determined by inductively-coupled plasma optical emission spectrometry (ICP-OES) with a Variant 725 ICP-OES with a charge-coupled device (CCD) detector.

Powder X-ray diffraction (XRD) patterns were collected using a Bruker D8 Advance DaVinci diffractometer, employing Cu  $K\alpha$  radiation ( $\lambda = 1.54058 \text{ \AA}$ ). The patterns were collected at room temperature between 5 and 90  $^{\circ}2\theta$ , with a step size of 0.02  $^{\circ}2\theta$  and a collecting time per step of 1 s. The proportions of the phases in the samples were extracted from the XRD patterns. To check the procedure, a standard was prepared containing 25 wt% ferrihydrite, 25 wt% goethite, 25 wt% hematite, and 25 wt% feroxyhyte. In order to quantify the area (intensity) of the following reflections, the program Fityk 0.9.8 [27] was used: ferrihydrite 33.90  $^{\circ}2\theta$ , goethite 21.37  $^{\circ}2\theta$  (101), 24.15  $^{\circ}2\theta$  hematite (012) and 35.13  $^{\circ}2\theta$  feroxyhyte (100). The obtained intensities were normalized for hematite and feroxyhyte to 100 % and all intensities were weighted by  $I/I_{\text{cor}}$  values, taken from the Crystallography Open Database (COD); ferrihydrite 1.03 (COD 9012761), goethite 2.92 (COD 9002158), hematite 4.82 (COD 1011267) and feroxyhyte 2.27 (COD 1008762). This method allowed us to quantify all phases in the samples with an inaccuracy  $< 5 \text{ wt\%}$  for the prepared standard. Since the incorporation of elements heavier than iron (e.g. As, Sb) into the iron oxides can affect the XRD peak intensities, this effect has to be considered as a minor but nevertheless additional error which was not taken into account.

Morphology determination and grain size for goethite and hematite were analyzed by scanning electron microscopy (SEM) using a Carl Zeiss ULTRA PLUS FE-SEM



operating at 20 kV with an Inlens SE-detector. Several milligram of air-dried sample was distributed over a conductive carbon pad with adhesive properties (PLANO). Since all studied samples are  $<1 \mu\text{m}$  the samples were not coated with carbon which could have covered morphological characteristics.

Morphological characteristics, grain size, and electron diffraction of feroxyhyte samples were studied by TEM using a LEO922 OMEGA operating at 200 kV with an in-column Omega filter and energy dispersive X-ray (EDX) detector. For preparation, the feroxyhyte sample was suspended in ethanol, placed on a Lacey copper grid, and air-dried.

The specific surface area of selected transformation products was analyzed using the Brunauer-Emmet-Teller (BET) method [28] with a Quantachrome Autosorb automated gas sorption system. About 0.2 g of the sample was outgased at  $70 \text{ }^\circ\text{C}$  for 2-7 h and measured using liquid  $\text{N}_2$  as adsorbate gas.

Raman analyses of the iron oxides were performed with a commercial micro-Raman setup (HR LabRam inverse system, Jobin Yvon Horiba). Raman scattering was excited by a frequency doubled Nd:YAG laser at a wavelength of 532 nm with a laser power of  $\sim 20 \mu\text{W}$  incident on the sample. The low values for the laser power was chosen to prevent an alteration of the sample. The laser beam was focused on the sample by means of a Leica PLFluor x100/0.75 microscope objective down to a spot diameter of approximately  $0.7 \mu\text{m}$ . The dispersive spectrometer has an entrance slit of  $100 \mu\text{m}$ , a focal length of 800 mm and is equipped with a grating of 300 lines/mm. The Raman scattered light was detected by a Peltier cooled CCD detector. The integration times for one Raman spectrum range from 60 to 1000 s.

## RESULTS

### *Morphology and surface area*

The synthesized ferrihydrite samples have a specific surface area of 252 m<sup>2</sup>/g, in good agreement with other studies [29,30]. Goethite synthesized at pH 12 consists of acicular crystals of 250-1750 nm in length and 80-200 nm in diameter with a specific surface area of 25 m<sup>2</sup>/g, whereas hematite synthesized at pH 4 displays rhombohedral-shaped crystals with a particle size of 35-260 nm and a specific surface area of 30 m<sup>2</sup>/g. These values are consistent with the existing literature [11]. Feroxyhyte samples formed at pH 4 and Sb(V) concentrations of 6 mM, show rhombohedral crystals with a size of 10-30 nm and a specific surface area of 94 m<sup>2</sup>/g, which is less than the given values for Sb-free feroxyhyte of 140-240 m<sup>2</sup>/g [31].

### *Products of transformation experiments (XRD, Raman spectroscopy, and TEM)*

The transformation experiments are pictorially summarized in Figure 1. In this figure, the results of the 405 runs can be seen at a glance. The phases produced in the runs are color-coded and the pie charts show the quantitative proportions of the phases. The results are sorted according to the two principal variables used in the runs, starting pH of the solution and the molarity of a pentavalent cation, either P(V), As(V), or Sb(V). Temperature was kept constant at 70 °C in all runs.

In acidic conditions (**pH 4**) and absence of P(V), As(V), or Sb(V), ferrihydrite transformed at 70 °C completely to hematite within eight days (Figure 1), an expected result, considering the preferred formation of hematite at elevated temperatures [11]. In the presence of P(V) and As(V), the transformation rate

generally declined with increasing concentrations, to a complete inhibition at 6.00 mM P(V)/As(V). The presence of Sb(V), however, lead to a more complex transformation behavior. At low Sb(V) concentrations (0.225 mM), the transformation to hematite was slightly retarded. With increasing Sb(V) concentrations, goethite appeared in addition to hematite and the transformation rate was diminished. At 6.00 mM Sb(V), surprisingly, the transformation rate suddenly increased with feroxyhyte as the only crystalline transformation product after six days.

At neutral pH (**pH 7**), the transformation of pure ferrihydrite took 12 days and yielded a mixture of 70 wt% hematite and 30 wt% goethite. P(V) and As(V) retarded the transformation process significantly and caused a complete inhibition at concentrations of 2.25 mM and higher. In the presence of Sb(V), the transformation was again not only affected by retardation. Just like at pH 4, goethite seemed to be favored by Sb(V), but 6.00 mM Sb(V) converted ferrihydrite almost completely to feroxyhyte with traces of hematite (the latter detected only by Raman spectroscopy).

In alkaline conditions (**pH 12**) and absence of foreign ions, ferrihydrite transformed within two days almost completely to goethite with traces of hematite (detected by Raman spectroscopy). No changes in composition were observed until day 16, when the experiment was terminated. These observations are consistent with the results of [3,5,12].

P(V) and As(V) favored hematite formation over goethite, and retarded the transformation process significantly at concentrations of 2.25 mM. At concentrations of 6.00 mM only traces of hematite were detected by Raman spectroscopy. In the presence of Sb(V), ferrihydrite transformed almost undisturbed to goethite. Only at concentrations of 6.00 mM Sb(V) a retarding effect was observed. The dominant

transformation product remained goethite with traces of hematite (detected by Raman spectroscopy).

Raman spectroscopy is a powerful tool for mineral identification [32,33]. Especially for the characterization of trace amounts of iron oxides, Raman spectroscopy is considered a useful and complimentary method for iron oxide identification [34]. For this reason, selected samples were additionally analyzed by Raman spectroscopy. Raman spectra confirm the here presented XRD measurements and complete them with regard to iron oxide species occurring in trace amounts. All Raman results are summarized in Table 1.

Because of the poor crystallinity of feroxyhyte, this phase has been additionally characterized by TEM observations and measurements. Several selected-area electron diffraction (SAED) patterns of single feroxyhyte crystals have been collected (Figure 2). Feroxyhyte forms rhombohedral crystals with a size of 10-30 nm and sharp diffraction spots. Despite of the sensitivity of feroxyhyte to the electron beam and its small size, one crystal has been carefully tilted by up to  $\sim 18^\circ$  along the  $[110]_{fx}$  axis from the  $[1\bar{1}1]_{fx}$  zone to the  $[2\bar{2}1]_{fx}$  zone. These measurements confirm the three dimensional consistency with the feroxyhyte lattice.

#### *Chemical composition of the transformation products (ICP-OES)*

The elemental composition of all 405 runs (shown in Figure 1) is summarized in Figure 3. A direct comparison between the different loadings (P(V), As(V), Sb(V)) is complicated, considering that different anions lead to different ratios amongst the transformation products and retard the transformation with different rates.

At pH 12 and concentrations of up to 0.750 mM, P(V) and As(V) lead to goethite + hematite mixtures, which were free of untransformed ferrihydrite. At 0.750 mM a molar P:Fe and As:Fe ratios of 0.0024 and 0.0068, respectively, was observed. Higher P(V)/As(V) concentrations (2.250-6.000 mM) led to ferrihydrite as the dominant phase, showing significantly higher molar P:Fe and As:Fe ratios of 0.012 and 0.024. In the presence of Sb(V), pure goethite was even formed at concentrations of 2.250 mM. These goethite samples showed molar Sb:Fe ratios of 0.034. At Sb(V) concentrations of 6.000 mM, goethite formed but ferrihydrite remained as the dominant phase until day 16, when the experiment was terminated. The goethite + ferrihydrite mixtures displayed molar Sb:Fe ratios of 0.085.

At pH 7, neither P(V) nor As(V) doped ferrihydrite transformed completely. Samples doped with P(V) revealed a maximum molar P:Fe ratio of 0.028, whereas As(V) doped samples showed a maximum molar As:Fe ratio of 0.060. Ferrihydrite doped with Sb(V), however, displayed a maximum molar Sb:Fe ratio of 0.052 (at 2.25 mM) for the goethite + hematite mixtures and 0.121 (at 6.00 mM) for ferrihydrite.

At pH 4, P(V) and As(V) revealed the highest concentrations in untransformed ferrihydrite (at 6.00 mM) with molar P:Fe and As:Fe ratios of 0.029 and 0.060, respectively. Again, the highest Sb(V) concentrations were found in ferrihydrite with molar Sb:Fe ratios of 0.120. Surprisingly, the goethite + hematite mixtures (formed at 2.25 mM Sb) contained not only less Sb(V) than similar mixtures formed at pH 7, but also less than goethite formed at pH 12.

*Transformations at increasing Sb:Fe ratios*

During the ferrihydrite transformations at pH 4 and 7, an increase in goethite abundance and the formation of feroxyhyte could be observed. In order to investigate these two changes in transformation products and to evaluate the stability of feroxyhyte at even higher Sb:Fe ratios, a second experiment at smaller concentration steps was performed. The conditions 70 °C and 16 days transformation time were kept for all samples. Selected XRD patterns of the experiment are shown in Figure 4.

In the absence of Sb(V) (molar Sb:Fe ratio of 0.000) and pH 4, hematite was the only transformation product. With increasing Sb(V) concentrations, the formation of goethite was indicated by a growing (101) peak at 21.15 °2 $\theta$ . The increase in intensity of the (101)<sub>goe</sub> peak was coupled with an increase of its FWHM, hence, decrease in the crystallinity of goethite. Hematite is also affected by increasing Sb(V) concentrations, showing decreasing intensities and an increasing FWHM of its peaks. However, the peaks ascribed to hematite did not decrease equally in intensity. From the dominant hematite peaks (102), (104), and (024) decreased strongly in intensity, whereas (110), (113), (116), and (300) decreased far less. Simultaneously, the hematite peaks (006) and (226) increased in intensity. The remaining peaks at an molar Sb:Fe ratio of 0.300 correspond well with the feroxyhyte peaks {100}, (002), {101}, {102}, {110}, and {202}.

With further increasing Sb(V) concentrations, the FWHM of the feroxyhyte peaks increased. At molar Sb:Fe ratios of 0.600-1.000, the only crystalline ferrihydrite transformation product was the iron antimonate tripuhyite (FeSbO<sub>4</sub>).

Since both feroxyhyte and tripuhyite are poorly crystalline transformation products, the XRD results were additionally confirmed by Raman spectroscopy. Selected

Raman spectra are shown in Figure 5. Sample pH4Sb6.000 was the product of ferrihydrite transformed at pH 4, 70 °C and Sb(V) concentrations of 6.000 mM, with an aging time of 16 days. The Raman spectrum confirmed feroxyhyte as the only transformation product with impurities of KNO<sub>3</sub> from the ferrihydrite synthesis. Sample pH7Sb6.000 was formed at the same conditions, but pH 7 instead of pH 4. In this case feroxyhyte was accompanied by traces of hematite and again some minor impurities of KNO<sub>3</sub>. At a molar Sb:Fe ratio of 0.600 (sample pH4Sb:Fe0.600), no feroxyhyte was formed but tripuhyte instead. This tripuhyte was poorly crystalline which reduced the quality of the Raman spectrum considerably. In comparison to tripuhyte reference 1, synthesized after [25], only minor similarities could be observed with sample pH4Sb:Fe0.600, which is mainly the band at ~620 cm<sup>-1</sup>. Tripuhyte reference 2, synthesized after [26], was in better agreement with the sample. However, the bands at ~740 cm<sup>-1</sup> and ~500 cm<sup>-1</sup> were not well distinctive, whereas the band at ~420 cm<sup>-1</sup> was missing. Furthermore, both tripuhyte reference compounds were clearly identified by XRD, although the Raman spectra showed only minor similarities between both of them (see Figure 5). It can therefore be concluded that the Raman spectra of feroxyhyte agree well with the XRD results. The Raman spectra of tripuhyte, however, showed considerable differences between the sample (pH4Fe:Sb0.600) and the reference compounds (prepared using two different methods), but also between the reference compounds themselves. The poor crystallinity of the nano-sized tripuhyte in sample pH4Fe:Sb0.600 could lead to phonon-confinement effects, often observed in nano-sized crystallites [35], causing the observed band shifts in the Raman spectrum.

## DISCUSSION

### *Maximum adsorption capacities*

With the measured specific surface area of the transformation products and the necessary surface area for the adsorption of P(V), As(V), and Sb(V) complexes taken from literature, maximum adsorption capacities for a simple adsorption model could be calculated.

The specific surface area of ferrihydrite should be handled with care, because it is highly variable and can fluctuate between 100-700 m<sup>2</sup>/g [11]. Considering that the structure and chemical formula is still under debate [17,36], adsorption calculations for ferrihydrite bear a significant uncertainty. The area required for the adsorption of one phosphate ion to the ferrihydrite surface varies between 0.33-0.62 nm<sup>2</sup> [37,38,39,40] and for arsenate 0.40 nm<sup>2</sup> [41]. These values lead to a calculated maximum adsorption capacity for phosphate and arsenate of 39.27 (5.03 μmol/m<sup>2</sup>) and 78.44 mg/g (4.18 μmol/m<sup>2</sup>), respectively. To our knowledge, no information about the area taken by one antimonate ion at the surface of ferrihydrite is available. For goethite, the reported areas for adsorbed phosphate ion are 0.61-0.66 nm<sup>2</sup> [38,42,43,44], those for an arsenate ion 0.65-1.11 nm<sup>2</sup> [45,46,47] and for an antimonate ion 0.417 nm<sup>2</sup> [48]. These values lead to a maximum adsorption capacity of goethite for P(V) of 2.11 mg/g (2.72 μmol/m<sup>2</sup>), As(V) 4.79 mg/g (2.55 μmol/m<sup>2</sup>), and Sb(V) 12.03 mg/g (3.95 μmol/m<sup>2</sup>). Hematite is more complicated concerning its adsorption capacity as both morphology and grain size are highly dependent on the conditions of its synthesis [11] and therefore adsorption capacity varies [49,50]. The area required for an adsorbed phosphate ion lies between 0.40-0.61 nm<sup>2</sup> [39,49,50,51], for an arsenate ion 0.37 nm<sup>2</sup> [47] and for an antimonate ion 0.780 nm<sup>2</sup> [52]. For hematite, maximum adsorption capacities for P(V) of 3.86 mg/g (4.15



$\mu\text{mol/m}^2$ ), As(V) 10.10 mg/g ( $4.49 \mu\text{mol/m}^2$ ), and Sb(V) 7.78 mg/g ( $2.13 \mu\text{mol/m}^2$ ) are reached. To our knowledge, no comparable information for ferrihydrite is available.

The chemical composition of the transformation products indicates that the P(V) and As(V) contents were all below the calculated maximum adsorption capacities, except for hematite, which contained up to 27.35 mg As/g. For Sb(V), the highest concentrations occurred in ferrihydrite with 142.56 mg Sb/g, followed by goethite with 110.30 mg Sb/g. Unfortunately, no comparable literature values are available about Sb(V) adsorption for both minerals. Goethite contained 44.39 mg Sb/g, significantly more than the calculated maximum adsorption capacity, whereas pure hematite was only present in low Sb(V) environment, remaining below the calculated adsorption capacity with 7.01 mg Sb/g.

Considering the calculated maximum adsorption capacities it can be summarized that Sb(V) loadings in the goethite samples are considerably higher than expected from a simple adsorption system. One could therefore speculate that Sb(V) is not only adsorbed to the surface of the goethite crystals but incorporated into their structure.

The validity of these calculated maximum adsorption capacities must be considered as a rough approximation. This model assumes a complete mononuclear, monodentate coverage of the whole specific surface area, not taking reactive adsorption sites, crystal morphology or shielding of other ions into account. Furthermore, the adsorption to ferrihydrite, yet without a widely accepted crystal structure and chemical composition, is still poorly understood. The aggregates formed by ferrihydrite and the size of the single particles may have a significant impact on the adsorption behavior and therefore on the adsorption capacity. Hematite, on the other hand, has a well-defined crystal structure and chemical

composition, however, the size of the crystallites and their habitus strongly depends on the conditions of their formation. For these two phases it is therefore questionable, if adsorption densities from literature are sufficient for the calculation of maximum adsorption capacities. Adsorption capacities calculated from literature values are summarized graphically in Figure 6.

### *Feroxyhyte or hematite*

At increasing Sb(V) concentrations, the XRD patterns showed an apparent transition between hematite ( $\alpha$ -Fe<sub>2</sub>O<sub>3</sub>) and feroxyhyte ( $\delta'$ -FeOOH). The six indicative peaks of feroxyhyte (100), (002), (011/101), (012/102), (110), and (022/202) which can be seen in the powder XRD patterns, share the same  $2\theta$  positions as the hematite peaks (110), (113), (116), (300), (006) and (226), respectively. A problem arises when hematite and feroxyhyte coexist, because the powder XRD pattern is a linear combination of the patterns of both minerals, with a complete overlap of the feroxyhyte peaks with hematite peaks.

Therefore, all electron diffraction patterns of feroxyhyte were additionally cross-checked for indexing with a hematite (space group R $\bar{3}c$ ) model. The results show that the lattice of feroxyhyte coincides completely with the lattice of hematite. All feroxyhyte indices can therefore be converted to hematite indices by a transformation of the lattice basis. The relation of both lattices is given by the following transformation matrix:

$$(1) \quad \bar{h}_{\text{hem}} = \bar{h}_{\text{fx}} \cdot \mathbf{P} \quad \text{with } \mathbf{P} = \begin{pmatrix} 1 & 1 & 0 \\ \bar{1} & 2 & 0 \\ 0 & 0 & 3 \end{pmatrix};$$

The unit cell volume of hematite is 9-times larger than that of feroxyhyte. Hence, several reflections of hematite should be extinct for feroxyhyte. Due to the 3-times

larger  $c$  axis of hematite, only hematite reflections with  $l = 3n$  are present for feroxyhyte. In addition the  $c$ -glide plane of hematite causes a further extinction rule for hematite of  $l = 6n$  for  $(00l)$ , which is not valid for feroxyhyte. Therefore, only these extinction rules provide an unambiguous possibility for the recognition of feroxyhyte. All reflections of powder electron diffraction patterns show exclusively only  $d$ -spacings characteristic for feroxyhyte, and also electron diffraction pattern along  $[010]_{\text{fx}}$  zone clearly violates the extinction of  $l = 6n$  for hematite (see Figure 2). The diffraction spot  $(003)_{\text{hem}}$  is weak but clearly present and could not be an effect of double diffraction. During tilting of the crystal from  $[301]_{\text{hem}}$  zone to the  $[601]_{\text{hem}}$  zone, which corresponds to  $[1\bar{1}1]_{\text{fx}}$  and  $[2\bar{2}1]_{\text{fx}}$  of feroxyhyte, a zone axis of  $[401]_{\text{hem}}$  should be clearly visible in case of hematite, because it contains the  $(10\bar{4})$  diffraction spot, one of the strongest reflections of hematite. The absence of this additional zone axis provides a further evidence for the presence of feroxyhyte (Figure 7).

The atomic structure of hematite is characterized by hexagonally close packed layers of oxygen, in which  $2/3$  of the octahedral sites are filled by ferric iron in an ordered matter. In contrast, the unit cell of feroxyhyte corresponds to a primitive cell setting of a close packed oxygen arrangement, which does not allow an ordered occupancy of any of the octahedral sites. Therefore, feroxyhyte (after the model of [53]) can be considered as completely disordered hematite, which of course, contains some (OH) groups for charge balance. Whether the OH groups are disordered, like in the structural model of feroxyhyte of [53] or ordered into basal layers like in the  $\text{Fe}(\text{OH})_2$ -structure type [11,54] is still poorly understood.

The formation of feroxyhyte occurs in this study only at certain, relatively high Sb(V) concentrations. The necessity of higher Sb(V) concentrations together with the rapid formation of feroxyhyte indicates a nucleation/crystallization from bulk solution, rather

than a solid state formation of feroxyhyte from hematite by cation disorder. This is supported by considering that Sb-doped hematite remains stable for more than 16 days at 70 °C in aqueous solution without any signs of a transformation to feroxyhyte. The observed apparent transition between hematite and feroxyhyte in the XRD patterns is therefore considered as a decreasing hematite signal at increasing Sb(V) concentrations, combined with an increasing feroxyhyte signal and not as a solid state transformation.

*Adsorption or structural incorporation of P(V), As(V), and Sb(V)*

During the transformation experiments, P(V) and As(V) have shown a similar behavior, consistent with the existing literature [8,9]. The formation of hematite was favored over goethite, and at high concentrations of both anions the transformation was retarded or completely inhibited. Except for the As(V) adsorption to hematite, the P(V) and As(V) concentrations in the solid transformation product stayed below the calculated adsorption capacities, in agreement with previous adsorption studies [37,38,39,40,41,42,43,44,45,46,47,48,49,50,51].

Transformations in the presence of Sb(V), however, differed strongly from those with P(V) and As(V). During the transformation experiments with Sb(V), goethite was favored instead of hematite. At higher Sb(V) concentrations, feroxyhyte replaced goethite and hematite. Additionally, the solid transformation products feroxyhyte and goethite showed extraordinary high concentrations of Sb(V).

Since most studies deal with the adsorption of contaminants to the surface of the iron oxides rather than with their structural incorporation, the possibility of a pure adsorption system should be examined. P(V), As(V), and Sb(V) occur in aqueous solution typically as anionic complexes. Between pH 4-12 three different, pH dependent species of P(V) and As(V) can be distinguished. At pH 4, the dominant

specie is  $\text{H}_2(\text{P,As})\text{O}_4^-$ , at pH 7  $\text{H}(\text{P,As})\text{O}_4^{2-}$ , and at pH 12  $(\text{P,As})\text{O}_4^{3-}$ . For Sb(V) only one dominant specie,  $\text{Sb}(\text{OH})_6^-$ , can be observed over the whole pH range of 4-12 [19,55,56]. In order to attract and therefore adsorb an anionic complex, positively charged surface is needed, thus, the pH of the solution must be lower than the point of zero charge (PZC) of the mineral. Feroxyhyte, formed at pH 4 and 7 has a PZC of about 7.5-8 [57,58]. This means that feroxyhyte, under certain conditions, is close to the point of zero charge, but anionic complexes are already attracted by the surface and adsorption is possible. In the conducted experiments, feroxyhyte showed molar Sb:Fe ratios of up to 0.12 (145 mg Sb/g). Can a pure adsorption system explain such high concentrations sufficiently? Unfortunately, no adsorption capacities are available for feroxyhyte in literature. Under the assumption that one surface Fe-octahedron on the feroxyhyte surface exposes an area of  $0.149 \text{ nm}^2$ , like at the goethite (001) face, and a mononuclear monodentate binding of the Sb-octahedra, a maximum of 127 mg Sb/g can be adsorbed to the feroxyhyte surface, which is less than in the feroxyhyte samples. This calculation is based on the specific surface area of the feroxyhyte samples and the chemical surface properties of goethite. Since the feroxyhyte structure is still under debate [59,60] and the occupancy of Fe on the octahedral sites is unclear, the goethite model was considered as a better basis for a rough estimation.

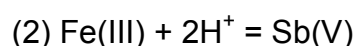
Goethite, on the other hand, which was formed in the experiments at pH 12 showed molar Sb:Fe ratios of 0.03 (44 mg Sb/g). Considering that the adsorption capacity for goethite calculated after [48] is about 12 mg Sb/g, a pure adsorption system is again unlikely. Additionally the PZC for goethite is around 7.2-9.0 [61,62,63,64,65], which means that at pH 12 the surface of goethite is negatively charged and repels anionic complexes like  $\text{Sb}(\text{OH})_6^-$ . These findings suggest that other or additional mechanisms than pure adsorption are taking place during the transformation experiments in the

presence of Sb(V), most likely incorporation but surface precipitation cannot be excluded.

*A possible model for the observed findings*

High concentration of Sb(V) in some of the runs can be explained by adsorption, surface precipitation, or incorporation. As discussed above, the adsorption capacities are not sufficient, especially in the case of goethite and feroxyhyte. Surface precipitation is possible, but no evidence for additional phases could be detected by Raman spectroscopy. Therefore, incorporation of Sb(V) into the structures of goethite and feroxyhyte seems to be the most viable explanation for the presented observations.

Sb(V) is usually coordinated octahedrally in the field of oxygen anions. The ionic radius of Sb(V) is 0.60 Å, very similar to that of 0.55 Å of Fe(III) [66]. In terms of ionic radii, the substitution of Sb(V) for Fe(III) should be easy. Of course, such heterovalent substitution must be coupled with the exchange of other ions. One possibility is the loss of hydrogen concomitant with this substitution:



Such mechanism could operate in the oxyhydroxides such as goethite or feroxyhyte. Here, the loss of some of the H atoms may not be substantial to the preservation of the entire structure.

First the structure of goethite will be considered. Goethite is constructed by [001] double octahedral chains (in the Pbnm setting) (Figure 8). The octahedral units in the structure of goethite has the composition Fe(III)O<sub>3</sub>(OH)<sub>3</sub>. The H atoms occupy positions in the tunnels between the double chains. The Fe(III)-Sb(V) substitution would change the composition of the octahedra to Sb(V)O<sub>5</sub>(OH) and leave two H

positions in the tunnels vacant. The crystal structure of goethite could probably tolerate a certain degree of Sb(V) substitution but would probably collapse if a significant portion of the tunnels should remain empty. This mechanism could operate in goethite and account for the Sb(V) incorporation, based on the following crystal chemical arguments.

The collapse of the tunnels between the double chains in goethite leads to a denser structure with single octahedral chains. Such structure belongs to the high-pressure polymorph  $\epsilon$ -FeOOH [67,68] (Figure 8). This phase is isostructural with rutile. Interestingly, tripuhyite, FeSbO<sub>4</sub>, has also a rutile-type structure [69] (Figure 8). Hence, the Fe(III)-Sb(V) substitution in goethite leads to a withdrawal of H atoms, collapse of the tunnels, and a gradual conversion of goethite to tripuhyite on the atomic scale. This transformation from double- to single chains can also account for the here presented observation that the crystallinity of goethite worsens with increasing Sb load.

In hematite, coupling of the Fe(III)-Sb(V) with H loss is limited or excluded. Structures derived from that of hematite are capable of incorporating pentavalent cations. The best example is LiNbO<sub>3</sub>, a superstructure of the hematite structure (Figure 9), with the substitution  $2\text{Fe(III)} = \text{Li}^+ + \text{Nb(V)}$ . The cations in LiNbO<sub>3</sub> are ordered in a way to avoid the presence of two Nb(V) ions in two face-sharing octahedra because such arrangement would lead to a strong electrostatic repulsion. By analogy, if forcing Sb(V) into the structure of hematite, the Fe(III)-Sb(V) repulsion in two neighboring face-sharing octahedra would be too strong. The substitution  $2\text{Fe(III)} = \text{H}^+ + \text{Sb(V)}$  seems to be implausible.

The only way to store a larger amount of Sb(V) in a hematite-related structure is to disorder the cations such that there are octahedra which do not share a face with

other octahedra. Such octahedra could be then occupied by Sb(V). The disordered variant of the hematite structure is feroxyhyte,  $\delta'$ -FeOOH, a phase observed in a number of runs.

### **Concluding remarks**

The presence of tripuhyte in antimony mine tailings was already reported in previous works [70,71], however, not the presence of feroxyhyte. One possible reason for this is the poor crystallinity as well as the small crystal size of feroxyhyte and the fact, that the XRD peaks of hematite and feroxyhyte overlap completely. Feroxyhyte could be erroneously identified as poorly crystalline hematite or hematite could mask the presence of feroxyhyte.

### **ACKNOWLEDGEMENTS**

We would like to thank Hannes Herzel for his help during the iron oxide syntheses. Thanks to Dirk Merten, Ines Kamp, Maria Wierzbicka-Wieczorek and Arkadiusz Wieczorek for their help with ICP-OES, XRD, and SEM, as well as Anna Schmidt and Beate Truckenbrodt (all Jena) for BET measurements. Additionally we want to thank the two anonymous reviewers for their comments and suggestions and the editor for editorial handling. This research was funded by the Deutsche Forschungsgemeinschaft (DFG) Research Training Group GRK 1257/1.



## REFERENCES

- [1] Ackermann, S., Gieré, R., Newville, M., and Majzlan, J. (2009) Antimony sinks in the weathering crust of bullets from Swiss shooting ranges. *Science of the Total Environment*, **407**, 1669 – 1682.
- [2] Loan, M., Parkinson, G.M., and Richmond, W.R. (2005) The effect of zinc sulfide on phase transformations of ferrihydrite. *American Mineralogist*, **90**, 258-261.
- [3] Cudennec, Y. and Lecerf, A. (2006) The transformation of ferrihydrite into goethite or hematite, revisited. *Journal of Solid State Chemistry*, **179**, 716-722.
- [4] Cornell, R.M., Giovanoli, R., and Schindler, P.W. (1987) Effect of silicate species on the transformation of ferrihydrite into goethite and hematite in alkaline media. *Clays and Clay Minerals*, **35**, 1, 21-28.
- [5] Nagano, T., Nakashima, S., Nakayama, S., and Senoo, M. (1994) The use of color to quantify the effect of pH and temperature on the crystallization kinetics of goethite under highly alkaline conditions. *Clay and Clay Minerals*, **42**, 2, 226-234.
- [6] Paige, C.R., Snodgrass, W.J., Nicholson, R.V., and Scharer, J.M. (1996) The crystallization of arsenate-contaminated iron hydroxide solids at high pH. *Water Environment Research*, **68**, 6, 981-987.
- [7] Paige, C.R., Snodgrass, W.J., Nicholson, R.V., Scharer, J.M., and He, Q.H. (1997) The effect of phosphate on the transformation of ferrihydrite into crystalline products in alkaline media. *Water, Air, and Soil Pollution*, **97**, 397-412.
- [8] Shaw, S., Pepper, S.E., Bryan, N.D., and Livens, F.R. (2005) The kinetics and mechanisms of goethite and hematite crystallization under alkaline conditions, and in the presence of phosphate. *American Mineralogist*, **90**, 1852-1860.
- [9] Das, S., Hendry, J., and Essilfie-Dughan, J. (2011a) Effects of adsorbed arsenate on the rate of transformation of 2-line ferrihydrite at pH 10. *Environmental Science and Technology*, **45**, 5557-5563.
- [10] Das, S., Hendry, J., and Essilfie-Dughan, J. (2011b) Transformation of two-line ferrihydrite to goethite and hematite as a function of pH and temperature. *Environmental Science and Technology*, **45**, 268-275.
- [11] Cornell, R.M. and Schwertmann, U. (2003) *The iron oxides, properties, reactions, occurrences, and uses*. Wiley-VCH Verlag, Weinheim.
- [12] Schwertmann, U. and Murad, E. (1983) Effect of pH on the formation of goethite and hematite from ferrihydrite. *Clays and Clay Minerals*, **31**, 4, 277-284.
- [13] Blesa, M.A. and Matijevic, E. (1989) Phase-transformations of iron-oxides, oxyhydroxides, and hydrous oxides in aqueous-media. *Advances in Colloid and Interface Science*, **29**, 3-4, 173-221.
- [14] Johnston, J.H. and Lewis, D.G. (1983) A detailed study of the transformation of ferrihydrite to hematite in an aqueous medium at 92°C. *Geochimica et Cosmochimica Acta*, **47**, 11, 1823-1831.
- [15] Schwertmann, U. and Fischer, W.R. (1966) Zur Bildung von  $\alpha$ -FeOOH und  $\alpha$ -Fe<sub>2</sub>O<sub>3</sub> aus amorphem Eisen(III)-hydroxid III. *Zeitschrift für Anorganische und Allgemeine Chemie*, **346**, 137-142.
- [16] Fischer, W.R. and Schwertmann, U. (1975) The formation of hematite from amorphous iron(III)hydroxide. *Clays and Clay Minerals*, **23**, 33-37.
- [17] Jambor, J.L. and Dutrizac, J.E. (1998) Occurrence and constitution of natural and synthetic ferrihydrite, a widespread iron oxyhydroxide. *Chemical Review*, **98**, 2549-2585.

- 
- [18] Guan, X., Dong, H., Ma, J., and Jiang, L. (2009) Removal of arsenic from water: Effects of competing anions on As(III) removal in  $\text{KMnO}_4$ -Fe(II) process. *Water Research*, **43**, 15, 3891-3899.
- [19] Filella, M., Belzile, N., and Chen, Y-W. (2002) Antimony in the environment: a review focused on natural waters - II. Relevant solution chemistry. *Earth-Science Reviews*, **59**, 265-285.
- [20] Majzlan, J. (2011) Thermodynamic stabilization of hydrous ferric oxide by adsorption of phosphate and arsenate. *Environmental Science and Technology*, **45**, 4726-4732.
- [21] He, Q.H., Leppard, G.G., Paige, C.R., and Snodgrass, W.J. (1996) Transmission electron microscopy of a phosphate effect on the colloid structure of iron hydroxide. *Water Research*, **30**, 6, 1345-1352.
- [22] Schwertmann, U. and Cornell, R.M. (2000) Iron oxides in the laboratory: Preparation and Characterization, 2nd edition. Wiley-VCH Verlag, Weinheim.
- [23] Álvarez-Benedí, J., Bolado, S., Cancillo, I., Calvo, C., and García-Sinovas, D. (2005) Adsorption-desorption of arsenate in three Spanish soils. *Vadose Zone Journal*, **4**, 2, 282-290.
- [24] Tighe, M., Lockwood P., and Wilson, S. (2005) Adsorption of antimony(V) by floodplain soils, amorphous iron(III) hydroxide and humic acid. *Journal of Environmental Monitoring*, **7**, 1177-1185.
- [25] Diemar, G.A., Filella, M., Leverett, P., and Williams, P.A. (2009) Dispersion of antimony from oxidizing ore deposits. *Pure and Applied Chemistry*, **81**, 9, 1547-1553.
- [26] Martinelli, A., Ferretti, M., Basso, R., Cabella, R., Lucchetti, G., Marescotti, P., and Buscaglia, V. (2004) Solid state miscibility in the pseudo-binary  $\text{TiO}_2$ - $(\text{FeSb})\text{O}_4$  system at 1373 K. *Zeitschrift für Kristallographie*, **219**, 487-493.
- [27] Wojdyr, M. (2010) Fityk: a general-purpose peak fitting program. *Journal of Applied Crystallography*, **43**, 1126-1128. (reprint)
- [28] Brunauer, S., Emmett, P.H., and Teller, E. (1938) Adsorption of gases in multimolecular layers. *Journal of the American Chemical Society*, **60**, 308-319.
- [29] Hansen, H.C.B., Raben-Lange, R., Raulund-Rasmussen, K., and Borggaard, O.K. (1994) Monosilicate adsorption by ferrihydrite and goethite at pH 3-6. *Soil Science*, **158**, 40-46.
- [30] Larsen, O. and Postma, D. (2001) Kinetics of reductive bulk dissolution of lepidocrocite, ferrihydrite, and goethite. *Geochimica et Cosmochimica Acta*, **65**, 1367-1379.
- [31] Carlson, L. and Schwertmann, U. (1980) Natural occurrence of feroxyhyte ( $\delta'$ - $\text{FeOOH}$ ). *Clays and Clay Minerals*, **28**, 4, 272-280.
- [32] Dörfer, T., Schumacher, W., Tarcea, N., Schmitt, M., and Popp, J. (2010) Quantitative mineral analysis using Raman spectroscopy and chemometric techniques. *Journal of Raman Spectroscopy* **41**, 684-689.
- [33] Ciobotă, V., Salama, W., Tarcea, N., Rösch, P., Aref, M.E., Gaupp, R., and Popp, J. (2012) Identification of minerals and organic materials in Middle Eocene ironstones from the Bahariya Depression in the Western Desert of Egypt by means of micro-Raman spectroscopy. *Journal of Raman Spectroscopy* **43**, 405-410.
- [34] Hanesch, M. (2009) Raman spectroscopy of iron oxides and (oxy)hydroxides at low laser power and possible applications in environmental magnetic studies. *Geophysical Journal International*, **177**, 3, 941-948.

- [35] Georgescu, D., Baia, L., Ersen, O., Baia, M., and Simon, S. (2012) Experimental assessment of the phonon confinement in TiO<sub>2</sub> anatase nanocrystallites by Raman spectroscopy. *Journal of Raman Spectroscopy*, **43**, 7, 876-883.
- [36] Michel, M.F., Ehm, L., Antao, S.M., Lee, P.L., Chupas, P.J., Liu, G., Strongin, D.R., Schoonen, M.A.A., Phillips, B.L., and Parise, J.B. (2007) The structure of ferrihydrite, a nanocrystalline material. *Science*, **316**, 5832, 1726-1729.
- [37] Ryden, J.C., McLaughlin, J.R., and Syers, J.K. (1977) Mechanisms of phosphate sorption by soil and hydrous ferric oxide gel. *Journal of Soil Science*, **28**, 72-92.
- [38] Borggaard, O.K., Raben-Lange, B., Gimsing, A.L., and Strobel, B.W. (2005) Influence of humic substances on phosphate adsorption by aluminium and iron oxides. *Geoderma*, **127**, 270-279.
- [39] Gimsing, A.L. and Borggaard, O.K. (2007) Phosphate and glyphosate adsorption by hematite and ferrihydrite and comparison with other variable-charge minerals. *Clays and Clay Minerals*, **55**, 1, 108-114.
- [40] Arai, Y. and Sparks, D.L. (2001) ATR-FTIR Spectroscopic investigation on phosphate adsorption mechanisms at the ferrihydrite-water interface. *Journal of Colloid and Interface Science*, **241**, 317-326.
- [41] Zhu, J., Pigna, M., Cozzolino, V., Caporale, A.G., and Violante, A. (2011) Sorption of arsenite and arsenate on ferrihydrite: Effect of organic and inorganic ligands. *Journal of Hazardous Materials*, **189**, 564-571.
- [42] Atkinson, R.J., Quirk, J.P., and Posner, A.M. (1972) Kinetics of isotropic-exchange of phosphate at alpha-FeOOH-aqueous solution interface. *Journal of Inorganic and Nuclear Chemistry*, **34**, 7, 2201-2211.
- [43] Barrow, N.J., Madrid, L., and Posner, A.M. (1981) A partial model for the rate of adsorption and desorption of phosphate by goethite. *Journal of Soil Science*, **32**, 3, 399-407.
- [44] Torrent, J., Barrón, V., and Schwertmann, U. (1990) Phosphate adsorption and desorption by goethites differing in crystal morphology. *Soil Science Society of America Journal*, **54**, 4, 1007-1012.
- [45] Salazar-Camacho, C. and Villalobos, M. (2010) Goethite surface reactivity: III. Unifying arsenate adsorption behavior through a variable crystal face – Site density model. *Geochemica et Cosmochimica Acta*, **74**, 2257-2280.
- [46] Wainippee, W., Weiss, D.J., Sephton, M.A., Coles, B.J., Unsworth, C., and Court, R. (2010) The effect of crude oil on arsenate adsorption on goethite. *Water Research*, **44**, 5673-5683.
- [47] Mamindy-Pajany, Y., Hurel, C., Marmier, N., and Roméo, M. (2011) Arsenic (V) adsorption from aqueous solution onto goethite, hematite, magnetite and zero-valent iron: Effects of pH, concentration and reversibility. *Desalination*, **281**, 93-99.
- [48] Leuz, A-K., Mönch, H., and Johnson, C.A. (2006) Sorption of Sb(III) and Sb(V) to goethite: Influence on Sb(III) oxidation and mobilization. *Environmental Science and Technology*, **40**, 7277-7282.
- [49] Barron, V., Herruzo, M., and Torrent, J. (1988) Phosphate adsorption by aluminous hematite of different shapes. *Soil Science Society of America Journal*, **52**, 3, 647-651.
- [50] Torrent, J., Schwertmann, U., and Barrón, V. (1994) Phosphate sorption by natural hematites. *European Journal of Soil Science*, **45**, 45-51.

- [501] Colombo, C., Barrón, V., and Torrent, J. (1994) Phosphate adsorption and desorption in relation to morphology and crystal properties of synthetic hematites. *Geochimica et Cosmochimica Acta*, **58**, 4, 1261-1269.
- [52] Ambe, S. (1987) Adsorption kinetics of antimony(V) ions onto  $\alpha$ -Fe<sub>2</sub>O<sub>3</sub> surfaces from an aqueous solution. *Langmuir*, **3**, 4, 489-493.
- [53] Patrat, G., de Bergevin, F., Pernet, M., and Joubert, J. (1983) Structure locale de delta-Fe O O H. *Acta Crystallographica B*, **39**, 165-170.
- [54] Parise, J.B., Marshall, W.G., Smith, R.I., Lutz, H.D., and Moller, H. (2000) The nuclear and magnetic structure of "white rust"-Fe(OH<sub>0.86</sub>D<sub>0.14</sub>)<sub>2</sub>. *American Mineralogist*, **85**, 189-193
- [55] Brintzinger, H. (1948) Die Antimonat-, Antimonit-, Germanat-und Aluminat-loden im gelösten Zustand. *Zeitschrift für Anorganische und Allgemeine Chemie*, **256**, 98-102.
- [56] Pitman, A.L., Pourbaix, M., and de Zoubov, N. (1957) Potential-pH diagram of the antimony– water system. Its applications to properties of the metal, its compounds, its corrosion, and antimony electrodes. *Journal of the Electrochemical Society*, **104**, 594-600.
- [57] Borggaard, O.K. (1983) Effect of surface-area and mineralogy of iron-oxides on their surface-charge and anion-adsorption properties. *Clays and Clay Minerals*, **31**, 3, 230-232.
- [58] Parida, K.M., Gorai, B., Das, N.N., and Rao, S. B. (1997) Studies on ferric oxide hydroxides. III. Adsorption of selenite (SeO<sub>3</sub><sup>2-</sup>) on different forms of iron oxyhydroxides, *Journal of Colloid and Interface Science*, **185**, 355-362.
- [59] Drits, V.A., Sakharov, B.A., and Manceau, A. (1993) Structure of feroxyhyte as determined by simulation of X-ray diffraction curves. *Clay Minerals*, **28**, 2, 209-222.
- [60] Manceau, A. and Drits, V.A. (1993) Local-structure of ferrihydrite and feroxyhyte by EXAFS spectroscopy. *Clay Minerals*, **28**, 2, 165-184.
- [61] Atkinson, R.J., Posner, A.M., and Quirk, J.P. (1967) Adsorption of potential-determining ions at the ferric oxide-aqueous electrolyte interface. *The Journal of Physical Chemistry*, **71**, 3, 550-558.
- [62] Borggaard, O.K. (1983) Effect of surface-area and mineralogy of iron-oxides on their surface-charge and anion-adsorption properties. *Clays and Clay Minerals*, **31**, 3, 230-232.
- [63] Gaboriaud, F. and Ehrhardt, J-J. (2003) Effects of different crystal faces on the surface charge of colloidal goethite ( $\alpha$ -FeOOH) particles: an experimental and modeling study. *Geochimica et Cosmochimica Acta*, **67**, 5, 967-983.
- [64] Walsch, J. and Dultz, S. (2010) Effects of pH, Ca- and SO<sub>4</sub>-concentration on surface charge and colloidal stability of goethite and hematite – consequences for the adsorption of anionic organic substances. *Clay Minerals*, **45**, 1, 1-13.
- [65] Cristiano, E., Hu, Y-J., Siegfried, M., Kaplan, D., and Nitsche, H. (2011) A comparison of point of zero charge measurements methodology. *Clays and Clay Minerals*, **59**, 2, 107-115.
- [66] Shannon, R.D. (1976) Revised effective ionic radii and systematic studies of interatomic distances in halides and chalcogenides. *Acta Crystallographica A*, **32**, 751-767.
- [67] Pernet, M., Joubert, J.C., and Berthet-Colominas, C. (1975) Etude par diffraction neutronique de la forme haute pression de FeOOH. *Solid State Communications*, **17**, 1505-1510.
- [68] Suzuki, A. (2010) High-pressure X-ray diffraction study of  $\epsilon$ -FeOOH. *Physics and Chemistry of Minerals*, **37**, 153-157.

- [69] Berlepsch, P., Armbruster, T., and Brugger, J. (2003) Tripuhyite,  $\text{FeSbO}_4$ , revisited. *Mineralogical Magazine*, **67**, 1, 31-46.
- [70] Majzlan, J., Lalinska, B., Chovan, M., Bläss, U., Brecht, B., Göttlicher, J., Steininger, R., Hug, K., Ziegler, S., and Gescher, J. (2011) A mineralogical, geochemical, and microbiological assessment of the antimony- and arsenic-rich neutral mine drainage tailings near Pezinok, Slovakia. *American Mineralogist*, **96**, 1, 1-13.
- [71] Mitsunobu, S., Takahashi, Y., Utsunomiya, S., Marcus, M.A., Terada, Y., Iwamura, T., and Sakata, M. (2011) Identification and characterization of nanosized tripuhyite in soil near Sb mine tailings. *American Mineralogist*, **96**, 7, 1171-1181.

## FIGURE CAPTIONS

Figure 1: Iron oxide speciation and quantification for P, As, and Sb-doped ferrihydrite and subsequently formed transformation products.

Figure 2: Bright field TEM image and corresponding selected area electron diffraction pattern (inset) of that area showing the rhombohedral shape and the sharp diffraction spots of feroxyhyte.

Figure 3: Chemical composition of the transformation products given as molar ratios of P, As, and Sb against Fe. The molar starting ratios of P/As/Sb : Fe are given for each concentration step.

Figure 4: Ferrihydrite transformation in the presence of increasing Sb(V)-concentrations. The numbers in front of each pattern indicate the molar Sb:Fe ratio. hem: hematite, goe: goethite, fx: feroxyhyte, tri: tripuhyite. All experiments were performed at pH 4 and an aging time of 16 days.

Figure 5: Selected Raman spectra of ferrihydrite transformations at increased Sb(V) concentrations. Sample 1 was transformed at pH 4, 70 °C and Sb(V) concentrations of 6.000 mM with a aging time of 16 days. Sample 2 was transformed at the same conditions, but pH 7 instead of pH 4. Sample 3 was transformed at an molar Sb:Fe ratio of 0.600 at pH 4, 70 °C and 16 days of aging.

Figure 6: Graphical summary of the maximum adsorption capacities calculated from different literature values. The striped bars show the adsorption capacity that can be reached by every cited literature value. The grey bars indicate the uncertainty for the maximum adsorption capacity calculated from literature values. Dots indicate that only one literature value was available. fh: ferrihydrite, hem: hematite, goe: goethite.

Figure 7: Selected electron diffraction pattern of feroxyhyte. The powder pattern shows the four dominant diffraction lines of feroxyhyte, whereas additional lines of hematite are clearly absent. In [010] zone pattern, the (001) reflection of feroxyhyte is clearly visible but should be extinct for hematite.  $[1\bar{1}1]$  and  $[2\bar{2}1]$  zone pattern belong to the same crystal tilted by  $\sim 18^\circ$  along the  $[110]$  axis.

Figure 8: On the left side the structure of goethite ( $\alpha$ -FeOOH) constructed by double octahedral chains (Pbnm setting). In a high pressure environment the tunnels which run parallel to the octahedral chains collapse forming the denser high pressure phase  $\varepsilon$ -FeOOH (upper right). During the Sb(V)  $\rightarrow$  Fe(III) substitution these tunnels could also collapse forming the denser tripuhyite structure (lower right). Both,  $\varepsilon$ -FeOOH and tripuhyite are isostructural with rutile.

Figure 9: Structures similar to that of hematite (left) can incorporate pentavalent ions. These pentavalent ions cannot occur in close contact to each other because of the strong electrostatic repulsion. In LiNbO<sub>3</sub>, a superstructure of hematite, the presence of Nb(V) face-sharing octahedra is avoided by monovalent Li<sup>+</sup> octahedra in between, reducing the electrostatic repulsion.

Table 1: Iron oxide speciation by Raman spectroscopy from selected ferrihydrite transformation products. fh: ferrihydrite, goe: goethite, hem: hematite, and fx: feroxyhyte. The asterisk marks component occurring in trace amounts which were not detected by XRD.

additive	concentration	pH4	pH7	pH12
P <sup>5+</sup>	high (6. mM)	fh/hem*	fh	fh/hem*
	low (0.75 mM)	fh/hem	fh/hem	goe/hem
	free (0 mM)	hem	goe/hem	goe/hem*
As <sup>5+</sup>	high (6 mM)	fh/hem*	fh	fh/hem*
	low (0.75 mM)	fh/hem	fh/goe/hem	goe/hem
	free (0 mM)	hem	goe/hem	goe/hem*
Sb <sup>5+</sup>	high (6 mM)	fx	fx/hem*	fh/goe/hem*
	low (0.75 mM)	goe/hem	goe/hem	goe
	free (0 mM)	hem	goe/hem	goe/hem*

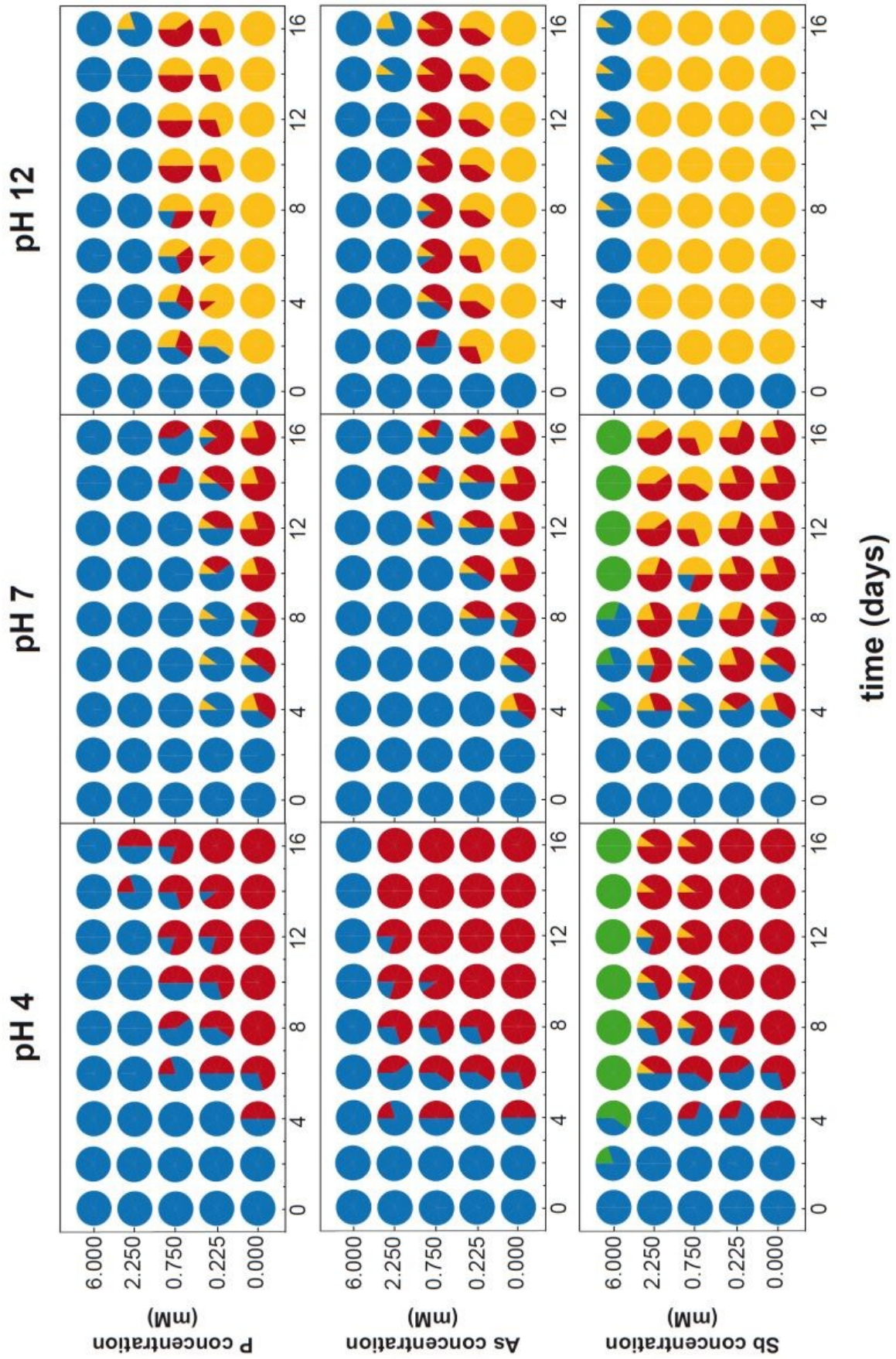


Figure 1: Iron oxide speciation and quantification for P, As, and Sb-doped ferrihydrite and subsequently formed transformation products.

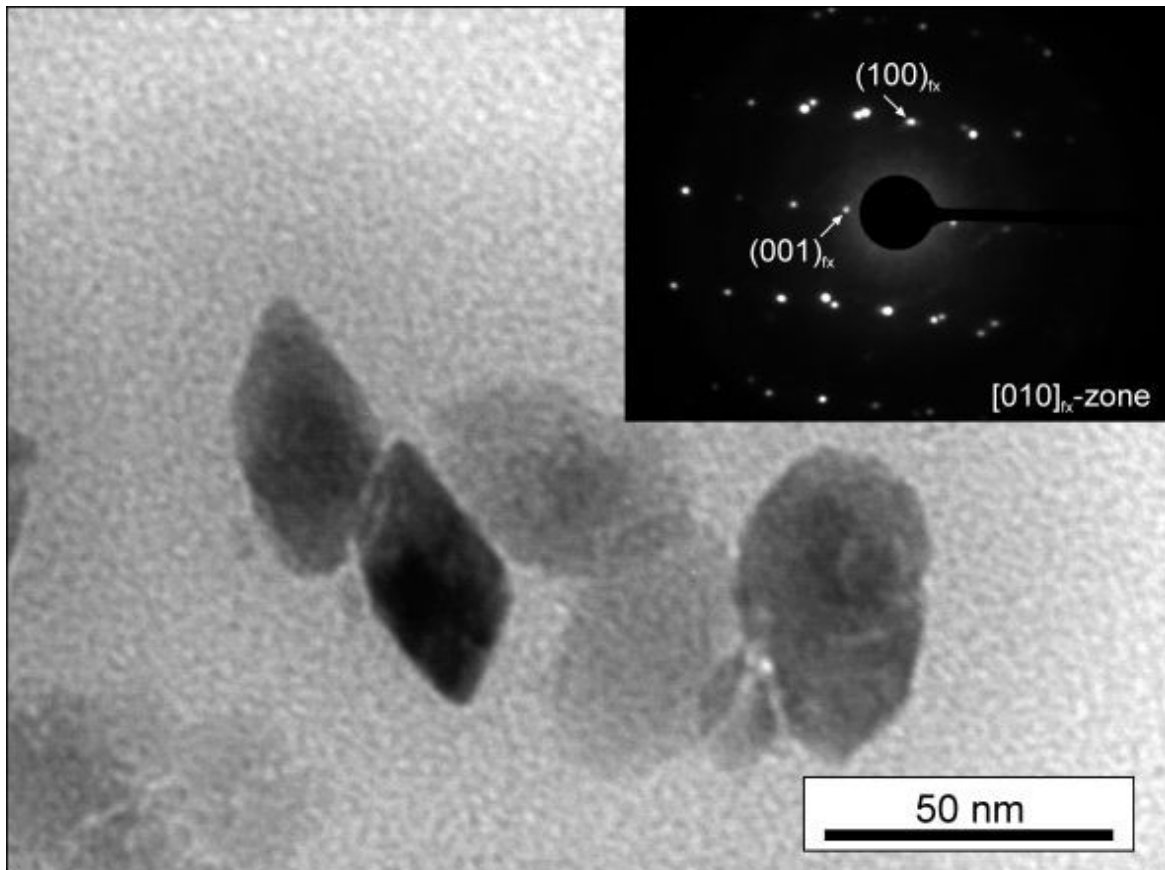


Figure 2: Bright field TEM image and corresponding selected area electron diffraction pattern (inset) of that area showing the rhombohedral shape and the sharp diffraction spots of feroxyhyte.



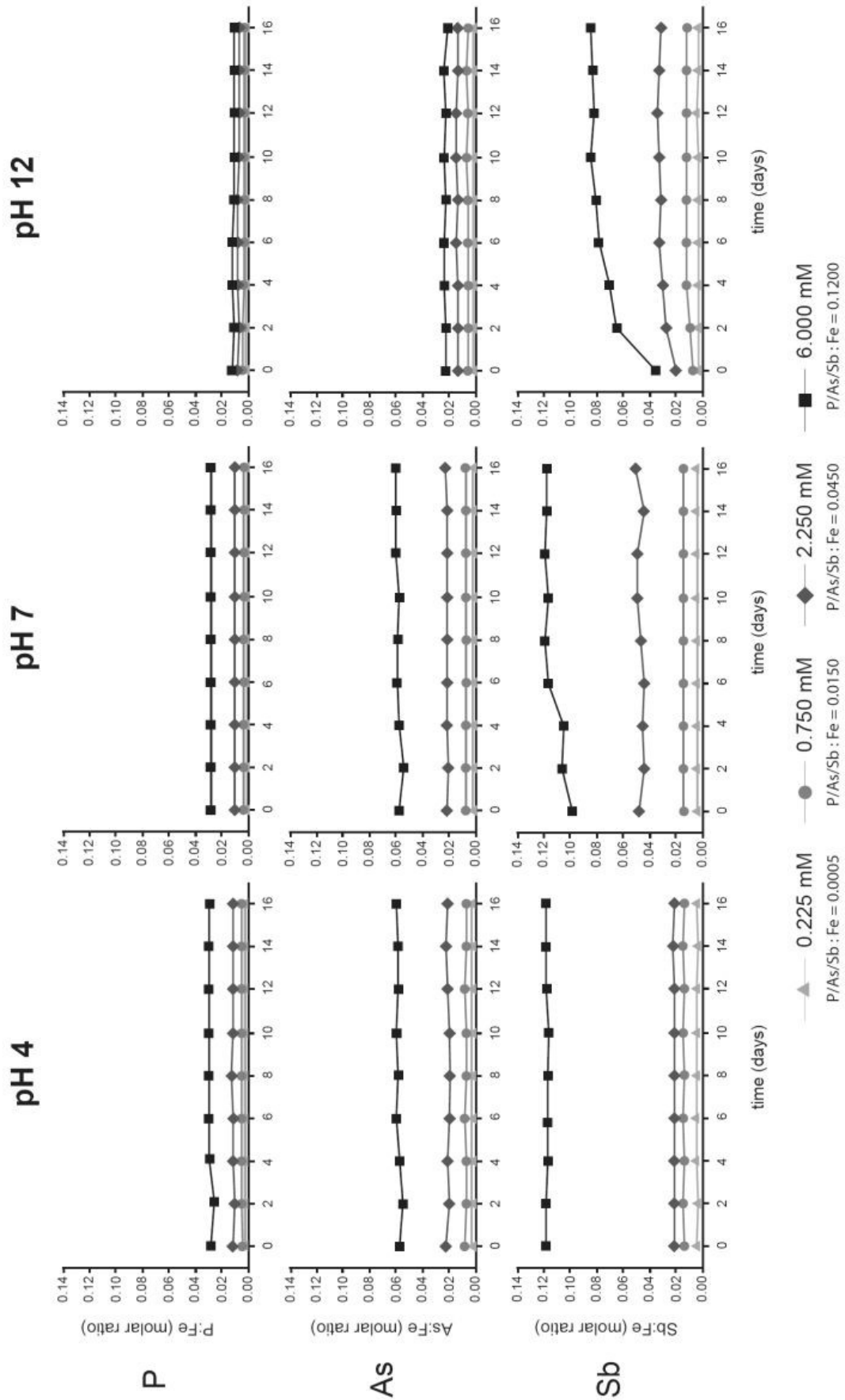


Figure 3: Chemical composition of the transformation products given as molar ratios of P, As, and Sb against Fe. The molar starting ratios of P/As/Sb : Fe are given for each concentration step.

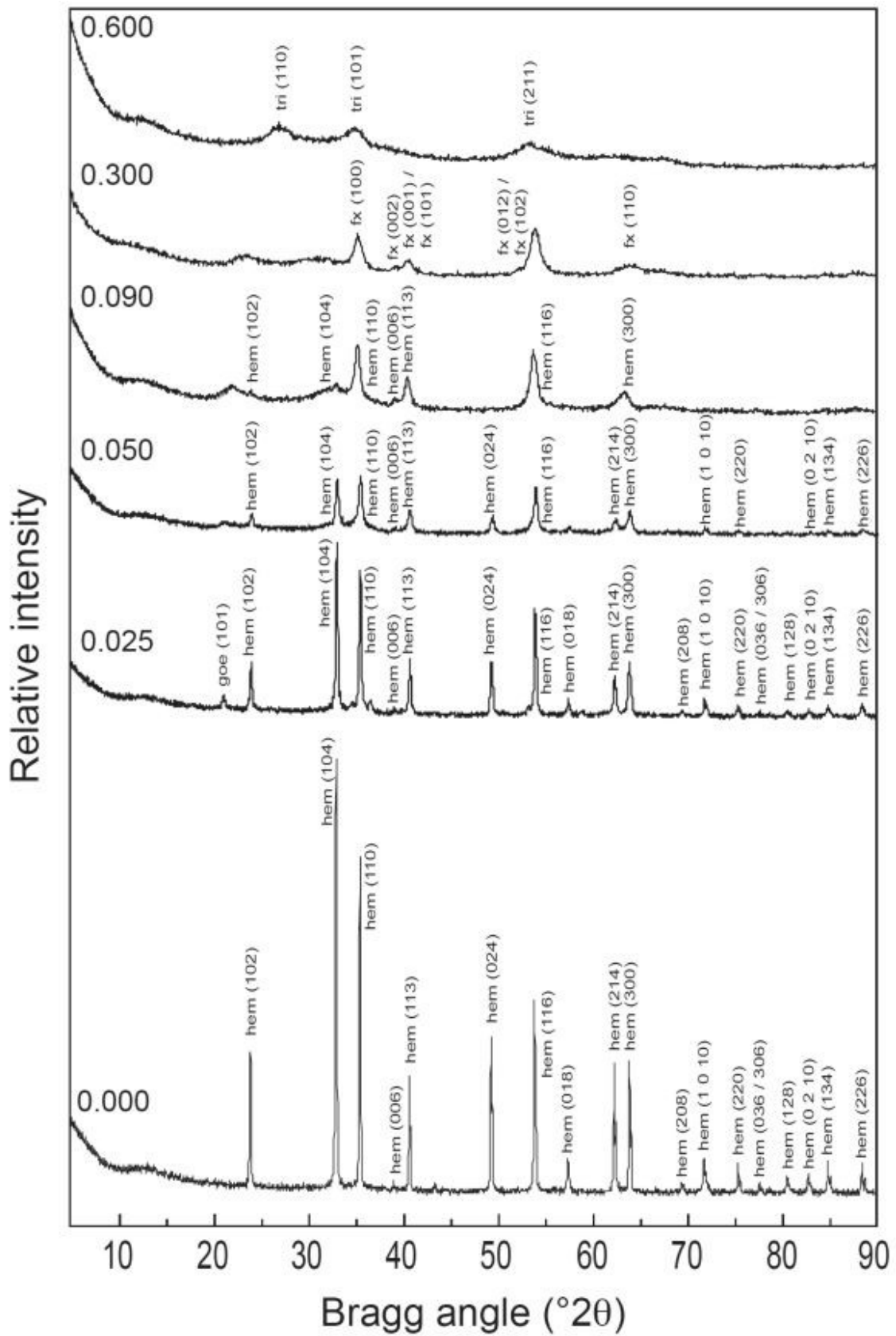


Figure 4: Ferrihydrite transformation in the presence of increasing Sb(V)-concentrations. The numbers in front of each pattern indicate the molar Sb:Fe ratio. hem: hematite, goe: goethite, fx: ferrihydrite, tri: tripuhyte. All experiments were performed at pH 4 and an aging time of 16 days.

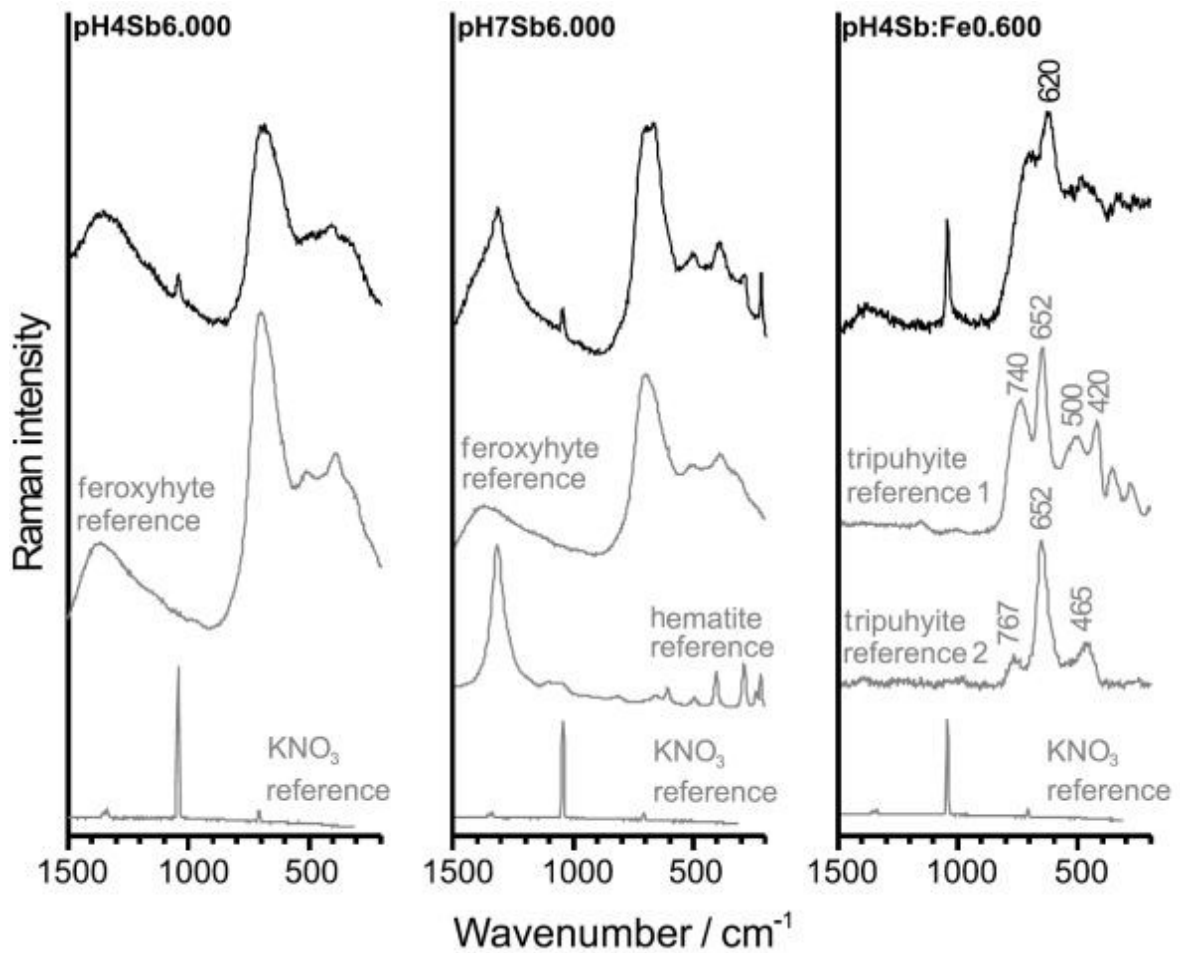
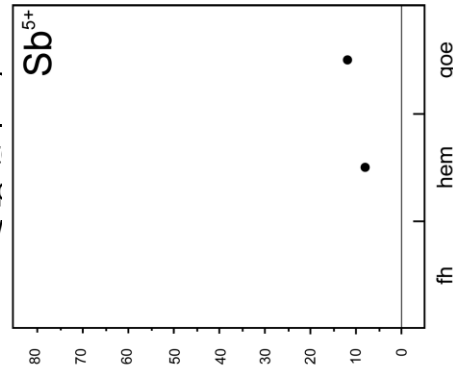
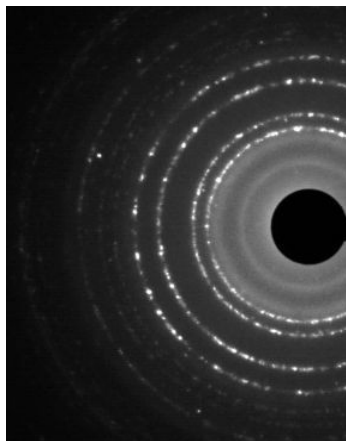
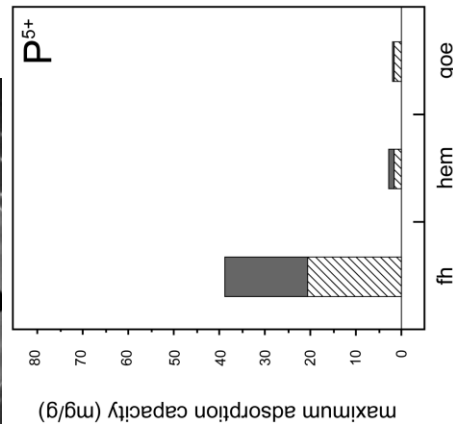
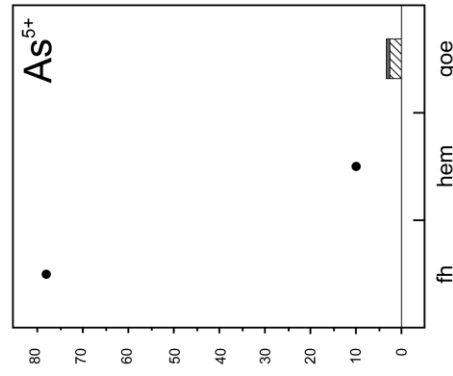


Figure 5: Selected Raman spectra of ferrihydrite transformations at increased Sb(V) concentrations. Sample 1 was transformed at pH 4, 70 °C and Sb(V) concentrations of 6.000 mM with a aging time of 16 days. Sample 2 was transformed at the same conditions, but pH 7 instead of pH 4. Sample 3 was transformed at an molar Sb:Fe ratio of 0.600 at pH 4, 70 °C and 16 days of aging.

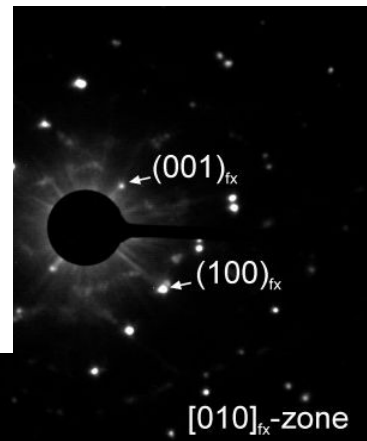
Figure 6: Graphical summary of different literature values. The y-axis represents the maximum adsorption capacity (mg/g) and the x-axis represents the mineral type (fh, hem, goe). Dots indicate that only one literature value was reached by every cited literature value.



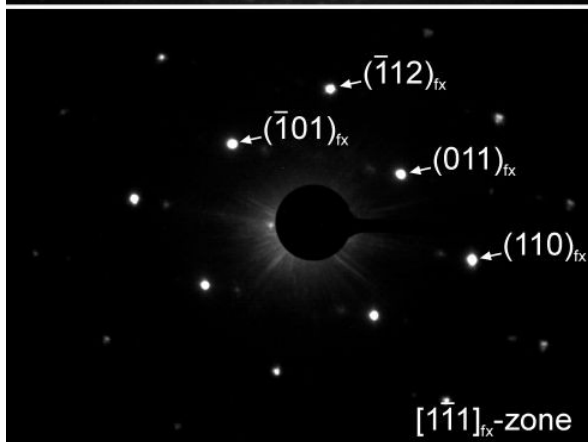
capacities calculated from the adsorption capacity that can be reached by every cited literature value. Dots indicate that hematite, goe: goethite.



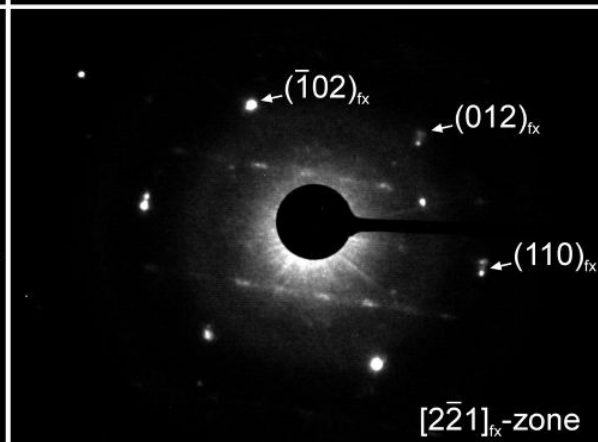
powder



$[010]_{fx}$ -zone



$[1\bar{1}1]_{fx}$ -zone



$[2\bar{2}1]_{fx}$ -zone

Figure 7: Selected electron diffraction pattern of ferroxyhyte. The powder pattern shows the four dominant diffraction lines of ferroxyhyte, whereas additional lines of hematite are clearly absent. In  $[010]_{fx}$  zone pattern, the  $(001)_{fx}$  reflection of ferroxyhyte is

clearly visible but should be extinct for hematite.  $[1\bar{1}1]$  and  $[2\bar{2}1]$  zone pattern belong to the same crystal tilted by  $\sim 18^\circ$  along the  $[110]$  axis.

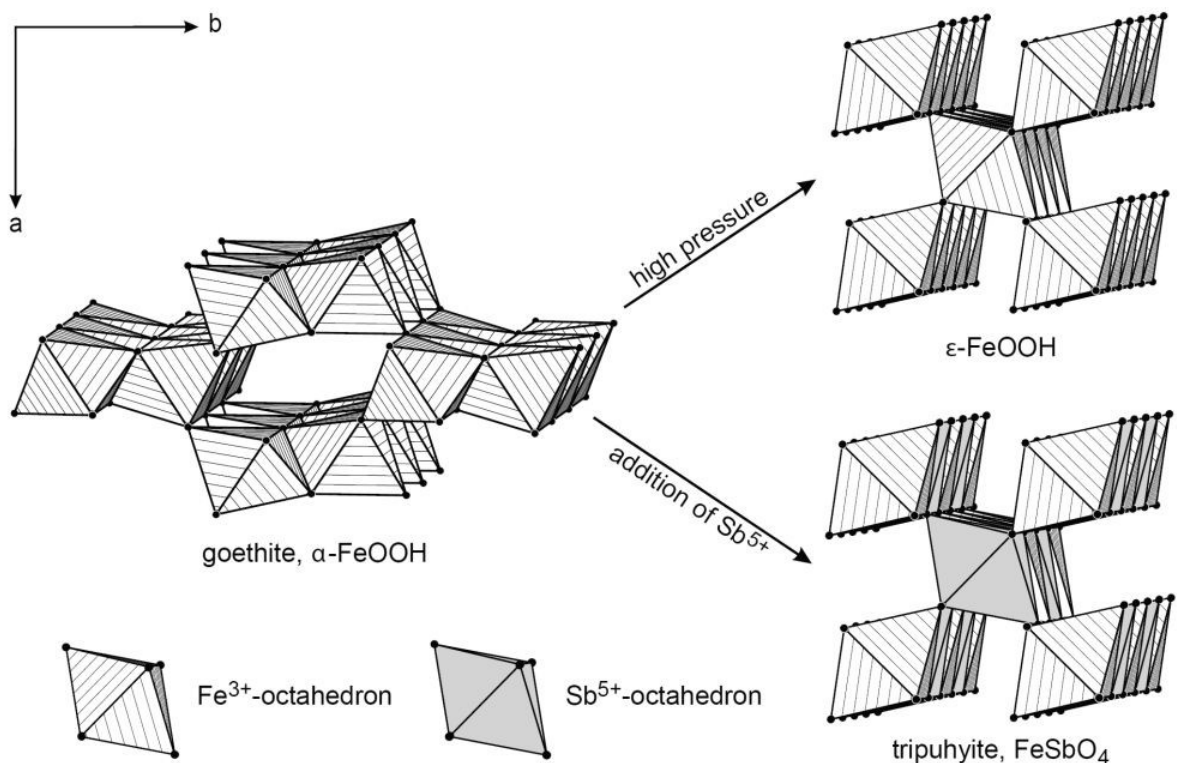


Figure 8: On the left side the structure of goethite ( $\alpha$ -FeOOH) constructed by double octahedral chains (Pbnm setting). In a high pressure environment the tunnels which run parallel to the octahedral chains collapse forming the denser high pressure phase  $\epsilon$ -FeOOH (upper right). During the  $\text{Sb}(\text{V}) \rightarrow \text{Fe}(\text{III})$  substitution these tunnels could

also collapse forming the denser tripuhyite structure (lower right). Both,  $\epsilon$ -FeOOH and tripuhyite are isostructural with rutile.

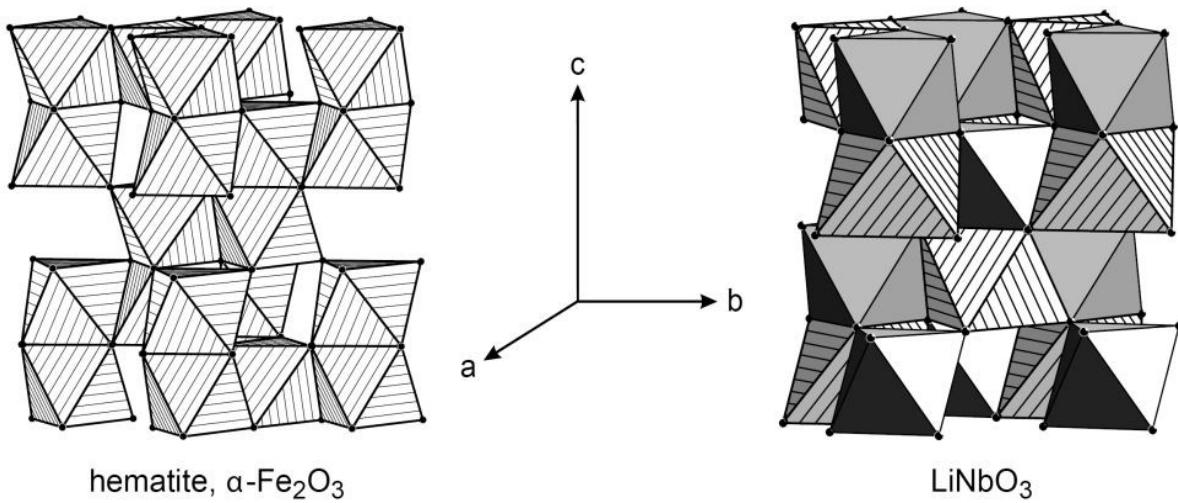


Figure 9: Structures similar to that of hematite (left) can incorporate pentavalent ions. These pentavalent ions cannot occur in close contact to each other because of the strong electrostatic repulsion. In LiNbO<sub>3</sub>, a superstructure of hematite, the presence of Nb(V) face-sharing octahedra is avoided by monovalent Li<sup>+</sup> octahedra in between, reducing the electrostatic repulsion.

## **Outlook**

For a reliable risk assessment of polluted soils, many factors have to be considered in order to distinguish between a soil with an elevated pollutant content and a soil that represents an environmental threat.

In chapter 1, I showed that the type of pollutant, the concentration, and the chemical speciation are utmost important. After 40 years,  $\text{As}^{5+}$  bound in a soluble state in the ash-waste, migrated to those soil constituents which are able to immobilize  $\text{As}^{5+}$ . The  $\text{As}^{5+}$  bound in the hardly soluble glass particles is almost completely immobile and therefore not bioavailable, but even the glass particles will weather over time and release the  $\text{As}^{5+}$  slowly into the environment.

Chapter 2 has shown that arsenic from a polluted geomaterial, *e.g.*, the ash-waste, can then be bound to the surface of ferrihydrite in soil. With time, ferrihydrite will transform to hematite and incorporate a fraction of the  $\text{As}^{5+}$  into the structure of the newly formed hematite. This process will immobilize the  $\text{As}^{5+}$  until the hematite itself becomes unstable.



The immobilization of  $\text{As}^{5+}$  by hematite proceeds via a specific mechanism, namely epitaxial intergrowth of hematite and a ferric arsenate. In chapter 3, I was able to show that other mechanisms operate for other pollutants, like  $\text{Sb}^{5+}$ , even though these may have been considered similar to  $\text{As}^{5+}$ . Pentavalent antimony can affect the transformation of ferrihydrite as well, leading to an incorporation of  $\text{Sb}^{5+}$  into the corresponding transformation products.

The complexity of the immobilization mechanisms of iron oxides is by no means understood. During the last decades, studies focused primarily on the adsorption of pollutants to the surface of iron oxides, whereas the incorporation received almost no attention. It is therefore my believe and hope that this thesis adds weight to the notion that the incorporation of pollutants by iron oxides is possible and might be a driving force in the immobilization of pollutants by iron oxides.

However, further investigations are needed which deal with different pollutants and study the complex transformation mechanisms of ferrihydrite in the presence of contaminants. Only with a better understanding of these mechanisms, which can be an indispensable tool for remediation projects, we will be able to restore a contaminated soil to its original or near-original state.

## **Ehrenwörtliche Erklärung**

Ich erkläre hiermit, dass ich die vorliegende Arbeit selbstständig und unter Verwendung der angegebenen Hilfsmittel, persönlichen Mitteilungen und Quellen angefertigt habe.

Ort, Datum

Unterschrift

.....

.....

## Curriculum Vitae

---

### Angaben zur Person

Vor- und Zuname: Ralph Bolanz  
Geburtsdag: 08.03.1982  
Geburtsort: Freiburg im Breisgau  
Wohnort: 07646 Stadtroda, August-Bebel-Straße 31  
Staatsangehörigkeit: deutsch  
Familienstand: ledig

### Schul Ausbildung

1992 - 1993	Gerhart-Hauptmann Hauptschule Freiburg im Breisgau
1993 - 1999	Walther-Rathenau Realschule Freiburg im Breisgau
1999	Abschluss: Realschulabschluss
2002 - 2004	Gertrud-Luckner Technische Oberschule
2004	Abschluss: Allgemeine Fachhochschulreife

### **Berufsausbildung**

1999 - 2002	Ausbildung zum staatlich geprüften Chemielaboranten an dem Chemischen- und Veterinäruntersuchungsamt in Freiburg im Breisgau
-------------	--

### **Akademischer Werdegang**

2004 - 2009	Studium der Geologie an der Albert-Ludwigs-Universität in Freiburg im Breisgau
2009 brown	Abschluss: Diplom in Geologie mit dem Diplomarbeitsthema "Geo hazards associated with coal mining in Central Slovakia" (Geologische Gefahren verbunden mit Braunkohlebergbau in der Zentralslowakei).
2009-2012	Doktorand als wissenschaftlicher Mitarbeiter an der Friedrich-Schiller-Universität in Jena mit dem Forschungsschwerpunkt „Arsenic and antimony in the environment: Release and possible immobilization mechanisms“ (Freisetzung und Immobilisation von Arsen und Antimon“
2010-2012	Mitglied des Graduiertenkollegs für „Alteration und Elementmobilisierung an Mikroben-Mineral- Grenzflächen“ an der Friedrich-Schiller-Universität Jena.

Ort, Datum

Unterschrift

